Research Square

Preprints are preliminary reports that have not undergone peer review.
They should not be considered conclusive, used to inform clinical practice,
or referenced by the media as validated information.

Contact percolation sets flocking phase transition via chemo-mechanical feedback in heterogeneous breast cancer

Giorgio Scita

giorgio.scita@ifom.eu

IFOM ETS - The AIRC Institute of Molecular Oncology https://orcid.org/0000-0001-7984-1889

Leonardo Barzaghi

IFOM https://orcid.org/0000-0002-3174-6441

Chiara Guidolin

University of Milan

Camillo Mazzella

IFOM

Joseph Ackermann

Sorbonne Université and CNRS, Laboratoire Jean Perrin

Edoardo Bellini

IFOM

Stefano Villa

Max Planck, Gottingen

Emanuela Frittoli

ondazione Istituto FIRC di Oncologia Molecolare

Brenda Green

IFOM ETS - The AIRC Institute of Molecular Oncology

Andrea Palamidessi

Fondazione Istituto FIRC di Oncologia Molecolare https://orcid.org/0000-0002-7134-7023

Angela Cattaneo

IFOM

Angela Bachi

IFOM

Valeria Cancila

University of Palermo

Claudio Tripodo

Ifom

simona Polo

Ifom

Roberto Cerbino

University of Vienna https://orcid.org/0000-0003-0434-7741

Raphael Voituriez

Sorbonne Université and CNRS, Laboratoire Jean Perrin

Fabio Giavazzi

University of Milan https://orcid.org/0000-0003-4930-0592

Article

Keywords:

Posted Date: April 2nd, 2025

DOI: https://doi.org/10.21203/rs.3.rs-6057847/v1

License: This work is licensed under a Creative Commons Attribution 4.0 International License.
Read Full License

Additional Declarations: There is **NO** Competing Interest.

Version of Record: A version of this preprint was published at Nature Communications on September 8th, 2026. See the published version at https://doi.org/10.1038/s41467-026-77357-8.

Contact percolation sets flocking phase transition via chemo-mechanical feedback in heterogeneous breast cancer

Leonardo Barzaghi[1,2], Chiara Guidolin[3], Camillo Mazzella[1], Joseph Ackermann[4], Edoardo Bellini[1,2], Stefano Villa[3,5], Emanuela Frittoli[1], Brenda Green[1], Andrea Palamidessi[1], Angela Cattaneo[6], Angela Bachi[1], Valeria Cancila[7], Claudio Tripodo[1,2,7], Simona Polo[1,2], Roberto Cerbino[8], Raphaël Voituriez[4], Fabio Giavazzi *[3], and Giorgio Scita †[1,2]

[1]IFOM ETS, the AIRC Institute of Molecular Oncology, Milan, Italy

[2]Department of Oncology and Haemato-Oncology, University of Milan, Milan, Italy

[3]Department of Medical Biotechnology and Translational Medicine, University of Milan, Segrate, Italy

[4]Laboratoire Jean Perrin, CNRS/Sorbonne Université, Paris, France

[5]Max Plank Institute for Dynamics and Self-Organization, Göttingen, Germany

[6]Cogentech SRL Benefit Corporation, Milan, Italy

[7]Department of Health Sciences, Human Pathology Section, University of Palermo School of Medicine, Palermo, Italy

[8]Faculty of Physics, University of Vienna, Vienna, Austria

*fabio.giavazzi@unimi.it

†giorgio.scita@ifom.eu

Abstract

Breast cancer progression is driven by dynamic changes in tissue mechanics that promote phase transitions toward collective cell movement, immune activation, and invasion. While previous investigations primarily employed model systems of genetically identical cells, breast carcinoma consists of heterogeneous cell populations varying in genetic and mechanical traits. The complex interplay between this diversity and collective cell dynamics, affecting phase transitions and tumor progression, remains largely unexplored. Here, we interpreted our experimental data through contact percolation theory to uncover a chemo-mechanical switch underlying a phase transition via the emergence of flocking motility in heterogeneous breast cancer tissues. Using engineered mixtures of motile RAB5A-expressing cells and immotile controls, we demonstrate that interconnected system-spanning clusters of fluidized RAB5A cells induce a phenotypic switch in neighboring cells, enabling them to acquire full-scale, flocking-like motility and reprogram their transcriptional state. This transition is accompanied by the activation of pro-inflammatory gene programs. Our theoretical modeling supports a mechanism by which local cell composition drives a motility switch critical for the emergence of coordinated, system-wide movement. These findings highlight the role of mechanical heterogeneity in tumor progression and identify contact percolation as a fundamental mechanism driving dynamic tissue reorganization and immune modulation at the root of breast cancer invasion and metastasis.

1 Introduction

Phase transitions are fundamental physical phenomena where gradual changes in individual cell parameters result in sudden, large-scale shifts in tissue behavior once a critical threshold is reached [1, 2]. Tissue-scale phase transitions are now recognized as pivotal in shaping cell behavior and fate across diverse physiological and pathological contexts [3–7]. One prominent example is the unjamming process, where solid, mature epithelial tissues transition into a fluid-like state. This shift is crucial for understanding cellular behaviors in regeneration, development, wound healing, and cancer invasion, as it allows cells to become more motile and responsive, adapting to the demands of each context [8–12]. A case where the jamming paradigm might ideally apply is in the progression of breast carcinoma (BC). In the course of the natural history of BC, malignant progression is marked by a critical shift in cell motility, characterized by a phase transition from a solid-like, jammed tissue state to a fluid-like, unjammed state [3, 9, 13–18]. This transition enables cancer cells to overcome the physical confinements of the mammary duct, allowing them to invade adjacent tissues. Despite its importance in cancer progression, the precise mechanisms by which cells initiate and regulate this phase transition remain largely unknown. We have recently characterized the jamming-to-unjamming transition as an endocytic-dependent, mechanically-driven, collective motility strategy of cell dissemination [19, 20]. Specifically, we showed that RAB5A, a master regulator of endocytosis, whose expression is elevated in aggressive human BC and correlates with reduced relapse-free survival of BC patients [21], is sufficient to reawaken via tissue fluidification the collective motility of kinetically arrested Ductal Carcinoma in Situ (DCIS) cells and their progression to Invasive Ductal Carcinoma (IDC). Molecularly, RAB5A-induced unjamming arises through a combination of increased junctional tension among neighboring cells and active cell reorientation, mediated by deregulation of the Epidermal Growth Factor Receptor (EGFR) pathway and trafficking [20]. This axis is essential to elicit RAB5A-dependent PT toward a flocking-fluid state characterized by the coexistence of both local short-range cell rearrangements and global, long-range coordinated and persistent flocking behavior, akin to the motion of ensembles of collective living animals, as bird flocks or fish schools. Remarkably, this RAB5A-mediated dynamic transition in tissue monolayers is sufficient to promote the persistent rotational motion of DCIS spheroids and organoids, leading to individual and collective invasion in 3D matrices and murine models [20]. Notably, this tissue-level phase transition is not merely a short-term response that

alters the characteristics and behavior of BC cell collectives. It also initiates a surprising long-term shift in gene expression, activating an innate immune response [22]. This shift is driven by the abnormal activation of the cGAS/STING pathway, leading to an inflammatory gene signature known as the Interferon-Stimulated Genes (ISG) or cytosolic DNA response (CytoDR). Through this pathway, cells in the unjammed, fluid-like state initiate a sustained inflammatory response, linking mechanical changes in the tumor microenvironment to immune activation [22]. These observations collectively support the hypothesis that a solid-to-liquid PT, facilitated by flocking in BC, plays a crucial role in BC progression. However, this transition has so far been studied only in model systems with genetically identical cells. In contrast, BC typically involves a heterogeneous cell population, with variations not only in genetic background but also in mechanical properties [13, 15, 18, 23–26]. This intra-tumor heterogeneity arises from a range of intrinsic factors, including genetic, epigenetic, and proteomic differences, as well as from external interactions with the surrounding microenvironment [23]. In line with this, we also showed that in human DCIS the expression of RAB5A is heterogeneous and typically elevated at the invasive front of breast cancer tumors that are about to invade the surrounding environment [20, 22, 25]. This is accompanied by local and spatially confined activation of cGAS and cGAS-dependent gene transcriptions. Whether and how cell mechanical heterogeneity impacts tissue dynamics, cell state, and tumor progression is poorly understood. In addition, we currently lack a comprehensive physical framework to understand how the complex interplay between mechanical, genetic, and phenotypic heterogeneity impacts or is impacted by the collective behaviors in solid malignancies. In this study, we investigated the impact of mechano-genomic heterogeneity on tissue-level PT, with a focus on its role in BC progression. We engineered mixed cell populations, combining fluidized BC cells overexpressing RAB5A with non-fluidized cells, and monitored their collective motility in confluent monolayers. Our findings are analyzed through the lens of percolation theory, suggesting that new emergent material properties arise when cell clusters interconnect, forming a network that spans the entire system. This connection enables a global flocking-fluid state, where even the jammed, immotile control cells participate in collective movement and adopt a pro-inflammatory signature. Our results demonstrate that mechano-chemical interactions between fluidized and solid-like cells drive a phenotypic and transcriptional shift across the entire heterogeneous cell population. Together, these insights reveal how mechanical and genomic heterogeneity, governed by percolation and chemo-mechanical signaling, promotes tissue-level phase transitions toward a flocking-fluid

state. This phenomenon has important implications for understanding the transition from DCIS to IDC.

2 Results

2.1 Percolation of motile cells sets the emergence of global flocking in heterogeneous breast cancer cell monolayers

To investigate the impact of mechanical heterogeneity on tissue dynamics, we use as a model system breast cancer epithelial monolayers comprising varying proportions of cells with distinct genetic and mechanical properties: control and RAB5A-expressing MCF10DCIS.com cells. MCF10DCIS.com cells, which are a well-established model system for studying the transition from DCIS to IDC when injected into immunocompromised mice, were engineered to express in a doxycycline-inducible fashion RAB5A to levels normally encountered in BC (Supplementary Fig.1A,B). We verified the homogeneity of RAB5A expression, which is a critical control parameter for the correct interpretation of subsequent experiments, by immunofluorescence analysis and quantification of protein cytoplasmic signal (Supplementary Fig.1C,D). Control MCF10DCIS.com cells were also engineered to co-express EGFP-H2B, while hyper-motile RAB5A-cells co-express mCherry-H2B. Using this system, we seeded cells to form hyperconfluent and densely packed monolayers composed of a variable fraction of control and RAB5A cells to reproduce cell mechano-dynamic heterogeneity in a controlled fashion (Fig.1A). We monitored both individual and collective behaviors through time-lapse microscopy (Supplementary Movie 1) and we interpreted our findings using contact percolation theory. This theory describes the behavior of a network when its components become progressively more interconnected until they form a system-spanning connected cluster [27, 28].

Using particle image velocimetry (PIV) and nuclear tracking, we initially extracted key motility parameters (Fig.1B-D), while cell segmentation via Voronoi tessellation enabled us to monitor the formation of interconnected, system-spanning supracellular clusters of control and RAB5A-expressing cells (Fig.1E,F). The analysis of the kinetic properties of mixed monolayers revealed that when 100% of control cells were seeded to form homogenous monolayers, they ceased their motion due to jamming, whereas monolayers composed of 100% of RAB5A cells display flocking-fluid motility, characterized by the coexistence of large local velocity fluctuations, captured by the root mean squared velocity V_{rms}, and long-range coordination of motion with large value of mean velocity (the velocity V_{CM} of the center of mass of the whole monolayer), correlation length L_{corr}, persistence length L_{pers} and order parameter ψ. The order parameter $\psi = |\langle v \rangle|/\langle |v| \rangle$, which can vary from 0 to 1, quantifies the uniformity of the velocity field v, with

$\psi = 1$ indicating perfectly coordinated motion where all cells move in the same direction and at the same speed, while $\psi \simeq 0$ for randomly oriented velocities. The correlation length L_{corr} quantifies the average distance over which cells move in a coordinated manner, and the length of persistence L_{pers} corresponds to the typical distance a cell travels with constant velocity before its motion becomes randomized. Analyzing motility parameters in mixed control/RAB5A populations, we observed two distinct dynamics dependent on monolayer composition. The root mean square velocity V_{rms} of the entire monolayer displayed an almost linear increase with the fraction of RAB5A cells, indicating enhanced local motility and amplitude of cell mutual displacements as a function of the increased RAB5A cell density (Fig.1B). Conversely, long-range coordinated motion as captured by the mean velocity and the order parameter (Fig.1C) display threshold-like behavior, with a relatively sharp increase above a critical value of about 50% of RAB5A cells in the monolayer. Similar behavior is also displayed by the correlation length and the persistence length (Fig.1D). We observed an analogous threshold-like behavior in collective motility also in the non-tumorigenic epithelial cell line MCF10A (Supplementary Fig.2 and Supplementary Movie 2). These measurements indicate that for the entire monolayers to flock a fraction of RAB5A cells above a critical threshold of about 50% is needed. Importantly, above this critical point of cell composition, cell segmentation analysis revealed the formation of percolating clusters of RAB5A cells that span the entire field of view (Fig.1E,F). Thus, this 50% threshold corresponds to the percolation threshold, the critical proportion of cells necessary to form system-spanning, interconnected clusters.

Collectively, these data suggest that when RAB5A-expressing cells represent more than 50% of the population, a condition whereby a percolating network of fluidized cells can form across the whole monolayer, flocking motion of the entire model tissue is also triggered. We further analyzed individual population dynamics by leveraging differential fluorescent markers in control and RAB5A cells, allowing independent measurements of V_{rms}, V_{CM}, and ψ for each population (Supplementary Fig.1E-G). Remarkably, the values of these parameters were indistinguishable between control and RAB5A cells at each relative monolayer composition, suggesting that direct contact between RAB5A cells not only dictates their dynamic behavior but also impacts the motility of control cells. This indicates that local monolayer composition directly influences the motility of individual cells.

Different reports have shown that mixing cells with different mechanical properties may lead

to compartmentalization and sorting [29–32]. This phenomenon is thought to be related to the establishment of an effective interfacial tension between cells that differ in mobility, stiffness, or adhesiveness. Since the presence of cell sorting could impact the statistics of connected clusters and thus confound our results, we experimentally verified whether demixing (sorting) occurs in the population of control and RAB5A-cells. To test this, we calculated a demixing parameter (DP) for each population (Supplementary Fig.1H). DP evaluates the average surroundings of each species, determining the likelihood of being surrounded by cells of similar (homotypic) or dissimilar (heterotypic) nature [31]. Specifically, for a given cell kind, DP was calculated using the formula $DP = (\langle \frac{n^{self}}{n^{tot}} \rangle - \phi_{self})(1 - \phi_{self})^{-1}$, where n^{tot} is the total number of neighbors, n^{self} is the number of homotypic neighbors (i.e., cells belonging to the same population, either controls or RAB5A-expressing), and ϕ_{self} is the fraction of cells of that same kind in the monolayer. If the two populations are well mixed, we expect $\frac{n^{self}}{n^{tot}} \cong \phi_{self}$, thus $DP \simeq 0$. If there is a certain level of demixing, cells will be surrounded on average by more cells of the same kind compared to the expected value ϕ_{self} and thus $DP > 0$. In the limit case of complete sorting, a cell is surrounded by all cells of the same family, so $n^{self} = n^{tot}$ and $DP = 1$. We found that DP remained below 0.2 across all RAB5A fractions and was not significantly affected by the fraction of RAB5A-expressing cells in the mixed monolayers (Supplementary Fig.1I). We reasoned that this behavior is likely due to the small-scale and short-range demixing consequence of the presence of an excess of pairs of neighboring cells of the same population due to cell division. We verified this contention by measuring the DP in a population composed of control cells expressing either EGFP-H2B or mCherry-H2B (Supplementary Fig.1L). We found similar, relatively small values of DP in both mixed controls and controls/RAB5A-expressing monolayers, indicating that the small-scale demixing is due to local cell division and not the result of active sorting due to interfacial tension.

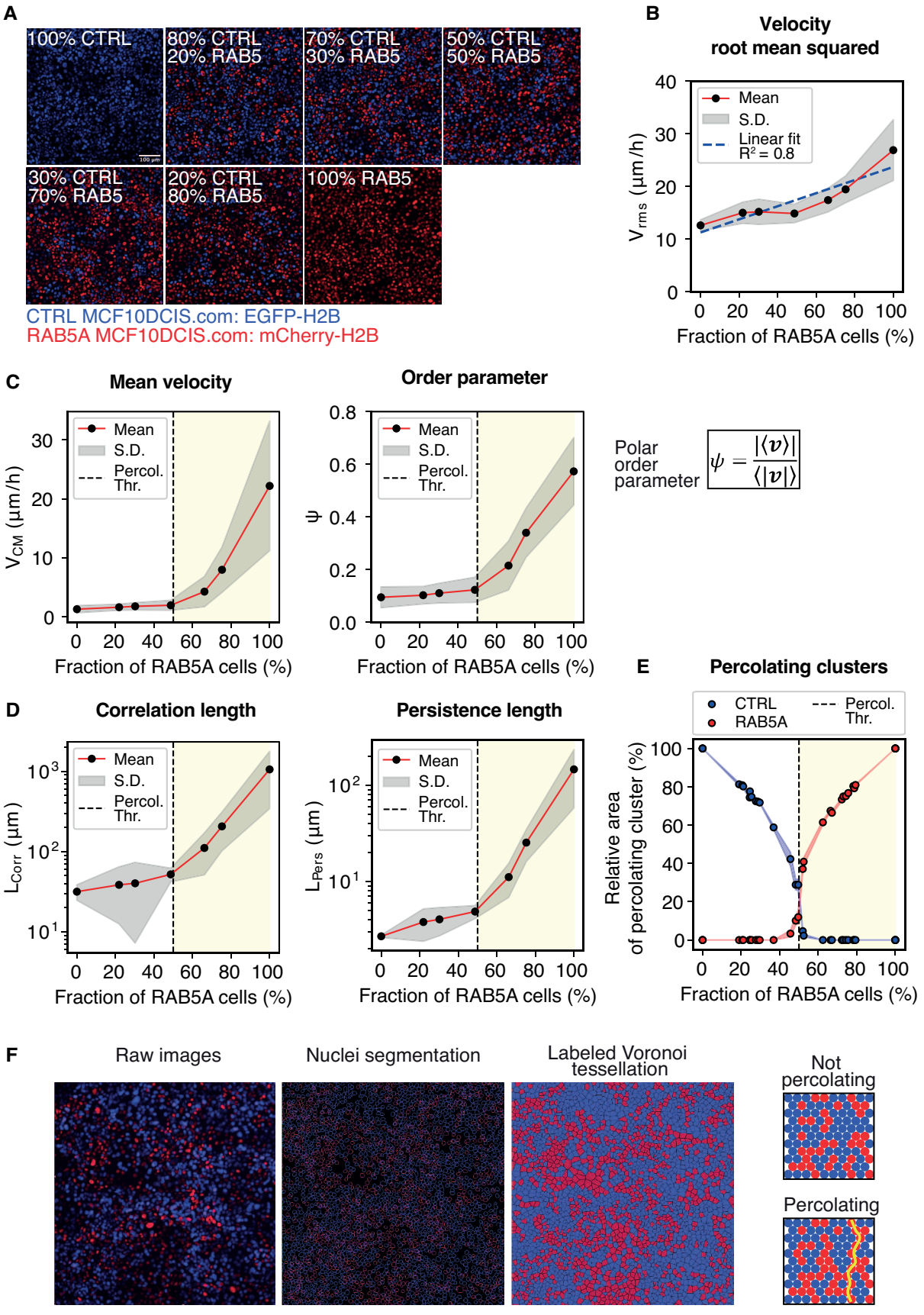

A
100% CTRL
80% CTRL
20% RAB5
70% CTRL
30% RAB5
50% CTRL
50% RAB5
30% CTRL
70% RAB5
20% CTRL
80% RAB5
100% RAB5
CTRL MCF10DCIS.com: EGFP-H2B
RAB5A MCF10DCIS.com: mCherry-H2B
B
Velocity
root mean squared
Mean
S.D.
Linear fit
R² = 0.8
V_rms (μm/h)
Fraction of RAB5A cells (%)
C
Mean velocity
Order parameter
Mean
S.D.
Percol. Thr.
V_CM (μm/h)
Ψ
Fraction of RAB5A cells (%)
Polar order parameter
ψ = |⟨v⟩| / ⟨|v|⟩
D
Correlation length
Persistence length
L_Corr (μm)
L_Pers (μm)
E
Percolating clusters
CTRL
RAB5A
Percol. Thr.
Relative area of percolating cluster (%)
F
Raw images
Nuclei segmentation
Labeled Voronoi tessellation
Not percolating
Percolating

Figure 1: Collective flocking transition of mixed monolayers coincide with contact percolation of motile cells.

(A) Representative fluorescent images of control, marked with EGFP-H2B in the nuclei (blue), and RAB5A-expressing, marked with mCherry-H2B in the nuclei (red), MCF10DCIS.com cells seeded at various relative ratios to form confluent mixed monolayers. The images are representative of > 10 independent experiments. Scale bar, $100\,\mu$m. (B-D) Motility parameters plotted as a function of the relative amount of RAB5A-MCF10DCIS.com cells obtained by nuclear tracking of mixed monolayers monitored by time-lapse microscopy. Motility parameters are evaluated over a ~ 10 hours time window centered on the peak of motility of RAB5A cells. (B) Root mean square velocity (V_{rms}) in the centre of mass reference frame. Blue line is the linear fitting of the data. (C) Left: mean velocity of the centre of mass (V_{cm}). Right: polar order parameter ψ. $\psi = 1$ means a perfectly uniform velocity field, $\psi \approx 0$ indicates randomly oriented velocities. (D) Left: length of correlation (L_{corr}), obtained from stretched exponential fits on spatial velocity correlation function curves; right: length of persistence (L_{pers}), obtained by fitting the MSD curves with a model function describing the transition from a short-time ballistic to a long-time diffusive behavior. Dashed black lines indicate the percolation threshold of RAB5A cells. Data are the mean $\pm$ S.D (n= 15 fields of view from 3 independent experiments). (E) Area of cell clusters that percolate the entire field of view relative to the total surface area of RAB5A-expressing MCF10DCIS.com in mixed monolayers as a function of the relative number of RAB5A-cells. Dashed black line indicates the percolation threshold. Data are the mean $\pm$ S.D (n= 15 fields of view from 3 independent experiments). (F) Representative snapshots describing the pipeline of analysis of mixed MCF10DCIS.com monolayers to define percolating clusters: raw images obtained through time-lapse fluorescence microscopy, nuclei segmentation, Voronoi tessellation and cluster assignment.

2.2 Blocking local percolation impairs the emergence of flocking motility

To establish a direct causal relationship between the percolation and flocking motility thresholds, we took two distinct orthogonal experimental and theoretical approaches. We initially assessed cellular dynamics in monolayers where local percolation was selectively hindered. We used mixed populations of control and RAB5A cells where percolation was impeded at the local level, while the global fraction of motile fluidized cells was well above the theoretical percolation threshold of 50%. Specifically, we employed silicone stencils consisting of two separate chambers where cells can be co-cultured. We then removed the wall between the compartments and allowed the two cell populations (one consisting of 100% RAB5A cells, the other of a 50% mixture) to form confluent monolayers. Under these conditions, despite the global fraction of hypermotile RAB5A cells being about 75%, well above the critical percolation threshold of 50%, RAB5A cells could not form an interconnected, system-spanning cluster (Supplementary Fig.3A and Supplementary Movie 3). As expected, we detected flocking-like, spatially correlated motility only in the half plane where percolation of RAB5A cells occurred, determined in this case by mapping the local decorrelation rate, which measures the opposite of the time needed by a cell to move with a displacement corresponding to the cell size (the higher is the local decorrelation rate, the fastest are the cells [33]) (Supplementary Fig.3A, right). However, the whole system failed to undergo long-range motility despite the global mixing ratio being above the critical percolation threshold, but no system-spanning, interconnected cluster could be formed.

This indicates that rather than a global mechanism akin to quorum sensing, the local composition and short-range interactions govern the emergence of collective flocking motility in heterogeneous populations of cells with distinct intrinsic migratory properties. This result also underscores that a purely geometric property, namely the presence of system-spanning connected cluster of hypermotile cells, whose emergence can be predicted by classical percolation theory, serves as a determinant for the emergence of flocking-fluid migratory behavior in mixed cell collectives.

2.3 Theoretical models indicate that a phenotype-switching mechanism accounts for the emergence of flocking behavior at the percolation threshold

To gain further mechanistic insights into the dynamic interplay between mechanically distinct cell populations and to validate with a complementary approach our experimental findings, we conducted numerical simulations and theoretical modeling of mixed cell monolayers designed to replicate the motility properties observed in vitro. Simple agent-based models, where cells are represented by active, interacting particles have been shown to reproduce effectively key aspects of the morphology, the structure, and the dynamics associated with collective behavior in dense cell assemblies [34]. Various models have been proposed to capture the salient features of the striking directed collective motility exhibited by confluent monolayers of RAB5A-expressing cells, including particle-based [35] and tessellation-based [19, 36] models. Despite the different implementations, a key common ingredient of these models is the presence of an aligning interaction between neighboring cells promoting local velocity coordination and, in the presence of sufficiently low noise, the emergence of long-range order in the velocity field. Fully confluent monolayers of control cells, instead, display a highly disordered motility pattern, characterized by short-ranged velocity correlations and poorly persistent motion at the single-cell level. This is compatible with the behavior of a dense collection of active particles randomly interacting against each other with poor or no mutual coordination.

Firstly, using a minimalistic model of self-propelled soft repulsive disks, we performed simulations of heterogeneous monolayers defined as binary mixtures of two families of particles [37]. In this model, the monolayer is represented by a two-dimensional assembly of interacting, active disks. The motion of each particle or cell i is determined by a combination of the repulsive force $\sum_j \mathbf{F}_{ij}$ exerted by neighboring cells j and the self-propulsion velocity $v_{0,i}\widehat{\mathbf{n}}_i$ of the cell (Fig.2A).

$$\dot{\mathbf{r}}_i(t) = v_{0,i}\widehat{\mathbf{n}}_i(t) + \mu \sum_j \mathbf{F}_{ij}(t) \tag{1}$$

where $\mathbf{F}_{ij} = k(a_i + a_j - |\mathbf{r}_i - \mathbf{r}_j|)(\mathbf{r}_i - \mathbf{r}_j)/|\mathbf{r}_i - \mathbf{r}_j|$ if $|\mathbf{r}_i - \mathbf{r}_j| < (a_i + a_j)$ and $\mathbf{F}_{ij} = 0$ otherwise. Here a_i is the radius of disk i. An active alignment mechanism, characterized by an orientation rate Γ_i, is incorporated to promote the alignment of the self-propulsion velocity of cell i along

the direction of its velocity

$$\dot{\theta}_i(t) = \Gamma_i[\psi_i(t) - \theta_i(t)] + \eta_i(t) \tag{2}$$

Here θ_i is the angle between the direction $\widehat{\mathbf{n}}_i$ of the self-propulsion velocity and the x-axis, ψ_i is the angle between the instantaneous velocity $\dot{\boldsymbol{r}}_i$ and the x-axis, and η_i is a Gaussian noise with zero mean and variance $2D_i$. We start by considering two distinct families of cells: efficient "aligners", for which $\Gamma_i = \Gamma > 0$, and non-aligners or "dissenters", for which $\Gamma_i = 0$ (Fig.2B). The other model parameters D_i and $v_{0,i}$ are assumed to take the same values for all cells, irrespective of their alignment propensity (see Methods, section 18 for details). These choices ensure that, for "pure" systems, constituted by 100% of aligners or 100% of dissenters, the model captures the salient features of the collective behavior of RAB5A and control cells, respectively [35]. We conducted simulations across different monolayer compositions, by changing the fraction ϕ of aligners and monitoring the presence of collective directed migration via the polar order parameter ψ. Flocking is only observed when dissenters were below 10%, in agreement with previous work [37] whereas in a similar system of mixed aligners and dissenters, a small fraction of dissenters was shown to be sufficient to disrupt an otherwise ordered flock (Fig.2C). Thus, the results obtained from simulations failed to reproduce the experimental observation that the flocking transition occurs at approximately 50% of RAB5A cells. They further suggest that control cells when embedded within heterogeneous monolayers exhibit a behavior that differs from that of pure dissenters and may, instead, adapt their dynamic behavior in response to RAB5A influence.

To explore this possibility further and reconcile model predictions and experimental observations, we introduce an additional mechanism enabling the cells to dynamically adapt their motility behavior in response to external stimuli or changes in the local environment (see Methods, section 17 for details). In line with the model described above, single-cell behavior is fully controlled by a set of three parameters $[v_{0,i}, \Gamma_i, D_{r,i}]$ encoding for self-propulsion speed, reorientation efficiency, and amplitude of the rotational noise, respectively. While in most implementations these parameters are considered to be constant over time, it is possible to introduce different mechanisms driving a change in single-cell identity, in response for example to the number of aligner cells in their immediate vicinity. Here, we introduce an explicit dependency

on the value of reorientation efficiency Γ_i of each cell on the composition of the set of particles surrounding it. For the sake of definiteness, we focus on a specific implementation considering a simple non-symmetric "majority rule", where a dissenter switches to an aligning behavior (it assumes a non-zero value for the reorientation efficiency Γ_i, identical to that of the aligners) whenever the majority of its first neighbors are represented by aligners (Fig.2D). This transition is assumed to be reversible. Stated differently, we assumed a "phenotypic switch" mechanism governed by a majority rule, whereby a dissenter cell, when surrounded by dissenters, persists in its state; on the other hand, if the majority of its neighbors are aligners, the dissenter cell transiently becomes an aligner and acquires the ability to sense the direction of its velocity and to align its self-propulsion speed accordingly. By introducing a majority rule-dependent phenotype-switching mechanism into the simulation, we obtained a qualitative and quantitative agreement with our experimental observations. The collective global behavior of a mixed monolayer displays a sharp transition toward a flocking state when about 50% of the cells express RAB5A and possess a stable aligning phenotype (Fig.2E), which is strikingly close to the percolation threshold. The reason why the introduction of the majority rule effectively displaces the position of the threshold for the flocking can be at least qualitatively understood based on the following argument. When the fraction of dissenters is low, almost all dissenter cells are surrounded by a majority of aligners and thus behave like aligners: the "effective" fraction of aligners remains almost 100% and, according to the above results, the monolayer is an ordered flocking state. A significant fraction of dissenters who maintain their identity can be present only when the probability for a dissenter cell to be surrounded by a majority of dissenter cells becomes large enough and this happens only if the nominal fraction is much larger. This semi-qualitative picture is also confirmed by numerical simulations (Fig.2F), showing a sharp increase in the effective fraction of aligners when the nominal fraction of aligners is increased, saturating to almost 100% for $\phi \sim 50\%$.

This modeling approach not only supports our experimental findings but also provides a framework for understanding how interactions between different mechanical cell phenotypes can lead to emergent collective behaviors. The ability of non-aligning cells to adopt an aligning phenotype in the presence of a majority of aligning cells highlights the importance of local microenvironmental and cell-cell communication cues in driving global tissue dynamics.

To assess the robustness of our results that are based on the above-defined agent-based model,

we also derived analytically general continuous hydrodynamic equations that describe the dynamics of generic binary mixtures of interacting cells. Based on an explicit coarse-graining procedure inspired by [37], we started with a minimal, generic definition of the microscopic dynamics of binary cell mixtures with local (nearest neighbors) interactions, consistent with our agent-based model, and obtained (see Supplementary Material - Hydrodynamic model for details) the dynamics of the corresponding continuous hydrodynamic variables ρ_i (cell density) , p_i (normalized cell polarity) and v_i (cell velocity), defined as local averages for each cell type i. In the context of our experiments with $i = C$ (control) and $j = R$ (RAB5A), the hydrodynamic equations can be written for spatially uniform states

$$\partial_t p_R = (j_{RR}\rho_R - D_R - \frac{j_{RC}^2}{2D_R}\rho_C^2 p_C^2)p_R + j_{RC}\rho_C p_C - \frac{j_{RR}^2}{2D_R}\rho_R^2 p_R^3 - \frac{j_{RC}j_{RR}}{D_R}\rho_C\rho_R p_R^2 p^C \quad (3)$$

$$\partial_t p_C = -D_C p_C + j_{CR}\rho_R p_R - \frac{j_{CR}^2}{2D_C}\rho_R^2 p_R^2 p_C \quad (4)$$

where D_i denotes the relaxation rate of the polarity of cell type i induced by fluctuations, and j_{ij} accounts for the strength of the aligning interaction of the polarity of cell type i with neighboring cells of type j (Fig.2G). We further assume a constant total cell density $\rho = \rho_C + \rho_R$ so that the fraction of RAB5A cells is $\phi = \rho_R/\rho$. Last, following experimental observations, we set relative friction coefficients in the force balance equation large enough to ensure $v_R = v_C \propto p_C \propto p_R$ (see Supplementary Material - Hydrodynamic model for details).

While the general dynamics is symmetric under the substitution $R \longleftrightarrow C$, based on our experimental findings, we set $j_{CC} = 0$ in Eq.4, so that in the absence of RAB5A cells, control cells alone ($\phi = 0$) relax to the non flocking state $p_C = 0$ and $j_{RR}\rho - D_R > 0$ in Eq.(3), so that RAB5A cells alone ($\phi = 1$) are in the flocking state $p_R \neq 0$. Importantly, taking $j_{CR} > 0$ effectively accounts for the phenotypic switch observed experimentally, as it promotes the alignment of p_C with p_R (see Eq.4) in a ρ_R dependent manner. In turn, in the absence of phenotypic switch ($j_{CR} = 0$ and thus $p_C = 0$ from Eq. 4), taking $j_{RC} > 0$ recapitulates our above observation in the numerical model that the fluctuations of the polarity of control cells (p_C^2 term in Eq. 4) disfavor the ordering of RAB5A cells and shift the flocking transition to larger values of ϕ. The analysis of this hydrodynamic model has the following merits. (i) The stationary states of Eqs. 3, 4 can be straightforwardly obtained and yield explicit expressions for $p_R(\phi)$ and $p_C(\phi)$ (see

Supplementary Material - Hydrodynamic model and Fig.2H). This shows that binary cell mixtures generically undergo a flocking transition for a critical fraction of RAB5A cells ϕ_C. This threshold value is controlled and can be significantly lowered, by the strength of the aligning interaction of control cells with RAB5A cells j_{CR}, in agreement with our experimental observations and analysis of the numerical model. Of note, such continuous description does not capture the local cell geometry, and thus cannot predict numerically the exact critical value of geometric percolation $\phi_p = 1/2$ for hexagonal packings. However, our analysis shows that ϕ_p can indeed be strikingly close to the flocking transition threshold ϕ_C as we observe experimentally for a simple choice of coupling values $j_{RC} = j_{RR} = j_{CR}$ and $D_R = D_C$ (Fig.2H); this suggests that control and RAB5A cells share similar properties except for their propensity to flock in uniform phases, which is parametrized by j_{CC} and j_{RR}. Note, however, that for general cell mixtures ϕ_p and ϕ_C do not need to be strictly identical, as ϕ_C depends on fluctuation strengths D_i and interactions j_{ij} (see Supplementary Material - Hydrodynamic model and inset in Fig.2H). (ii) Such hydrodynamic description is insensitive to specific microscopic rules (eg the majority rule for the phenotypic switch, or alignment rule), and in principle can be applied to a broad range of binary cell mixtures, as we demonstrate in the Supplementary Material - Hydrodynamic model. This finally shows the robustness of our findings that the local aligning interactions of control cells with RAB5A cells, akin to a phenotypic switch, can promote the emergence of a flocking phase at fractions ϕ close to the geometric percolation threshold.

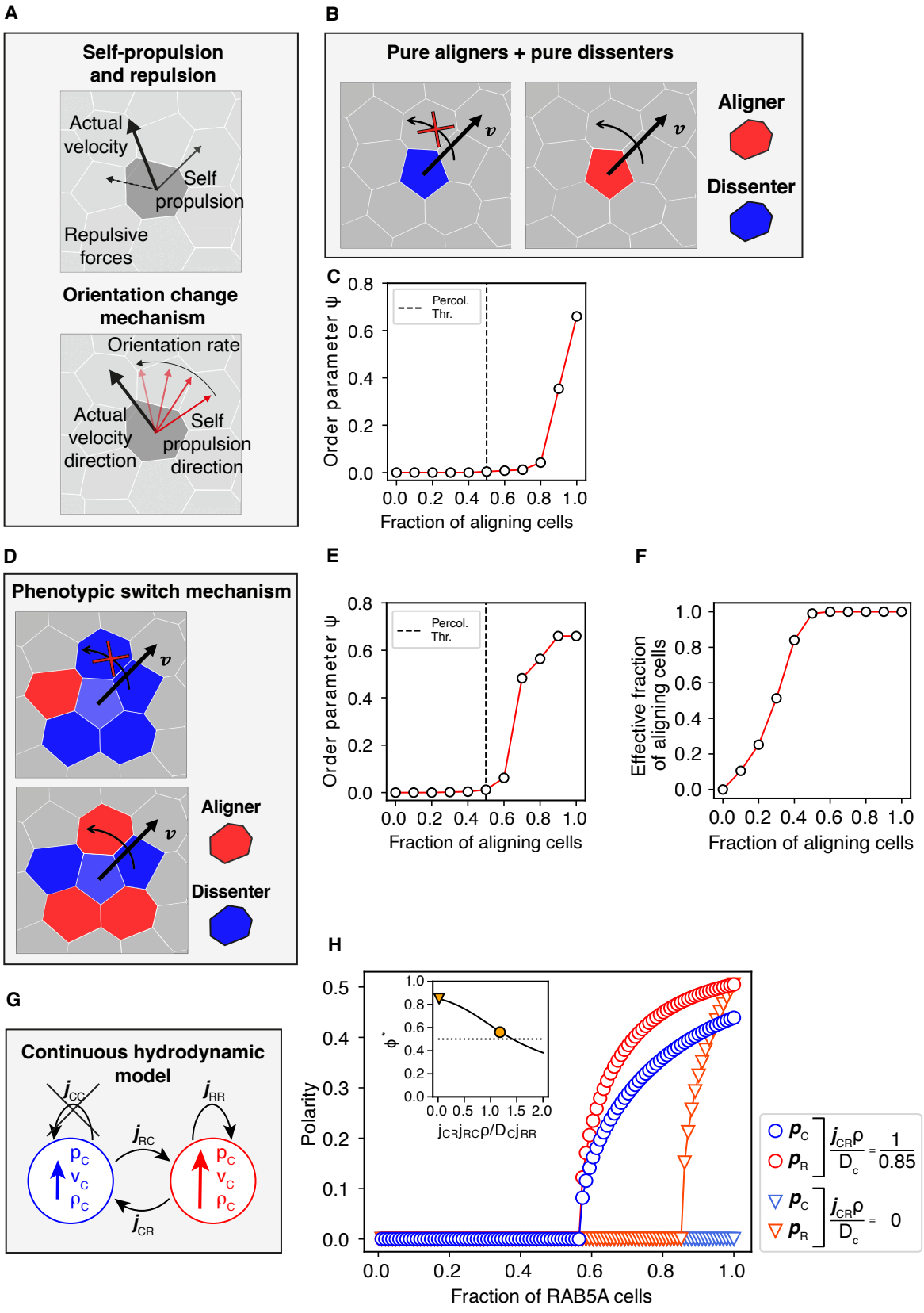

A
Self-propulsion and repulsion
Actual velocity
Self propulsion
Repulsive forces
Orientation change mechanism
Orientation rate
Actual velocity direction
Self propulsion direction
B
Pure aligners + pure dissenters
v
Aligner
Dissenter
C
Order parameter ψ
Percol. Thr.
Fraction of aligning cells
D
Phenotypic switch mechanism
Aligner
Dissenter
E
Order parameter ψ
Percol. Thr.
Fraction of aligning cells
F
Effective fraction of aligning cells
Fraction of aligning cells
G
Continuous hydrodynamic model
H
Polarity
Fraction of RAB5A cells

Figure 2: A phenotype switching mechanism accounts for the emergence of flocking behavior in heterogeneous cellular systems.

(A) Schematics of the agent-based model. Top panel illustrates the mechanism of self-propulsion and repulsion. Each particle moves with a self-propulsion velocity $v_0\mathbf{n}$, while interacting with neighboring particles through repulsive forces $\sum_j F_j$. The resulting actual velocity of the particle is the combined effect of self-propulsion and repulsion from neighbors. Bottom panel shows the orientation change mechanism. The particle adjusts its self-propulsion direction n (red arrows) towards its actual velocity direction ψ (black arrow), with an orientation rate Γ. Randomness in the orientation is introduced by the noise term (not shown), affecting how accurately the self-propulsion direction aligns with the actual velocity. (B) In the basic definition of the model, controls are considered as non-aligning cells (dissenters), which display random motion, while RAB5A-cells are efficiently aligning cells (aligners), which display highly coordinated migratory behavior. (C) Polar order parameter ψ as a function of the fraction ϕ of aligning cells in mixed monolayer of aligners and dissenters. A relatively small fraction of dissenters (about 10%) is enough to disorder the flocking motion and suppress long-range orientational order. (D) Schematics of the phenotypic switch mechanism: based on a "majority rule", dissenters can acquire the ability to efficiently align their self-propulsion along the direction of the velocity when the majority of their first neighbors is represented by aligners. (E) Polar order parameter ψ as a function of the fraction ϕ of aligning cells in a mixed monolayer of aligners and dissenters with a phenotypic switch mechanism. (F) Effective fraction of aligning cells as a function of the fraction ϕ of aligning cells in a mixed monolayer of aligners and dissenters with a phenotypic switch mechanism. The effective fraction corresponds to the sum of the number of aligners and the number of "converted" dissenters, normalized by the total number of cells. (G) Main parameters of the hydrodynamic model of cell mixtures. Each cell type $i = R, C$ is characterized by its local density ρ_i, normalized cell polarity p_i, and velocity v_i. The phenomenological coupling parameters j_{ij} account for the strength of the torque that aligns the polarity of cell i with that of a neighboring cell j. Self-couplings j_{CC} and j_{RR} control the flocking transition of homogeneous systems: the absence of flocking transition for CTRL cells only ($\phi = 0$) is captured by $j_{CC} = 0$, while $j_{RR} > D_R/\rho$ yields a flocking phase for RAB5A cells only ($\phi = 1$). In uniform phases, we assume that ϕ is constant, and assume large cell/cell friction forces so that ensure $v_R = v_C \propto p_C \propto p_R$. (H) Flocking transition as predicted by the hydrodynamic model: the average polarity of RAB5A (p_R) and CTRL (p_C) cells increases beyond

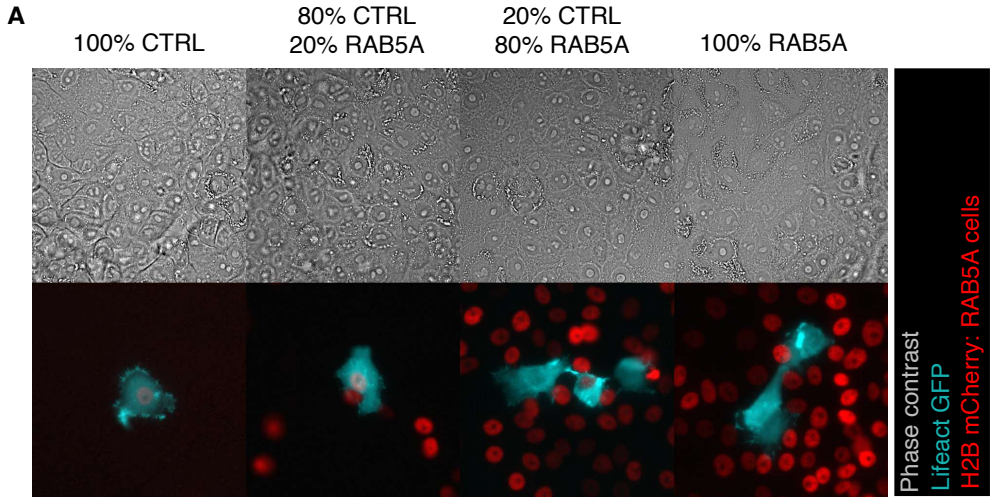
406 a critical value ϕ^* of the fraction of RAB5A cells. Triangles model the case of RAC1(T17N) domi-
407 nant negative control cells, for which we set $j_{CR} = 0$ (dissenters). In this case the model yields
408 $\frac{j_{RR}\rho}{D_R} = \frac{1}{\phi^*}$ (see SI), which sets the value of $\frac{j_{RR}\rho}{D_R}$ by using the experimental value $\phi^* \approx 0.85$. We
409 set $D_R = D_C$ for simplicity. For WT control cells (circles), we use the same value of $\frac{j_{RR}\rho}{D_R}$ and
410 set $j_{RR} = j_{RC} = j_{CR}$. Remarkably, this yields $\phi^* \approx \phi_p \approx 0.5$, in agreement with experiment.
411 The inset shows the dependence of ϕ^* on j_{CR}, the other parameters being fixed as above; the
412 case of RAC1(T17N) control cells ($j_{CR} = 0$) is indicated by the triangle, the case of WT control
413 cells ($j_{CR} = j_{RR}$) by the disk.

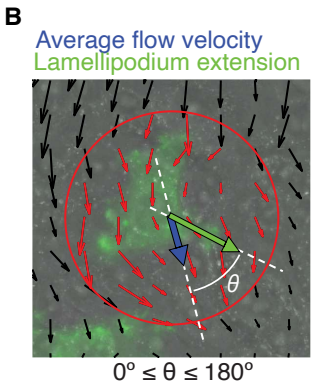
2.4 Experimental validation of the phenotypic switch mechanism for the emergence of flocking transition

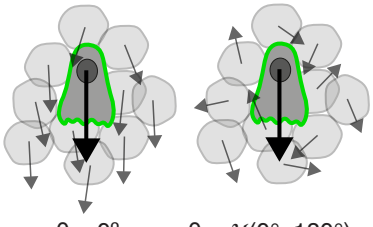
Theoretical modeling of mixed monolayers composed of cells with different dynamic properties predicts that the flocking transition can occur close to the percolation transition of aligning RAB5A cells only if, otherwise dissenting, controls are allowed to switch their migratory phenotype according to the local environment. They also predict that flocking behavior could not emerge if true dissenters were insensitive to the local environmental cues provided by the presence of a majority of fluid and aligner RAB5A-expressing cells. We tested both these predictions experimentally using two orthogonal approaches. Firstly, we set out to directly visualize the occurrence of a phenotypic migratory switch of control dissenter cells when surrounded by a majority of RAB5A aligners cells. We previously showed that RAB5A-dependent flocking-fluid transition critically relies on the ability of these cells to efficiently reorient and align their velocity vector along that of their neighbors [19, 20]. This is mediated by the extension of migratory protrusions that extend underneath neighboring cells in densely packed monolayers, named cryptic lamellipodia [38]. Cryptic lamellipodia are primarily composed of dynamic actin-branched networks controlled by the small GTPase RAC1 and drive cell motility by pushing the membrane forward and generating traction forces on the substrate. Importantly, the orientation of lamellipodia extension is a crucial parameter in determining the emergence of flocking and can be used as a proxy of cell orientation and directional velocity of each cell. We used live-cell imaging to capture the dynamics and orientation of cryptic lamellipodia in mixed monolayers of cells mosaically expressing Lifeact-GFP (Fig.3A). To analyze this parameter, we developed a pipeline that determines the angle between the manually-defined direction of lamellipodia extensions and the local average velocity vector, as determined by PIV (Fig.3B). In homogeneous cell populations composed entirely of control or RAB5A cells, we observed distinct behaviors. Control cells extended cryptic lamellipodia randomly, while RAB5A cells formed highly coordinated protrusions oriented in the direction of the local motion (Fig.3C). However, in mixed populations where control cells were surrounded by a majority of RAB5A cells - allowing the formation of a percolating cluster and the onset of flocking fluid motility – controls also acquired the ability to extend cryptic lamellipodia along the direction of supracellular motility streams (Fig.3D and Supplementary Movie 4). Conversely, below this threshold, lamellipodia in control cells were randomly oriented, in line with their uncoordinated mode of motion and lack of flocking. Thus,

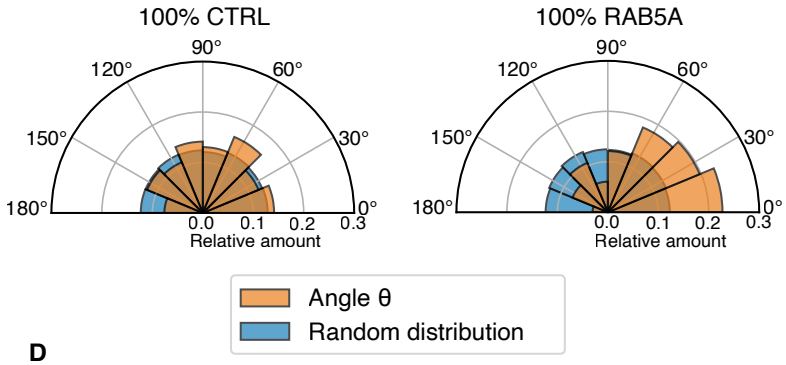
control cells in mixed monolayers above the RAB5A percolation threshold actively contribute to flocking through the dynamic extension of cryptic lamellipodia.

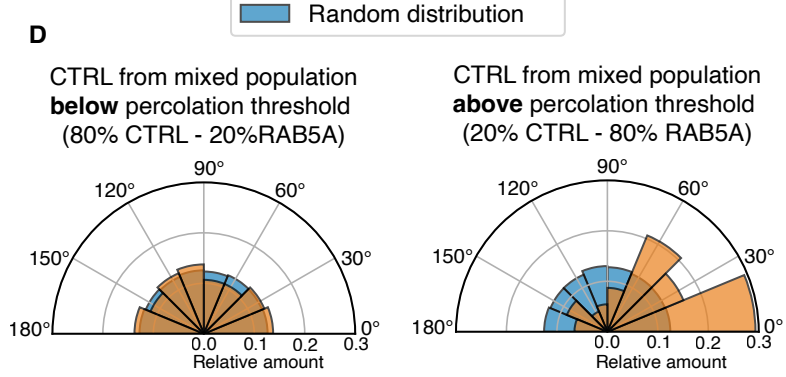
Secondly, we aimed to make control dissenter cells unable to reorient their velocity vector as a function of the number of RAB5A neighbors. We reasoned that this could be achieved by preventing the formation of cryptic lamellipodia through the blockade of the activity of the critical RAC1 GTPases essential for actin-based protrusion through the activation of the WAVE-Arp2/3 complex [39, 40]. To this end, we genetically engineered control MCF10DCIS.com cells to express a doxycycline-inducible RAC1(T17N) mutant protein, which is locked in its GDP inactive state and sequester guanine nucleotide exchange factors essential for the activation of GTPases, thereby acting as a dominant-negative (DN) [41]. We generated mixed monolayers of RAC1(T17N) controls and RAB5A cells. The expression of the transgene was verified by immunoblotting (Supplementary Fig.3B). Next, we measured motility parameters, including the mean velocity of the center of mass V_{CM}, polar order parameter ψ, length of correlation L_{corr}, and length of persistence L_{pers} (Fig.3E and Supplementary Movie 5). In the absence of RAB5A cells ($\phi = 0$), the kinetics of RAC1(T17N) controls is undistinguishable from the one displayed by WT controls (Supplementary Fig.3D). However, unlike mixed monolayers comprising phenotypically switchable WT controls, RAC1(T17N)-monolayers failed to exhibit a flocking transition at the percolation threshold (Fig.3E), indicating that even a minor fraction of true dissenters could prevent the flocking behavior typically induced by RAB5A cells. Our results also showed that the root mean square velocity V_{rms} of RAC1(T17N) control monolayers was consistently lower than that of RAB5A cells across all mixtures of control and RAB5A cells. In contrast, WT control monolayers displayed V_{rms} values similar to RAB5A cells (Supplementary Fig.3C). This indicates that the expression of RAC1(T17N) effectively prevented efficient locomotion of control cells which became insensitive to their neighbors and failed to undergo a phenotypic switch preventing the emergence of flocking at the percolation threshold as predicted by theoretical modeling. Altogether these results suggest that control cells in mixed monolayers above the RAB5A percolation threshold actively contribute to collective flocking through the dynamic extension of cryptic lamellipodia and further corroborate the results obtained through numerical simulations and biophysical modeling.


A
100% CTRL
80% CTRL
20% RAB5A
20% CTRL
80% RAB5A
100% RAB5A
Phase contrast
Lifeact GFP
H2B mCherry: RAB5A cells


B
Average flow velocity
Lamellipodium extension
θ
0° ≤ θ ≤ 180°


θ ≈ 0°
θ ~ 𝒰(0°, 180°)


C
100% CTRL
100% RAB5A
90°
120°
60°
150°
30°
180°
0°
0.0
0.1
0.2
0.3
Relative amount
Angle θ
Random distribution


D
CTRL from mixed population
below percolation threshold
(80% CTRL - 20%RAB5A)
CTRL from mixed population
above percolation threshold
(20% CTRL - 80% RAB5A)
90°
120°
60°
150°
30°
180°
0°
0.0
0.1
0.2
0.3
Relative amount

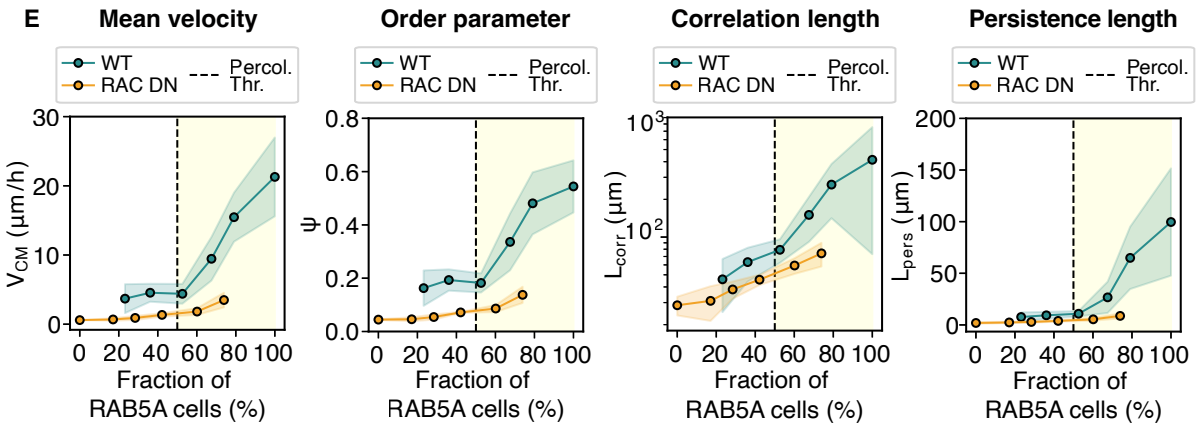

E
Mean velocity
Order parameter
Correlation length
Persistence length
WT
RAC DN
Percol. Thr.
V_{CM} (µm/h)
Ψ
L_{corr} (µm)
L_{pers} (µm)
Fraction of RAB5A cells (%)

Figure 3: Control cells switch their motility phenotype as a function of local cellular composition.

(A) Representative snapshots of phase-contrast and fluorescent images from time-lapse movies of cryptic lamellipodia extension in mixed control and RAB5A-MCF10DCIS.com monolayers. Control or RAB5A-cells expressing GFP-LifeAct were mixed (1:10 ratio) with non-expressing cells to correctly visualize actin-based cryptic lamellipodia. (B) Image representation of the angle θ between the direction of each cryptic lamellipodia and the local direction of the migrating cell sheet, as measured by PIV. $\theta \simeq 0$ indicates that protrusions and collective migration have the same direction; if the distribution of θ angles is random between 0° and 180° indicates that there is no not a clear correlation between the directions of protrusions and collective migration. (C) Quantification of the orientation angle θ in control or RAB5A-expressing MCF10DCIS.com monolayers. Data are the mean (n = more than 50 cells per condition from 3 independent experiments). (D) Quantification of the orientation angle θ in control or RAB5A-expressing MCF10DCIS.com cells from mixed populations, as indicated. Data are the mean (n = more than 50 cells per condition from 3 independent experiments). (E) Motility parameters plotted as a function of the relative amount of RAB5A-MCF10DCIS.com cells obtained by nuclear tracking of mixed monolayers monitored by time-lapse microscopy. Motility parameters are evaluated over a ~ 10 hours time window centered on the peak of motility of RAB5A cells. Teal dots are mixed monolayers composed of RAB5A cells and WT controls, while gold dots are mixed monolayers composed of RAB5A cells and control cells expressing RAC1(T17N), a mutant dominant-negative (DN) form of RAC1. Mean velocity of the center of mass (V_{cm}), polar order parameter ψ, length of correlation (L_{corr}), obtained from stretched exponential fits on spatial velocity correlation function curves, length of persistence (L_{pers}). Data are the mean $\pm$ S.D (n = 15 fields of view from 3 independent experiments).

2.5 Heterotypic cell interactions and RAB5A expression control cell shape in mixed monolayers and breast cancer tissues

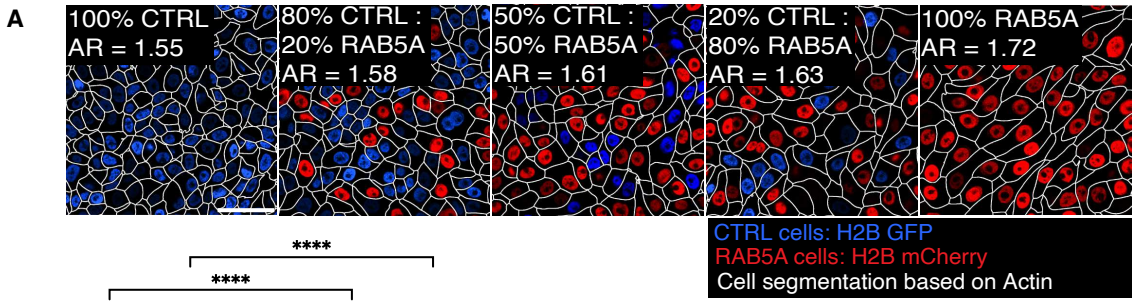
The presence of a phenotypic switch mechanism governed by the local environment, assumed in our theoretical model and confirmed experimentally, points to the existence of a mechano-chemical communication between control and RAB5A cells, suggesting that heterotypic cell-cell interactions in heterogeneous monolayers influence individual cell properties, and may further impact cell state and fate. Increasing evidence indicates that abrupt changes in tissue material properties leading to phase transition and the emergence of flocking-fluid motion are associated with continuous smooth variations in individual cell shape geometric parameters [8, 15]. Within this framework, jammed and solid tissues typically exhibit reduced cell shape, captured by the shape index ($\frac{perimeter}{\sqrt{area}}$) or the cell aspect ratio (AR), defined as the ratio of a cell's long axis to its short axis, as well as their variance. Increased cell shape or AR value above a critical threshold parameter are invariably associated with an abrupt PT toward a fluid unjammed dynamic state of the entire tissue. We, therefore, ask whether a similar relationship between local cell shape parameters and global tissue dynamic state is at play in mixed monolayers and what could be the wider pathobiological consequences in heterogeneous tumors. To this end, we began by analyzing geometric shape parameters in mixed MCF10DCIS.com monolayers containing varying fractions of RAB5A-expressing cells. We acquired confocal images of monolayers, using Phalloidin staining to label the actin cytoskeleton, and used the Cellpose segmentation tool [42] to extract geometric parameters of thousands of cells. Nuclei from controls or RAB5A-expressing cells were separately identified by exploiting the differential H2B-GFP or H2B-mCherry nuclear fluorescent markers and masks of cell borders were specifically associated with each nucleus. Using this strategy, we could independently segment control and RAB5A cells and consequently measure shape parameters from each of the two cell populations simultaneously (Supplementary Fig.4A). We specifically focused on cell AR. In control monolayers, cells exhibited a cobble-like shape with low AR, consistent with a densely packed, immotile epithelial state. In contrast, RAB5A cells display an elevated AR, corresponding to a more elongated and fluid-like cell system (Fig.4A,B). In mixed populations, the AR of control cells displays a roughly linear increase as a function of RAB5A cell fraction, becoming particularly prominent above the percolation and flocking-fluid motility threshold. Below this threshold, RAB5A cells retained a more isotropic shape, similar to controls, indicating that cell elongation and fluidity

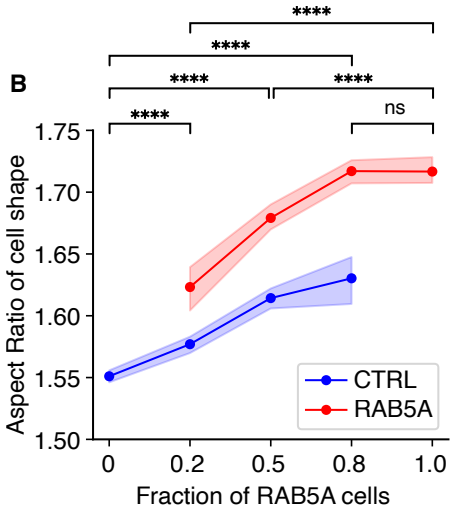
are strictly associated with the local density of RAB5A cells. Importantly, the linear increase in AR correlated with the progressive elevation in the amplitude of mutual cell displacements and uncoordinated velocity fluctuations (captured by V_{rms}) measured by the analysis of cell motility (Fig.1B). Cell shape has been interpreted as the outcome of the competition between cell-cell adhesive strength and tension at the level of the junctions. The shape transition we observed in mixed monolayers above the percolation threshold might, thus, suggest that control cells surrounded by fluidized RAB5A cells undergo a change in their junctional state and dynamics, which ultimately impacts junctional forces and tension, determining a switch towards a more fluid-like, unjammed phase of the tissue. Thus, we conclude that feedback-positive interactions are at play between kinetically arrested and highly motile cells such that the former acquire morpho-phenotypic features of the latter as a function of their surrounding cells and are transformed into active aligners.

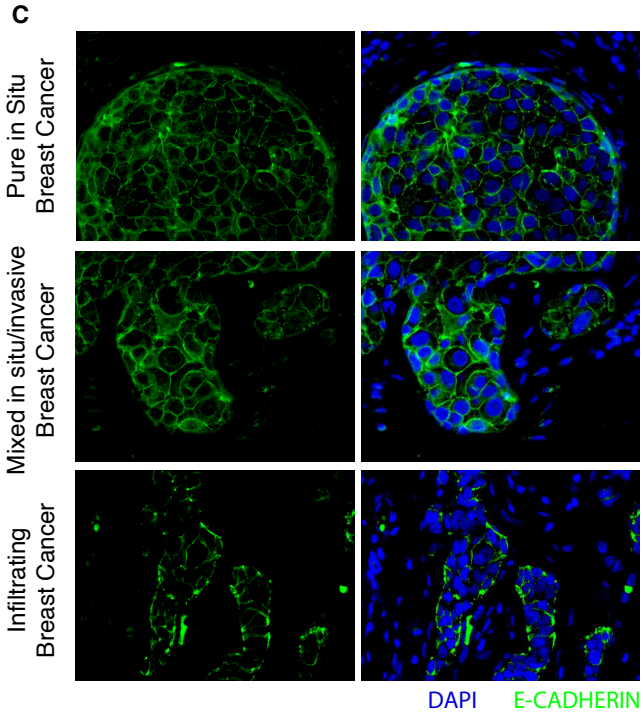
To test whether shape changes in mixed monolayers could also be captured in a pathologically relevant condition during human breast cancer progression from early, quasi benign DCIS to IDC, we analyzed a cohort of pure DCIS, DCIS with local areas of infiltration and overt IDC (Fig.4C). We used an imaging pipeline that extracts shape descriptors of nuclei by Stardist-based segmentation [43] and of cells by Voronoi tessellation (Supplementary Fig.4B). We found that pure indolent DCIS displayed lower AR, indicative of a jammed, rigid state, whereas the AR increased progressively in locally infiltrative DCIS and became significantly higher in IDC, correlating higher AR with increased tissue fluidity and aggressiveness (Fig.4D).

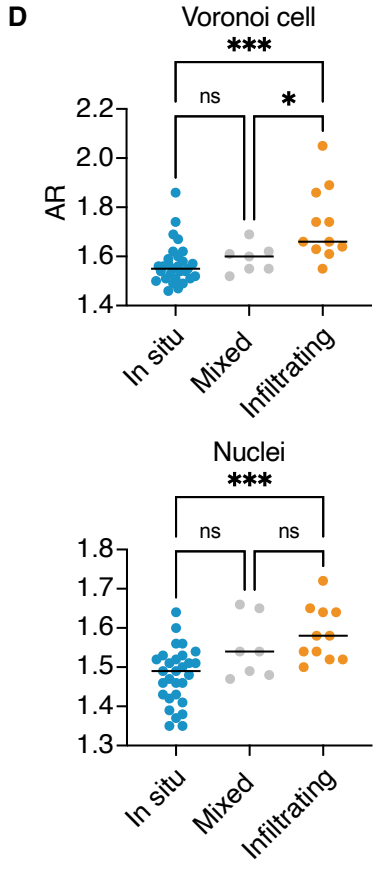
Next, we focused on DCIS lesions with micro-invasive foci. Using both immunohistochemical and multiplex immunohistochemistry/Immunofluorescence (mIHC/IF) analysis, we had previously reported a heterogeneous distribution of RAB5A in these lesions [20]. Consistently, we now show that RAB5A displays a graded increase in expression toward the invasive front and poor or no expression in the tumor bulk (Supplementary Fig.4C). We automatically segmented breast cancer cell nuclei using the Stardist tool and extracted nuclei AR in the bulk and in the invasive RAB5A+ front. We found that nuclei of tumor cells located on the invasive front display an increased AR that is significantly higher compared to the nuclei AR of tumor cells in the bulk, indicative of a system undergoing a gradual solid-to-fluid-like transition (Fig.4E). This set of findings indicates that breast cancer is characterized by inter- and intra-tumor mechanical heterogeneity and that alterations in tissue fluidity might confer breast cancer cells aggressive

properties.


A
100% CTRL
AR = 1.55
80% CTRL :
20% RAB5A
AR = 1.58
50% CTRL :
50% RAB5A
AR = 1.61
20% CTRL :
80% RAB5A
AR = 1.63
100% RAB5A
AR = 1.72
CTRL cells: H2B GFP
RAB5A cells: H2B mCherry
Cell segmentation based on Actin


B
****
****
****
****
****
ns
Aspect Ratio of cell shape
1.75
1.70
1.65
1.60
1.55
1.50
0
0.2
0.5
0.8
1.0
Fraction of RAB5A cells
CTRL
RAB5A


C
Pure in Situ Breast Cancer
Mixed in situ/invasive Breast Cancer
Infiltrating Breast Cancer
DAPI
E-CADHERIN


D
Voronoi cell
***
ns
*
AR
2.2
2.0
1.8
1.6
1.4
In situ
Mixed
Infiltrating
Nuclei
***
ns
ns
1.8
1.7
1.6
1.5
1.4
1.3
In situ
Mixed
Infiltrating

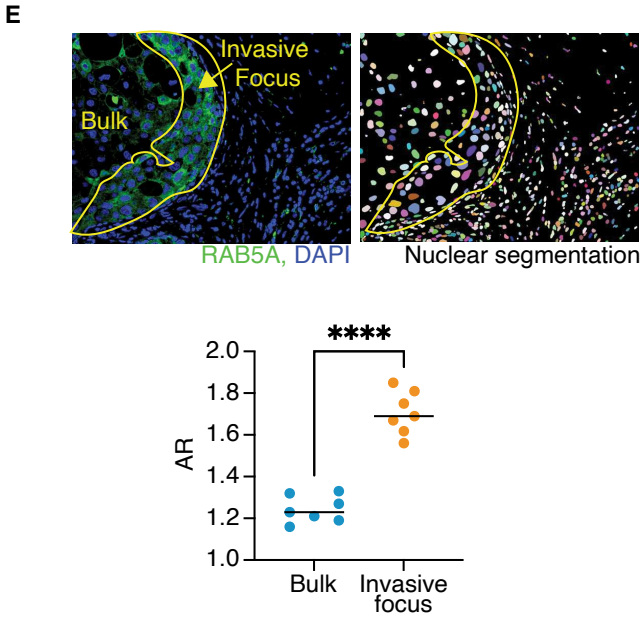

E
Invasive
Focus
Bulk
RAB5A, DAPI
Nuclear segmentation
****
AR
2.0
1.8
1.6
1.4
1.2
1.0
Bulk
Invasive
focus

Figure 4: In heterogeneous monolayers and breast cancer tissues, cell shape is controlled by RAB5A expression and local cellular composition.

(A) Representative confocal immunofluorescence images of control and RAB5A-expressing MCF10DCIS.com cells seeded at various relative ratios to form confluent mixed monolayers. White cell borders are resulting from Cellpose segmentation based on Phalloidin staining. The AR indicated in black boxes refers to control or RAB5A-cells from pure populations or to control cells from mixed populations. Scale bar $50\,\mu$m. (B) Aspect ratio (AR) of control or RAB5A-MCF10DCIS.com cells in mixed monolayers as a function of the relative number of RAB5A-expressing cells. Data are the median $\pm$ 95% confidence interval from 3 independent experiments. (From left to right, number of CTRL cells = 36246, 28963, 18478, 5879; number of RAB5A cells = 4291, 13907, 20551, 14384). Dunn's multiple comparison test (ns: p>0.9999; ****: p<0.0001). (C) Representative multiplex immunohistochemistry/immunofluorescence images of DAPI (blue) and E- CADHERIN (green) in human pure DCIS, mixed in situ/invasive DCIS and infiltrating BC. (D) Voronoi cells (top) and nuclear (bottom) aspect ratio (AR) plotted as a function of cancer state, referred to panel C. Each dot is a field of view (n = 4 human BC cases per condition). Tukey's multiple comparison test (Top, ***: p=0.0001; bottom, ***: p=0.0005). (E) Top: representative human DCIS with micro-invasive focus. Multiplex immunohistochemistry/immunofluorescence, RAB5A (green) and DAPI and nuclear segmentation using Stardist of BC cells from human DCIS with micro-invasive focus. Bottom: Nuclear aspect ratio (AR) plotted as a function of DCIS region (tumour bulk or invasive focus). Each dot is the mean nuclear AR from 7 human DCIS cases. Black line is the mean. Two- tailed unpaired t-test (****: p<0.0001).

2.6 Percolation and flocking transitions set chemo-mechanical communication and transcriptional reprogramming in mixed monolayers and 3D Spheroids

Lastly, we investigated whether the morpho-phenotypic transformation of control cells in mixed monolayers impacted their transcriptional state. Cells in tissues are subjected to a range of mechanical deformations and biochemical signals, especially during tumor progression. Changes in cellular morphology can trigger intracellular responses, resulting in dynamic adaptations that involve alterations in the cellular transcriptional state. Endocytic-dependent flocking-fluid motion triggered by RAB5A overexpression can induce wholesale transcriptional rewiring toward a cGAS/STING-mediated innate immunity gene program, akin to a cytosolic DNA response (CytoDR) signature [22]. We hypothesized that control cells may undergo a similar transcriptional reprogramming, particularly above the RAB5A-cells percolation and flocking threshold. To test this possibility, we used mixed monolayers below (80% controls, 20% RAB5A) and above (20% controls, 80% RAB5A) the percolation threshold of RAB5A cells. After observing the onset of flocking above the percolation threshold, we exploited the different nuclear fluorescent labels of the two cell populations to separate them through FACS sorting. We then performed RNA-sequencing (RNA-seq) on the isolated control cells, and we compared their transcriptome with that of pure control and RAB5A-monolayers (Supplementary Fig.5A-D). Compared with controls in homogeneous monolayers, control cells in mixed populations above the percolation threshold exhibited upregulation of interferon-stimulated genes (ISGs), while expression levels below the threshold were similar to pure controls (Fig.5A). Gene set enrichment analysis (GSEA) further confirmed that ISGs were the most significantly enriched genes in control cells above the percolation threshold, similarly to homogeneous RAB5A monolayers (Supplementary Fig.5E). Interestingly, even below the percolation threshold of RAB5A cells, controls exhibited a smaller yet significant enrichment in ISG expression, indicating that a low fraction of RAB5A cells is sufficient to alter the transcriptome of controls in mixed monolayers. Importantly, we rigorously controlled that the increase in ISG expression levels was not the result of contamination of RAB5A-cells into control-sorted populations. We did that through post-sorting analysis of residual H2B-mCherry-tagged RAB5A cells in control populations and by qRT-PCR analysis of RAB5A mRNA levels (Supplementary Fig.6). Both analyses revealed minimal levels of residual RAB5A-cells in the FACS-sorted controls from mixed monolayers.

We corroborated these findings by quantifying the expression levels of a subset of ISGs by

qRT-PCR analysis (Fig.5B,C). We specifically used mixed monolayers composed of increasing fractions of RAB5A cells, we separated control and RAB5A-cells by FACS sorting and analyzed ISG expression levels in the two cell populations. Consistent with RNA-seq data, ISGs showed increased expression in control cells from mixed monolayers above the percolation threshold compared to homogeneous controls, with levels positively correlating with the fraction of RAB5A cells (Fig.5B). Conversely, ISG expression in RAB5A cells declined in mixed populations with higher control cell fractions, suggesting an inverse relationship (Fig.5C).

To further validate our model in a more relevant pathological setting, we extended our investigation to 3D spheroids composed of mixed populations of MCF10DCIS.com cells. We used Aggrewell plates to form mixed spheroids consisting of control and RAB5A-overexpressing cells, either below (80% control – 20% RAB5A) or above (20% control – 80% RAB5A) the 50% threshold. After 48 hours, the spheroids were disaggregated, and the two cell populations were separated using FACS sorting (Fig.5D). Quantitative analysis of ISG mRNA expression revealed a consistent increase in inflammatory transcripts in RAB5A-spheroids (Fig.5F), consistent with previous findings [22]. Similar to 2D monolayers, RAB5A cells from spheroids with $\phi < 50\%$ exhibited decreased ISG expression levels (Fig.5F). Notably, control cells in spheroids with ϕ above the 50% threshold, but not below, also showed increased ISG expression (Fig.5E).

Together, these findings indicate that the flocking transition, coinciding in 2D with the percolation transition of RAB5A-expressing cells, drives a morpho-phenotypic transformation and robust transcriptional rewiring toward interferon gene program in naïve control cells. This suggests that chemo-mechanical mechanisms between control and RAB5A cells underlie these changes and govern cell-cell communication in mixed monolayers.

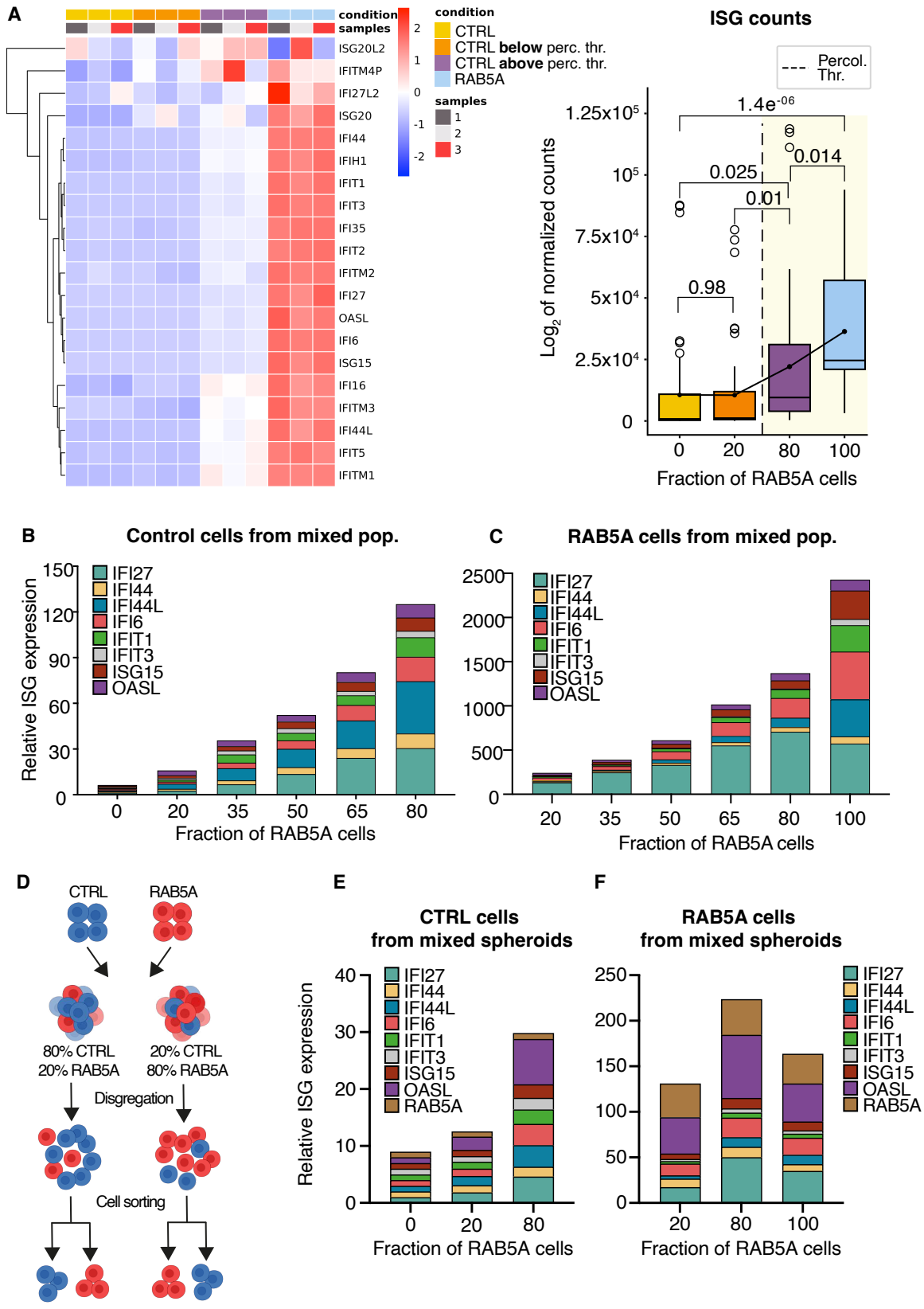

A
condition
samples
ISG20L2
IFITM4P
IFI27L2
ISG20
IFI44
IFIH1
IFIT1
IFIT3
IFI35
IFIT2
IFITM2
IFI27
OASL
IFI6
ISG15
IFI16
IFITM3
IFI44L
IFIT5
IFITM1
condition
CTRL
CTRL below perc. thr.
CTRL above perc. thr.
RAB5A
samples
1
2
3
ISG counts
Percol. Thr.
1.4e-06
0.025
0.01
0.014
0.98
Log2 of normalized counts
Fraction of RAB5A cells
B
Control cells from mixed pop.
Relative ISG expression
IFI27
IFI44
IFI44L
IFI6
IFIT1
IFIT3
ISG15
OASL
Fraction of RAB5A cells
C
RAB5A cells from mixed pop.
Fraction of RAB5A cells
D
CTRL
RAB5A
80% CTRL
20% RAB5A
20% CTRL
80% RAB5A
Disgregation
Cell sorting
E
CTRL cells
from mixed spheroids
Relative ISG expression
RAB5A
Fraction of RAB5A cells
F
RAB5A cells
from mixed spheroids
Fraction of RAB5A cells

Figure 5: Percolation and flocking transitions set transcriptional reprogramming in mixed monolayers and 3D spheroids.

(A) Left: heatmap of the normalized counts from RNA-sequencing of ISGs identified in each of the 3 replicates of pure control (CTRL), pure RAB5A-expressing (RAB5A)-MCF10DCIS.com monolayers and controls isolated from mixed monolayers below or above the percolation threshold of RAB5A cells. Normalized expression has been calculated for each gene starting from DESeq2 log2-transformed expression value and then normalized by row mean values. Right: boxplot of ISGs-associated log2 transformed DESeq2 normalized counts for each sample. Two-tailed unpaired t-test, p-values are indicated in the figure. (B) mRNA relative expression levels of the indicated ISGs determined by qRT-PCR in control and RAB5A-overexpressing (C) MCF10DCIS.com cells isolated by FACS sorting from mixed monolayers at the indicated relative composition. Values were normalized to 100% control monolayers. Each column is the mean (n=3 independent experiments). (D) Schematics of the experimental procedure: mixed spheroids consisting of control (CTRL) and RAB5A-overexpressing (RAB5A) cells, either below (80% control – 20% RAB5A) or above (20% control – 80% RAB5A) the critical percolation threshold were formed. After 48 hours, the spheroids were disaggregated, and the two cell populations were separated using FACS sorting. mRNA expression levels of the indicated ISGs determined by qRT-PCR in CTRL (E) and RAB5A (F) cells isolated by FACS sorting. Values were normalized to 100% control spheroids and are the mean $\pm$ SD (n=2 independent experiments).

To gain initial clues as to the potential mechanisms underlying the mechano-chemical communication of cells in mechanically heterogeneous populations, we first assessed whether RAB5A-fluidized cells secrete pro-inflammatory factors, which might trigger in a paracrine fashion the activation of a cytosolic DNA response in controls. Notably, control cells treated with conditioned media from RAB5A monolayers displayed elevated mRNA levels of CytoDR-responsive and ISG genes (Fig.6A). SILAC-based mass spectrometry of the RAB5A cell secretome further revealed a consistent upregulation of proteins enriched in pathways typically associated with innate immune responses, particularly interferon and cytokine signaling (Fig.6B,C). These data suggest that RAB5A-mediated tissue fluidification elicits a pro-inflammatory microenvironment that influences in a paracrine fashion the transcriptional state of nearby cells.

We noticed, however, that ISG upregulation in control cells treated with conditioned medium was quantitatively much lower than in control cells that had been mixed with RAB5A cells above the percolation threshold (Fig.6D). This finding indicates that the majority rule phenotypic switch might be the overarching determinant for the transcription rewiring of control cells in mixed monolayers. They further point to the role of direct cell-cell contact for full transcriptional dysregulation.

To test this further, we compared homogeneous populations of control and RAB5A cells at varying cell densities (Fig.6E), monitoring ISG expression levels by qRT-PCR and motility via time-lapse microscopy (Supplementary Movie 6). The emergence of flocking fluid locomotion in RAB5A cells, measured by the mean velocity V_{CM} and the root mean squared velocity V_{rms}, was strongly dependent on cell density and coincided with the formation of interconnected percolating cell clusters (Fig.6F,G). Notably, ISG expression levels as a function of seeding density correlated with the emergence of percolating interconnected cell clusters and the activation of flocking collective motion (Fig.6H). These findings indicate that flocking migration, which also in this subconfluent case is set by contact percolation, significantly impacts ISG activation, suggesting that both paracrine soluble signaling and contact-dependent, cell-cell interaction and dynamic state are at the basis of a chemo-mechanical communication switch in heterogeneous cell assemblies.

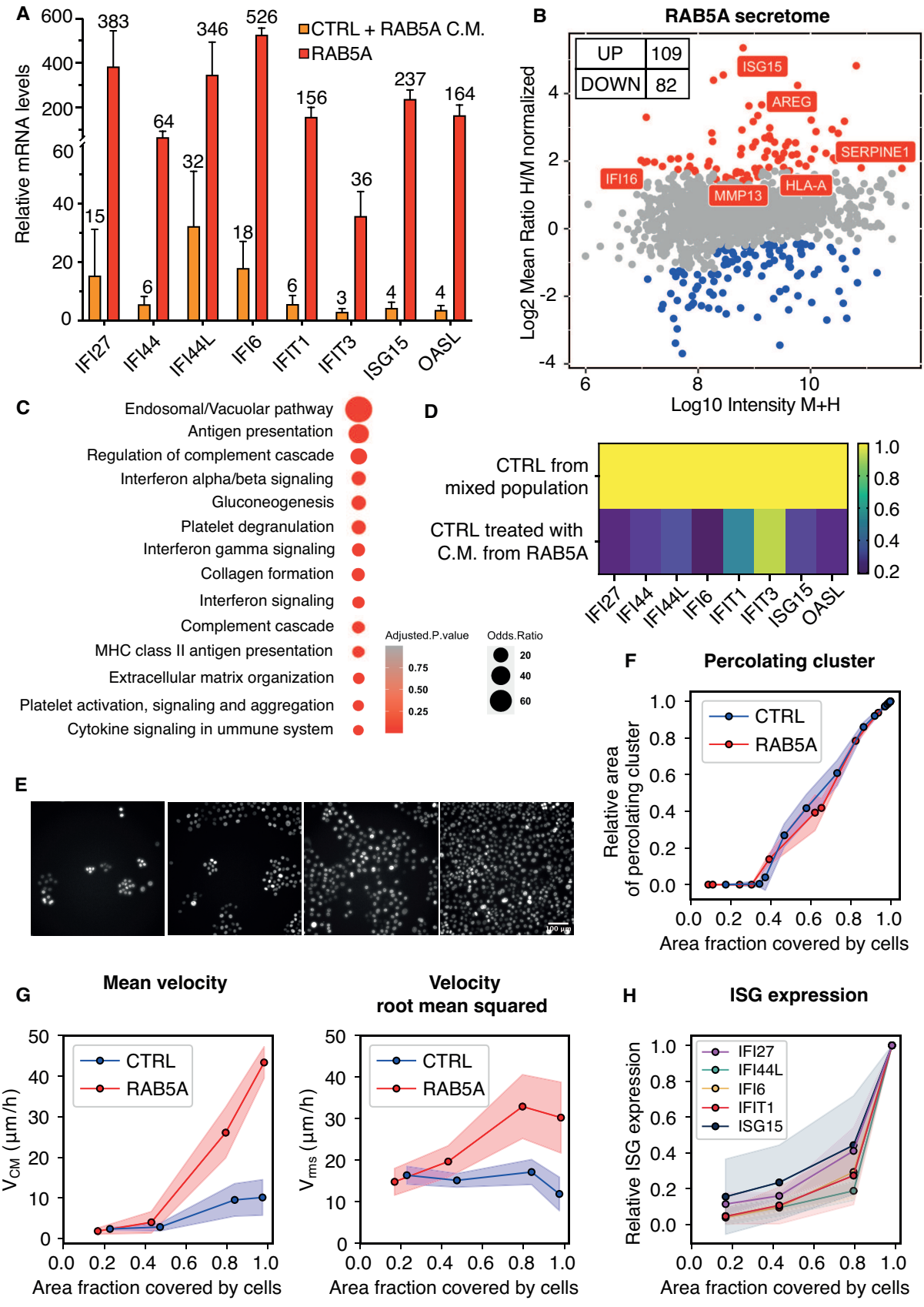

A
Relative mRNA levels
CTRL + RAB5A C.M.
RAB5A
IFI27
IFI44
IFI44L
IFI6
IFIT1
IFIT3
ISG15
OASL
B
RAB5A secretome
UP 109
DOWN 82
ISG15
AREG
SERPINE1
IFI16
MMP13
HLA-A
Log2 Mean Ratio H/M normalized
Log10 Intensity M+H
C
Endosomal/Vacuolar pathway
Antigen presentation
Regulation of complement cascade
Interferon alpha/beta signaling
Gluconeogenesis
Platelet degranulation
Interferon gamma signaling
Collagen formation
Interferon signaling
Complement cascade
MHC class II antigen presentation
Extracellular matrix organization
Platelet activation, signaling and aggregation
Cytokine signaling in ummune system
Adjusted.P.value
Odds.Ratio
D
CTRL from mixed population
CTRL treated with C.M. from RAB5A
E
F
Percolating cluster
Relative area of percolating cluster
Area fraction covered by cells
G
Mean velocity
Velocity root mean squared
H
ISG expression
Relative ISG expression

Figure 6: Mechano-chemical interaction between control and RAB5A cells sets a phenotypic switch.

(A) mRNA expression levels of the indicated ISGs determined by qRT-PCR in control and RAB5A-monolayers treated for 48 hours with conditioned medium from control or RAB5A-monolayers. Data are the mean $\pm$ SD (n= 5 independent experiments). (B) MA plot showing log2 fold changes as function of log10 sum normalized protein intensities of secreted proteins from control (M) and RAB5A-overexpressing (H) MCF10DCIS.com monolayers. Red and blue dots are statistically-significant upregulated (UP) and downregulated (DOWN) proteins in the RAB5A secretome, respectively. (C) Dot plot showing odds ratios as dots dimension and significance as colour of Reactome database terms, coming from deregulated proteins (from mass-spectrometry secretome analysis). (D) Heatmap of the indicated ISGs in control MCF10DCIS.com cells co-cultured with RAB5A-cells (20% CTRL – 80% RAB5A) and isolated by FACS sorting or treated with conditioned medium from the mixed population. Data are the ratio of gene expression relative to control cells co-cultured with RAB5A-cells and are the mean (n=4 independent experiments). (E) Representative widefield fluorescent images of nuclei of control and RAB5A-expressing MCF10DCIS.com cells seeded at increasing densities. Scale bar $100\,\mu$m. (F) Area of cell clusters that percolate the entire field of view relative to the area fraction covered by cells. The area of percolating cluster was evaluated over the first 5 frames of the time window used to calculate motility parameters. (G) Motility parameters of control (CTRL) or RAB5A- expressing (RAB5A) MCF10DCIS.com cells seeded at various densities plotted as a function of the area fraction covered by cells, obtained by PIV analysis of time-lapse movies. Motility parameters are evaluated over the time window 4–12 h. Data are the mean $\pm$ SD (n=15 field of views from 3 independent experiments). (Left) Mean velocity of the center of mass (V_{cm}), (right) root mean square velocity (V_{rms}). (H) Relative expression levels of the indicated ISGs of RAB5A-expressing MCF10DCIS.com cells seeded at various densities, plotted as a function of the area fraction covered by cells. Values were normalized to the controls at each dilution and expressed as a relative expression with respect to the maximal level for each ISG at the highest seeded density. Values are the mean $\pm$ SD (n=3 independent experiments).

3 Conclusion and Perspectives

Our study highlights contact percolation as a pivotal driver of chemo-mechanical feedback inducing a dramatic transition in heterogeneous breast cancer tissues, promoting both collective motility and transcriptional reprogramming. The combination of experimental and theoretical modeling approaches reveals that a phenotypic switch enables even immotile control cells to adopt motility traits from neighboring RAB5A-expressing cells, ultimately contributing to a pro-inflammatory transcriptional profile in control cells once the percolation threshold is surpassed. This mechanistic insight bridges the physical principles of phase transitions with the biological complexity of tumor invasion, offering a new framework for understanding tissue fluidity and immune modulation within the tumor microenvironment. However, further work is needed to define the precise molecular and physical mechanisms underlying this phenotypic and genetic switch. In addition, it will be necessary to explore how mechanical heterogeneity and cell signaling and specifically cell-cell-direct contact interplay in more complex, heterogeneous 3D environments and in vivo conditions, which could reveal additional regulatory elements beyond those captured in our current models. Ultimately, the insights gained here may contribute to targeted therapeutic strategies that disrupt these phase transitions, potentially inhibiting cancer progression and invasion.

References

1. Corominas-Murtra, B. & Petridou, N. I. Viscoelastic Networks: Forming Cells and Tissues. *Frontiers in Physics* **9.** ISSN: 2296-424X. (2024) (June 2021).
2. Hannezo, E. & Heisenberg, C.-P. Rigidity Transitions in Development and Disease. *Trends in Cell Biology* **32,** 433–444. ISSN: 0962-8924. (2023) (May 2022).
3. Blauth, E., Kubitschke, H., Gottheil, P., Grosser, S. & Käs, J. A. Jamming in Embryogenesis and Cancer Progression. *Frontiers in Physics* **9.** ISSN: 2296-424X. (2023) (2021).
4. Lawson-Keister, E. & Manning, M. L. Jamming and Arrest of Cell Motion in Biological Tissues. *Current Opinion in Cell Biology. Cell Dynamics* **72,** 146–155. ISSN: 0955-0674. (2022) (Oct. 2021).
5. Mongera, A. *et al.* A Fluid-to-Solid Jamming Transition Underlies Vertebrate Body Axis Elongation. *Nature* **561,** 401–405. ISSN: 1476-4687. (2023) (Sept. 2018).
6. Petridou, N. I., Corominas-Murtra, B., Heisenberg, C.-P. & Hannezo, E. Rigidity Percolation Uncovers a Structural Basis for Embryonic Tissue Phase Transitions. *Cell* **184,** 1914–1928.e19. ISSN: 0092-8674. (2023) (Apr. 2021).
7. Pinheiro, D., Kardos, R., Hannezo, É. & Heisenberg, C.-P. Morphogen Gradient Orchestrates Pattern-Preserving Tissue Morphogenesis via Motility-Driven Unjamming. *Nature Physics* **18,** 1482–1493. ISSN: 1745-2481. (2023) (Dec. 2022).
8. Atia, L. *et al.* Geometric Constraints during Epithelial Jamming. *Nature Physics* **14,** 613–620. ISSN: 1745-2481. (2023) (June 2018).
9. Oswald, L., Grosser, S., Smith, D. M. & Kas, J. A. Jamming Transitions in Cancer. *J Phys D Appl Phys* **50,** 483001. ISSN: 0022-3727 (Print) 0022-3727 (Linking) (Oct. 2017).
10. Park, J. A., Atia, L., Mitchel, J. A., Fredberg, J. J. & Butler, J. P. Collective Migration and Cell Jamming in Asthma, Cancer and Development. *J Cell Sci* **129,** 3375–83. ISSN: 0021-9533 (Print) 0021-9533 (Linking) (Sept. 2016).
11. Park, J. A. *et al.* Unjamming and Cell Shape in the Asthmatic Airway Epithelium. *Nat Mater* **14,** 1040–8. ISSN: 1476-1122 (Print) 1476-1122 (Linking) (Oct. 2015).
12. Pinheiro, D. & Mitchel, J. Pulling the Strings on Solid-to-Liquid Phase Transitions in Cell Collectives. *Current Opinion in Cell Biology* **86,** 102310. ISSN: 0955-0674. (2024) (Feb. 2024).

13. Fuhs, T. *et al*. Rigid Tumours Contain Soft Cancer Cells. *Nature Physics,* 1–10. ISSN: 1745-2481. (2022) (Sept. 2022).

14. Gottheil, P. *et al*. State of Cell Unjamming Correlates with Distant Metastasis in Cancer Patients. *Physical Review X* **13,** 031003. (2023) (July 2023).

15. Grosser, S. *et al*. Cell and Nucleus Shape as an Indicator of Tissue Fluidity in Carcinoma. *Physical Review X* **11,** 011033 (2021).

16. Ilina, O. *et al*. Cell–Cell Adhesion and 3D Matrix Confinement Determine Jamming Transitions in Breast Cancer Invasion. *Nature Cell Biology* **22,** 1103–1115. ISSN: 1476-4679. (2023) (Sept. 2020).

17. Sauer, F. *et al*. Changes in Tissue Fluidity Predict Tumor Aggressiveness In Vivo. *Advanced Science* **10,** 2303523. ISSN: 2198-3844. (2024) (2023).

18. Staneva, R. *et al*. Cancer Cells in the Tumor Core Exhibit Spatially Coordinated Migration Patterns. *Journal of Cell Science* **132,** jcs220277. ISSN: 0021-9533. (2023) (Mar. 2019).

19. Malinverno, C. *et al*. Endocytic Reawakening of Motility in Jammed Epithelia. *Nat Mater* **16,** 587–596. ISSN: 1476-1122 (Print) 1476-1122 (Linking) (May 2017).

20. Palamidessi, A. *et al*. Unjamming Overcomes Kinetic and Proliferation Arrest in Terminally Differentiated Cells and Promotes Collective Motility of Carcinoma. *Nat Mater* **18,** 1252–1263. ISSN: 1476-4660 (Nov. 2019).

21. Frittoli, E. *et al*. A RAB5/RAB4 Recycling Circuitry Induces a Proteolytic Invasive Program and Promotes Tumor Dissemination. *Journal of Cell Biology* **206,** 307–328. ISSN: 0021-9525. (2023) (July 2014).

22. Frittoli, E. *et al*. Tissue Fluidification Promotes a cGAS–STING Cytosolic DNA Response in Invasive Breast Cancer. *Nature Materials* **22,** 1–12. ISSN: 1476-4660. (2023) (May 2023).

23. Lawson, D. A., Kessenbrock, K., Davis, R. T., Pervolarakis, N. & Werb, Z. Tumour Heterogeneity and Metastasis at Single-Cell Resolution. *Nature Cell Biology* **20,** 1349–1360. ISSN: 1476-4679. (2023) (Dec. 2018).

24. Lüönd, F., Tiede, S. & Christofori, G. Breast Cancer as an Example of Tumour Heterogeneity and Tumour Cell Plasticity during Malignant Progression. *British Journal of Cancer* **125,** 164–175. ISSN: 1532-1827. (2023) (July 2021).

25. Nader, G. P. d. F. *et al*. Compromised Nuclear Envelope Integrity Drives TREX1-dependent DNA Damage and Tumor Cell Invasion. *Cell* **184,** 5230–5246.e22. ISSN: 0092-8674. (2023) (Sept. 2021).

26. Shen, Y. *et al*. Detecting Heterogeneity in and between Breast Cancer Cell Lines. *Cancer Convergence* **4,** 1. ISSN: 2366-6196. (2022) (Feb. 2020).

27. Broadbent, S. R. & Hammersley, J. M. Percolation Processes: I. Crystals and Mazes. *Mathematical Proceedings of the Cambridge Philosophical Society* **53,** 629–641. ISSN: 1469-8064, 0305-0041. (2024) (July 1957).

28. Sahini, M. & Sahimi, M. *Applications Of Percolation Theory* ISBN: 978-0-203-22153-2 (CRC Press, July 2003).

29. Amack, J. D. & Manning, M. L. Knowing the Boundaries: Extending the Differential Adhesion Hypothesis in Embryonic Cell Sorting. *Science* **338,** 212–5. ISSN: 0036-8075 (Oct. 2012).

30. Maître, J. L. *et al*. Adhesion Functions in Cell Sorting by Mechanically Coupling the Cortices of Adhering Cells. *Science* **338,** 253–6. ISSN: 0036-8075 (Oct. 2012).

31. Sahu, P. *et al*. Small-Scale Demixing in Confluent Biological Tissues. *Soft Matter* **16,** 3325–3337. ISSN: 1744-6848. (2023) (Apr. 2020).

32. Steinberg, M. S. Reconstruction of Tissues by Dissociated Cells. Some Morphogenetic Tissue Movements and the Sorting out of Embryonic Cells May Have a Common Explanation. *Science* **141,** 401–8. ISSN: 0036-8075 (Print) 0036-8075 (Aug. 1963).

33. Cerbino, R. *et al*. Disentangling Collective Motion and Local Rearrangements in 2D and 3D Cell Assemblies. *Soft Matter* **17,** 3550–3559. ISSN: 1744-6848. (2024) (Apr. 2021).

34. Alert, R. & Trepat, X. Physical Models of Collective Cell Migration. *Annual Review of Condensed Matter Physics* **11,** 77–101. ISSN: 1947-5454, 1947-5462. (2024) (Mar. 2020).

35. Giavazzi, F. *et al*. Giant Fluctuations and Structural Effects in a Flocking Epithelium. *Journal of Physics D: Applied Physics* **50,** 384003. ISSN: 0022-3727 (2017).

36. Giavazzi, F. *et al*. Flocking Transitions in Confluent Tissues. *Soft Matter* **14,** 3471–3477. ISSN: 1744-6848 (Electronic) 1744-683X (Linking) (May 2018).

37. Yllanes, D., Leoni, M. & Marchetti, M. C. How Many Dissenters Does It Take to Disorder a Flock? *New Journal of Physics* **19,** 103026. ISSN: 1367-2630. (2023) (Oct. 2017).

38. Farooqui, R. & Fenteany, G. Multiple Rows of Cells behind an Epithelial Wound Edge Extend Cryptic Lamellipodia to Collectively Drive Cell-Sheet Movement. *Journal of Cell Science* **118,** 51–63. ISSN: 0021-9533. (2024) (Jan. 2005).

39. Bieling, P. & Rottner, K. From WRC to Arp2/3: Collective Molecular Mechanisms of Branched Actin Network Assembly. *Current Opinion in Cell Biology* **80,** 102156. ISSN: 0955-0674. (2024) (Feb. 2023).

40. Rottner, K., Stradal, T. E. B. & Chen, B. WAVE Regulatory Complex. *Current Biology* **31,** R512–R517. ISSN: 0960-9822. (2024) (May 2021).

41. Ridley, A. J. & Hall, A. The Small GTP-binding Protein Rho Regulates the Assembly of Focal Adhesions and Actin Stress Fibers in Response to Growth Factors. *Cell* **70,** 389–99 (1992).

42. Stringer, C., Wang, T., Michaelos, M. & Pachitariu, M. Cellpose: A Generalist Algorithm for Cellular Segmentation. *Nature methods* **18,** 100–106. ISSN: 1548-7105 (Jan. 2021).

43. Weigert, M. & Schmidt, U. *Nuclei Instance Segmentation and Classification in Histopathology Images with Stardist* in *2022 IEEE International Symposium on Biomedical Imaging Challenges (ISBIC)* (Mar. 2022), 1–4. (2024).

4 Methods

4.1 Plasmids, antibodies and reagents

Doxycycline-inducible lentiviral vectors, pSLIK-neomycin (neo) or pSLIK-hygromicin (hygro) carrying HA-RAB5A or RAC1(T17N) sequences were obtained from Gateway Technology (Invitrogen), and prepared following the manufacturer's protocol. The plasmids pBABE-puromycin (puro)-mCHERRY-H2B and pBABE-puro-EGFP-H2B were provided by the IFOM Imaging Facility. The lentiviral expression construct pRRL-LifeAct-EGFP-puromycin (puro) was a gift from O. Pertz (University of Basel, Basel, Switzerland).

Mouse monoclonal antibodies raised against α-Tubulin and Vinculin were from Sigma-Aldrich (1:1000 for WB). Mouse monoclonal anti-HA-Tag (6E2) (1:1000 for WB, 1:100 for IF), anti-RAB5A (E6N8S) (1:1000 for WB) and anti-RAB5A (C8B1) (1:100 for IF) antibodies were from Cell Signaling. Mouse monoclonal anti-STING/TMEM173 antibody was from Invitrogen (1:1000 for WB). Mouse monoclonal anti-RAC-1 antibody was from BD (1:1000 for WB). Secondary antibodies conjugated to horseradish peroxidase were all used at a dilution of 1:5000 and were from Cell Signaling. Cy3-conjugated secondary antibodies were from Jackson ImmunoResearch. DAPI, Alexa Fluor 488-conjugated secondary antibodies and Alexa Fluor Plus 405 Phalloidin were from ThermoFisher Scientific.

Doxycycline hyclate and Carbenoxolone disodium salt were from Sigma Aldrich.

4.2 Cell cultures

MCF10DCIS.com cells were provided by J. F. Marshall (Barts Cancer Institute, Queen Mary University of London, UK) and maintained in DMEM/F12 (Biowest) supplemented with 5% horse serum (Life Technologies), 2mM L-Glutamine (EuroClone), $0.5\,\mathrm{mg/mL}$ Hydrocortisone (Sigma-Aldrich), $10\,\mu\mathrm{g/mL}$ Human insulin (Sigma-Aldrich) and $20\,\mathrm{ng/mL}$ EGF (Peprotech).

MCF10A cells were a gift from J. S. Brugge (Department of Cell Biology, Harvard Medical School, Boston, USA) and were maintained in DMEM/F12 (Biowest) supplemented with 5% horse serum (Life Technologies), 2 mM L-Glutamine (EuroClone), $0.5\,\mathrm{mg/mL}$ Hydrocortisone (Sigma-Aldrich), $10\,\mu\mathrm{g/mL}$ Human insulin (Sigma-Aldrich), $100\,\mathrm{ng/mL}$ cholera toxin (Sigma-Aldrich) and $20\,\mathrm{ng/mL}$ EGF (Peprotech).

HEK-293T (BBCF-Biological Bank and Cell factory, INT, Milan) and Phoenix-AMPHO cells (American Type Culture Collection, CRL-3213) were grown in DMEM (Lonza) supplemented with 10% FBS (Life Technologies) and 2 mM L-glutamine (EuroClone) and used as the packaging line for lentiviral and retroviral vectors, respectively. All cell lines were authenticated by STR profiling (StemElite ID System, Promega) and tested for mycoplasma using PCR and biochemical test (MycoAlert, Lonza). Cells were grown at $37\,^{\circ}$C in a humidified atmosphere with 5% CO_2.

MCF10DCIS.com and MCF10A cells were infected with pSLIK-neo-EV (empty vector, CTR), pSLIK-neo-HA-RAB5A or pSLIK-hygro-RAC1(T17N) lentiviruses and selected with the appropriate antibiotic to obtain stable inducible cell lines. Constitutive expression of EGFP-LifeAct, mCherry or EGFP-H2B was achieved by lentiviral and retroviral infection of MCF10DCIS.com and MCF10A cells with EGFP-LifeAct-puro or pBABE-puro-mCherry-H2B/pBABE-puro-EGFP-H2B vectors, respectively.

4.3 Lentiviral and retroviral infections

Lentiviruses were produced by transfecting HEK-293T cells with $6\,\mu$g of the vector of interest, $4.5\,\mu$g of psPAX2 and $2\,\mu$g of pMD2 packaging vectors using Lipofectamine2000 protocol (Invitrogen). Retroviruses were produced by transfecting Phoenix-AMPHO cells with $10\,\mu$g of the vector of interest using Calcium Phosphate protocol. The day after transfection, medium was removed, and $5.5\,$mL of fresh medium was added to each $10\,$mm plate. 48 and 72 hours after transfection, supernatants containing viral particles were collected and passed through a $0.45\,\mu$m filter. Supernatants were supplemented with $8\,\mu g/$mL Polybrene (Sigma) and cells were subjected to four cycles of infection. Infected cells were then selected using the appropriate antibiotic: neomycin for the pSLIK-neo vector ($150\,\mu g/$mL), hygromycin for the pSLIK-hygro vector ($100\,\mu g/$mL).

4.4 Quantitative RT-PCR

Total RNA was extracted using the RNeasy Mini kit and quantified by NanoDrop to assess both the concentration and quality of the samples. Reverse transcription was performed using the SuperScript VILO cDNA Synthesis kit. Gene expression was analysed by using the TaqMan Gene expression Assay (Applied Biosystems). $0.1\,$ng of cDNA was amplified, in triplicate, in a reaction volume of $25\,\mu$L with $10\,$pmol of each gene-specific primer and the SYBR Green PCR

MasterMix (Applied Biosystems). Real-time PCR was performed on the 14 ABI/Prism 7700 Sequence Detector System (PerkinElmer/Applied Biosystems) using a pre-PCR step of 10 min at $95\,^{\circ}$C, followed by 40 cycles of 15 s at $95\,^{\circ}$C and 60 s at $60\,^{\circ}$C. Specificity of the amplified products was confirmed by melting curve analysis (Dissociation Curve TM; Perkin Elmer/Applied Biosystems) and by 6% PAGE. Preparations with RNA template without reverse transcription were used as negative controls. Samples were amplified with primers for each gene and different housekeeping genes. The cycle threshold Ct values were normalized to the housekeeping gene curve. PCR experiments were performed in triplicate and standard deviations calculated and displayed as error bars.

List of qRT-PCR assays:

Table 1: List of qRT-PCR assays

Gene symbol	Supplier	Assay ID
18s	ThermoFisher	Hs99999901_s1
GAPDH	ThermoFisher	Hs99999905_m1
GUSB	ThermoFisher	Hs99999905_m1
RAB5A	ThermoFisher	Hs00702360_s1
IFI27	ThermoFisher	Hs01086373_g1
IFI44	ThermoFisher	Hs00197427_m1
IFI44L	ThermoFisher	Hs00915292_m1
IFI6	ThermoFisher	Hs00242571_m1
IFIT1	ThermoFisher	Hs03027069_s1
IFIT3	ThermoFisher	Hs01922752_s1
ISG15	ThermoFisher	Hs01921425_s1
OASL	ThermoFisher	Hs00984387_m1

4.5 Immunostaining

Cells were washed twice with 1X PBS, fixed in 4% paraformaldehyde for 10 min and permeabilized with 0.1% Triton X-100 and 10% FBS for 10 min. After a 1X PBS wash, primary antibodies were added for 2 h at room temperature or overnight at $4\,^{\circ}$C. Coverslips were washed in 1X PBS before secondary antibody incubation for 1 h at room temperature, protected from light. Alexa Fluor Plus 405 Phalloidin was added in the secondary antibody step, where applicable.

After removal of not specifically bound antibodies by 1X PBS washing, nuclei were stained with 0.5 ng/mL DAPI. Samples were post-fixed and mounted on glass slides in anti-fade mounting medium (glycerol). Antibodies were diluted in 1X PBS and 10% FBS.

4.6 Immunoblotting

Cells, washed twice with cold phosphate-buffered saline (PBS), were lysed in JS buffer supplemented with proteases and phosphatases inhibitors (50 mM HEPES pH 7.5, 50 mM NaCl, 1% glycerol, 1% Triton X-100, 1.5 mM $MgCl_2$, 5 mM EGTA, protease inhibitor cocktail (Roche Basel, Switzerland), 20 mM Na pyrophosphate pH 7.5, 50 mM NaF, 5 M $NaVO_4$ in HEPES pH 7.5 to inhibit phosphatases). Lysates were incubated on ice for 15 min and cleared by centrifugation at 13000 rpm for 30 min at $4\,^{\circ}$C. Protein concentration was quantified by the Bradford colorimetric protein assay. The same amount of protein lysates was loaded into polyacrylamide gel in 5X SDS sample buffer. Proteins were transferred onto Protran Nitrocellulose Transfer membranes (Whatman) in transfer buffer (20% methanol, 14 g/L glycine, 3 g/L Tris base) at 0.85 A for 1.5 h. Membranes were blocked for unspecific antibody binding using 5% skimmed milk in TBS-T (0.1% Tween) for 1 h. Blocked membranes were probed with the appropriated primary antibody in blocking solution for 1hr at room temperature or overnight at $4\,^{\circ}$C. After washing thrice in TBST, the membranes were incubated with HRP conjugated secondary antibodies for 1 h at room temperature and visualized with ECL western blotting detection reagents (GE Healthcare). Membranes were imaged using an iBright imaging system (Thermofisher).

4.7 Cell streaming assay

Cells were seeded in 6-well plates (1.5×10^6 cells per well) or in 12-well plates (0.6×10^6 cells per well) in complete medium and cultured until a uniform monolayer had formed. RAB5A expression was induced, where indicated, a few hours before performing the experiment by adding fresh complete media supplemented with 2.5 µg/mL doxycycline hyclate to cells. Cell migration was monitored by time-lapse phase contrast and fluorescence microscopy using a Leica Thunder Imaging System based on a Leica DMi8 inverted microscope equipped with a Leica K8 CMOS camera. A Leica HC PL FLUOTAR 10x/0.32 PH1 objective was used. Images were acquired every 5 min over a 24–48 h period. The assay was performed using an environmental microscope incubator set to $37\,^{\circ}$C and 5% CO_2 perfusion. After cell induction, doxycycline hyclate was maintained in the medium for the total duration of the time-lapse experiment.

4.8 Pipeline of analysis of cell motility

MCF10DCIS.com monolayers were seeded and time-lapse movies were acquired as described before. For each sample, typically five fields of view (FOVs) were simultaneously collected and analysed. Movies of mixed monolayers composed of control (CTRL) and RAB5A-overexpressing cells typically contain three different channels, displaying: phase contrast of the cell monolayer, fluorescent nuclei of the CTRL cell population and fluorescent nuclei of the RAB5A-overexpressing cell population.

The overall image analysis is divided in three main blocks:

1. PIV: preliminary analysis to identify the peak of maximum motility of 100% RAB5A population
2. "STATIX": nuclei segmentation and characterization of the cell pattern from the segmented cell nuclei
3. "DYNAMIX": single-cell tracking and quantification of the main dynamical parameters of interest from cell trajectories

4.8.1 PIV

Maps of the flow field in the cell monolayer are obtained by analyzing phase-contrast movies with PIV using a custom MATLAB script. The time interval between consecutive frames is typically 5 min. The image size is 1024 x 1024 pixels, while the interrogation window is typically set to 32 × 32 pixels, with a 50% overlap between adjacent windows. The size is chosen so that each interrogation window contains roughly 5 cell nuclei. Larger and smaller interrogation windows have also been tested as a consistency check, giving substantially equivalent results. PIV analysis gives the instantaneous velocity $\mathbf{v}_i$ in each interrogation window i. From this map of velocities, we compute the instantaneous velocity of the center of mass at a given time t as the average velocity $\boldsymbol{v}_{CM}(t) = \langle \boldsymbol{v}_i(t) \rangle_i$, where $\langle ... \rangle_i$ denotes the average over all the interrogation windows. Moreover, we quantify the root mean square velocity as $v_{RMS} = \sqrt{\langle |\boldsymbol{v}_i - \boldsymbol{v}_{CM}|^2 \rangle_i}$.

By looking at the time evolution of the two velocities v_{CM} and v_{RMS}, we identify the peak of maximum motility for the sample made of 100% RAB5A cells. We then select a time window centered around the motility peak and perform the rest of the analysis over the restricted time interval for each sample.

4.8.2 STATIX

We characterize the spatial distribution of the two cell populations within the monolayer. To do that, fluorescence time-lapse images within the selected time window are first cropped on a square central portion of edge equal to 800 pixels. Both channels displaying CTRL and RAB5A cell nuclei are then processed with ImageJ using StarDist [43–45], a deep-learning based Fiji plugin that allows detecting and segmenting densely-packed nuclei with star-convex polygons. This plugin offers a set of already trained models that can be directly applied to new images: in our case we select and used the built-in neural network model called "versatile (fluorescent nuclei)". For each frame, the segmented nuclei are returned as a label image. The output labelled images are then saved and further processed with custom MATLAB scripts.

Using the built-in MATLAB function *regionprops*, we compute the main features of all labeled cell nuclei, including their centroid positions. For each frame, we thus have a list of centroid coordinates of each cell nucleus, which we use to first calculate the Delaunay triangulation and then the corresponding Voronoi diagram. The Voronoi tessellation partitions the monolayer into regions containing a single vertex of the triangulation and all the surrounding points that are closer to that vertex than to any other vertex.

The connectivity list obtained from the triangulation allows identifying the first neighbors of each cell. Thus, we can find and characterize all clusters of both cell types. The size of each cluster is calculated as the total area covered by the Voronoi regions of the cells belonging to that cluster. A cluster of a given cell type is considered as percolating if it is simultaneously touching at least two opposite frame edges. For each population, we thus compute the surface fraction covered by the percolating cluster ϕ_{PC}. If we have no percolation then $\phi_{PC} = 0$. By averaging ϕ_{PC} over each frame in the time window and then over each field of view we obtain the percolation probability.

As for each cell we know the list of neighbors and their cell type, we can quantify the level of demixing in the monolayer. For each cell, we define and calculate the demixing parameter (DP) as $DP = (\frac{n_{self}}{n_{tot}} - \phi_{self})(1 - \phi_{self})^{-1}$, where n_{tot} is the total number of neighbors, n_{self} is the number of neighbors of the same kind as the cell we are considering, and ϕ_{self} is the fraction of cells of that same kind in the monolayer. If the two populations are well mixed, we expect $\frac{n_{self}}{n_{tot}} \simeq \phi_{self}$, thus $DP \simeq 0$. If there is a certain level of demixing, cells will be surrounded on average by more cells of the same kind compared to the expected value ϕ_{self} and thus $DP > 0$. In the

limit case, the cell is surrounded by all cells of the same family, so $n_{self} = n_{tot}$ and $DP = 1$. The demixing parameter is calculated for each cell for each frame. The mean value is calculated by first averaging over all the cells in the monolayer, or over all cells of the same population separately, and then over time within the selected time window.

4.8.3 DYNAMIX

For a more detailed characterization of cell dynamics, we perform single-cell tracking over the selected time window. To do that we use TrackMate [46, 47], a Fiji tracking plugin, on the labeled image sequences. This plugin allows following the nuclei over time and reconstruct their trajectories: each labeled nucleus is detected in multiple frames and assigned an identity, which is recorded over the frames in the shape of a track. These tracks are then saved for subsequent processing with a series of custom MATLAB scripts that extract the dynamical parameters of interest. For the analysis, only tracks lasting at least 5 consecutive frames are considered.

Velocities For a given nucleus, the track contains the corresponding spot features, including the position of the centroid $\boldsymbol{r}_i = (x_i, y_i)$, for each frame. The instantaneous velocity of the i-th nucleus at time t is computed as $\boldsymbol{v}_i(t) = (\boldsymbol{r}_i(t + \Delta t) - \boldsymbol{r}_i(t))/\Delta t$ where Δt is the time interval between two consecutive frames.

At each time point t, we then calculate the instantaneous velocity of the center of mass, defined as the ensemble average velocity $\boldsymbol{v}_{CM}(t) = \langle \boldsymbol{v}_i(t) \rangle_i$, where $\langle ... \rangle_i$ denotes the average over all the nuclei in the field of view detected at both times t and $t + dt$.

The amplitude of the velocity fluctuations is evaluated as the root mean square velocity of the nuclei in the reference frame of the center of mass, namely we compute $v_{RMS} = \sqrt{\langle |\boldsymbol{v}_i - \boldsymbol{v}_{CM}|^2 \rangle_i}$ where $\boldsymbol{v}_i$ are the velocities of the nuclei and $\boldsymbol{v}_{CM}$ is the velocity of the center of mass. Using these two quantities we also evaluate the order parameter as $\psi = \frac{|\langle \boldsymbol{v} \rangle|}{\sqrt{\langle |\boldsymbol{v}|^2 \rangle}}$.

All the aforementioned parameters are evaluated at each time point within the selected time window and then averaged first over time and then over the different FOVs. The average is calculated considering both populations separately but also for the whole cell monolayer.

Directional persistency We compute the mean square displacement $\text{MSD}(\Delta t) = \langle |\boldsymbol{r}_i(t + \Delta t) - \boldsymbol{r}_i(t)|^2 \rangle_i$ at different time delays Δt, spanning between the minimum time interval between

consecutive frames and half the duration of the selected time window. We fit the MSD curves with an equation of the kind $\text{MSD}(\Delta t) = 2D\Delta t + (2D/\gamma)(\exp(-\gamma\Delta t) - 1) + k$ [48], where D represents an effective diffusion coefficient and the constant k is introduced to account for the nuclei segmentation noise. This equation describes a shift from a short-time ballistic-like scaling MSD $\sim \Delta t^2$ to a long-time diffusive-like scaling MSD $\sim \Delta t$. The persistence length L_{pers} is retrieved from the fit parameters as $L_{pers} = \sqrt{D/\gamma}$.

Spatial velocity correlation We compute the velocity spatial correlation function as $c_{vv}(r) = \langle \boldsymbol{v}_i(t) \cdot \boldsymbol{v}_j(t) \rangle_{i \neq j}$, where $\cdot$ denotes the scalar product and $\langle ... \rangle_{i \neq j}$ indicates the average over all couples of nuclei in the field of view. The correlation is calculated at each time t and then averaged over the entire time window. We estimate the correlation length L_{corr} of the velocity field by fitting c_{vv} with a stretched exponential of the kind $e^{-(r/L_{corr})^\beta}$.

4.9 Co-culture experiment of monolayers with different mixing ratios

MCF10DCIS.com cells were seeded in removable PDMS cell culture chambers (Stencell Presto, idylle). These silicone stencils can stick on the bottom of plastic multi-wells and are made of two oblong chambers separated by a $0.25\,$mm spacer. In each of the two chambers 45000 cells were seeded at the indicated mixing fraction. After $24\,$h, the silicone spacer was removed by manual cutting with a scalpel and cells were left to close the gap for at least $24\,$h. RAB5A expression was induced a few hours before performing the experiment by adding fresh complete media supplemented with $2.5\,\mu$g/mL doxycycline hyclate to cells. Cell migration was monitored as described before.

The activity map shown in Supplementary Fig.3A represents the local relaxation rate Γ^* (1/hours) and it is obtained according to the procedure described in [33]. In brief, we spatially downsample by a factor of 32 the image sequence obtained by merging the two fluorescent channels. For each pixel $\boldsymbol{x}$ of the obtained image sequence $I(\boldsymbol{x}, t_0)$, we evaluate the mean squared difference $d(\tau \mid \boldsymbol{x}) = \langle I(\boldsymbol{x}, t_0 + \tau) - I(\boldsymbol{x}, t_0) \rangle_{t_0}$, where the symbol $\langle \rangle_{t_0}$ indicates a time average performed over the interval comprised between 6 and 16 hours from the beginning of the acquisition. $d(\tau \mid \boldsymbol{x})$ is an increasing function of τ and it saturates to a plateau value with a characteristic relaxation rate Γ^*, which is a measure of the rapidity of the local dynamics [33]. For each pixel $\boldsymbol{x}$, a stretched exponential function $f(\tau) = A(1 - e^{-(\Gamma^*\tau)^\beta}) + B$ is then fitted to $d(\tau \mid \boldsymbol{x})$ to obtain an estimate of the local relaxation rate Γ^*.

4.10 Analysis of cryptic lamellipodia dynamics

MCF10DCIS.com cells stably expressing eGFP-LifeAct (co-expressing EV or RAB5A) were mixed 1:10 with unlabeled cells and seeded at the indicated mixing fractions in Ibidi μ-Slide 8 Well chamber slides (150000 cells/well). Cell streaming assay was performed as described before. Cell migration was monitored by time-lapse phase contrast and fluorescence microscopy using a Leica Thunder Imaging System based on a Leica DMi8 inverted microscope equipped with a Leica K8 CMOS camera. A Leica HC PL APO 40×/0.95 dry objective was used. The images were acquired every 1.5 min for 4 hour focusing on the basal cellular region in order to correctly visualize cryptic lamellipodia and acquiring z-stacks spanning ~ 3 µm below and above the middle plane.

Maximum projections were used to measure cryptic lamellipodia directionality by identifying the angle θ delimited by the manually-annotated direction of the single lamellipodium and the direction vector of the local average velocity calculated by PIV, as previously described. The local velocity vector was obtained by averaging velocity vectors within a region roughly corresponding to the size of the cell of interest. $\theta = 0^\circ$ indicates that protrusion and collective migration have the same direction; $\theta = 180^\circ$ indicates that protrusion and collective migration have opposite directions.

4.11 Cell shape analysis

Confocal images of MCF10DCIS.com monolayers were acquired using a Leica TCS SP8 laser confocal scanner mounted on a Leica DMi8 microscope equipped with motorized stage; a Leica HC PL APO CS2 40×/1.30 oil immersion objective was used. For each field of view fluorescent nuclei and Phalloidin channels were acquired.

Images were processed using a custom Python script exploiting Cellpose [42] to segment cell (exploiting Phalloidin staining) and nuclear (exploiting the differential H2B-GFP or H2B-mCherry nuclear fluorescent markers in control and RAB5A cells) borders (Supplementary Fig.4A). The Cellpose Cytoplasm 3.0 model was used to detect cell borders, while the Nuclear model was used to detect nuclei. The mask of each cell was assigned to the corresponding nucleus exploiting the differential fluorescent labeling in case of mixed cell populations. The obtained masks were filtered discarding nuclei shared by more than 1 cell, extremely big or small nuclei and cells without a nucleus. User-defined area cut-off values for cells and nuclei were also used.

Morphological parameters were calculated using the Python Scikit-image library.

4.12 FACS sorting

MCF10DCIS.com CTRL EGFP-H2B and RAB5A mCherry-H2B cells were seeded at different relative proportions in 6-well plates (1.5×10^6 cells per well) in complete medium and cultured until a uniform monolayer had formed. RAB5A expression was induced for 48 hours. Cells were detached with trypsin and the two cell populations were separated using a MoFlo Astrios (Beckman Coulter) cell sorter set with a 488 nm laser and a 513/26 emission filter to detect eGFP and a 561 nm laser and a 614/20 emission filter to detect mCherry signal. Cells were immediately pelleted, washed with cold PBS and stored at $-80\,^{\circ}$C for subsequent RNA extraction.

4.13 RNA-sequencing

4.13.1 Samples preparation and sequencing

MCF10DCIS.com CTRL EGFP-H2B and RAB5A mCherry-H2B cells were seeded at different relative proportions in 6-well plates (1.5×10^6 cells per well) in complete medium and cultured until a uniform monolayer had formed. Three independent biological replicas were performed. RAB5A expression was induced for 48 hours. Cells were detached and FACS-sorted as already described. For each experimental sample, RNA was extracted using TRIzol reagent (Thermo Fisher) followed by RNAeasy Mini Kit (Qiagen), its abundance measured using Nanodrop and its integrity assessed using Agilent Bioanalyzer 2100 with Nano RNA kit (RIN > 8).

Sequencing was performed by Eurofins Genomics sequencing company (Germany) in paired-end mode (2 x 150 bn) on an Illumina Sequencer NovaSeq X, generating on average 30 million PE reads per sample.

4.13.2 Bioinformatic analysis

FASTQ reads were quality checked with FastQC (v 0.11.9) and adaptors trimmed with Trimmomatic (v 0.40) [49], specifying default parameters. High-quality trimmed reads were mapped to the mm10 reference genome with STAR aligner (v 2.7.9) using the latest GENCODE main annotation file. The construction of the gene count matrix was done using featureCounts [50] on .bam files generated by STAR, counting the reads associated to 'exons' features per gene. This step was performed using nf-core rnaseq pipeline (v 3.13.2) [51]. Differential gene expression

on the normalized gene count matrix was performed with DESeq2 (v 3.13). DEGS (differentially expressed genes) were extracted by filtering on Pvalue adjusted (using 0.05 as threshold value), corrected by the Benjamini Hochberg test. GO enrichment analysis on DEGs was performed with Gprofiler2 (v 0.2.0) [52]; only overrepresented categories with corrected Pvalue were kept, using the previously described method. Downstream statistics and plotting were performed within the R (v 4.0.1) environment. Heatmaps were generated with ComplexHeatmap (v 3.0.215). Preranked gene set enrichment analysis (GSEA) for evaluating pathway enrichment in transcriptional data was carried out using the Bioconductor package fgsea [53], taking advantage of the Hallmarks, KEGG and chemical and genetic perturbations (CGP) gene sets available from the GSEA Molecular Signatures Database (http://www.gsea-msigdb.org/gsea/msigdb/collections.jsp).

4.14 Conditioned medium treatments

MCF10DCIS.com cells were seeded in 6-well plates (1.5×10^6 cells per well) in complete medium and cultured until a uniform monolayer had formed. RAB5A expression was induced and conditioned medium was collected after 24 and 48 hours. Conditioned media were centrifugated $250 \times g$ for 5 min to eliminate dead cells and filtered with 0.22 µm filters. Recipient cells were treated for 48 hours. Where indicated, conditioned medium was boiled at $100\,^{\circ}$C for 30 min to eliminate proteins fraction. For conditioned medium fractionation, 3 kDa molecular weight cut-off concentrating columns were used and recipient cells were either treated with upper or lower molecular weight fraction.

4.15 Proteomic mass-spectrometry analysis of the secretome

4.15.1 Stable isotope labelling by amino acids in cell culture (SILAC)

Analysis of the secretome of MCF10DCIS.come cells was performed as previously described by Secret3D workflow [54]. Briefly, MCF10DCIS.com CTRL or RAB5A-overexpressing cells were grown for one week in DMEMF12 SILAC supplemented with 5% dialysed FBS, 0.5 mg/mL hydrocortisone, 10 µg/mL human insulin, 20 ng/mL EGF and L-arginine and L-lysine containing "medium" or "heavy" stable isotopes (the medium and heavy media) (Cambridge Isotope Laboratories). The "medium" culture contained $^{13}C_6$-$^{14}N_4$ L-arginine and 4,4,5,5-D_4 L-lysine, and the "heavy" culture contained $^{13}C_6$-$^{15}N_4$ L-arginine and $^{13}C_6$-$^{15}N_2$ L-lysine amino acids. After five cell divisions, incorporation of labeled amino acids was tested. The incorporation test was

performed by nLC-ESI-MS/MS on a Orbitrap mass spectrometer and the incorporation rate was greater than 95% for both Lys and Arg [55]. Cells were then counted and equal amounts of control or RAB5A-overexpressing MCF10DCIS.com cells (3×10^6) were plated into 60 mm dishes to obtain confluent monolayers. After two days, RAB5A expression was induced by adding fresh SILAC media supplemented with 2.5 µg/mL doxycycline hyclate to cells. After 24 hours, cells were washed 3x with PBS and 3x with serum-free medium. Cells were starved in serum-free SILAC media supplemented with 2.5 µg/mL doxycycline hyclate for 18 hours. Conditioned media were collected and centrifuged at $250 \times g$ for 5 min to eliminate dead cells and filtered with 0.22 µm filters. Heavy- and medium-labeled secretomes were mixed 1:1 and concentrated through a 3 kDa molecular weight cut-off concentrating column. Buffer was exchanged with 8 M Urea 100 mM Tris pH8, the protein extract was sonicated with BIORUPTOR (3 cycles: 30 s on/30 s off) and protein concentration was quantified by using Pierce BCA Protein Assay Kit (ThermoFisher Scientific).

4.15.2 Protein digestion and peptides purification

50 µg of proteins for each sample were processed applying the in-solution digestion FASP protocol [56]. Briefly, in an AMICON Ultra 0.5 mL 10K filter, proteins were reduced by Tris(2-carboxyethyl)phosphine TCEP (Thermo Scientific) and alkylated by chloroacetamide CAM (Sigma-Aldrich) at 10 mM and 40 mM respectively as final concentration, then deglycosylated by PNGase-F (New England Biolabs) and then overnight digested by Lys-C (Wako, FUJIFILM) and Trypsin (ROCHE) [54]. The resulting peptides were desalted on a home-made StageTip C18 [57], eluted peptides were dried, resuspended in 5% formic acid and injected on the LC-MS.

4.15.3 Mass Spectrometry data acquisition

Each digested sample was analyzed as technical replicate on the chromatographic system EASY-nLC1200 coupled with a Quadrupole Orbitrap Exploris 480 mass spectrometer equipped with a Nano Flex ESI-source and the FAIMS Pro interface operating at CV -50/-70 (ThermoFisher Scientific). Peptides were separated on a 25 cm, 75 µm ID, nano-column packed in house with ReproSil-Pur C18-AQ 1.9 µm beads (Dr. Maisch), at a flow rate of 200 nL/min, on a linear gradient of 80 min, starting from 2 min at 93% of solvent A (0.1% formic acid, 2% acetonitrile) and ramping to 30% solvent B (0.1% formic acid, 80% acetonitrile) in 60 min,

then to 60% of Solvent B in 5 min. This was followed by a washout step of 2 min increase to 100% of B which was held for 11 min. The ion source parameters were: Spray Voltage 2200 V, funnel RF lens at 40%, Ion Transfer Tube Temp $300\,^{\circ}$C and total carrier gas flow $3.7\,\mathrm{L/min}$. MS data were acquired in positive data-dependent acquisition mode (DDA) top 28 method for HCD fragmentation. Survey full scan MS spectra (300–1500 Th) were acquired in the Orbitrap with 60,000 resolution, Normalized AGC Target 100%, IT 100 ms, Microscan 1. Precursors for data-dependent scan should have 2-6 as charge state and a minimum precursor signal intensity threshold of 5.0e3. For HCD fragment spectra the resolution was set to 15,000, Normalized AGC Target 100%, maximum IT mode Auto, Microscan 1, Normalized Collision Energy 28%, Isolation Window 1.6 m/z with Exclusion duration of $20\,\mathrm{second}$ and Mass Tolerance of $\pm$ 10 ppm.

4.15.4 Mass Spectrometry data analysis

For identification and quantitation, .raw files were processed with MaxQuant (v. 2.0.3.0) searching against the database uniprot_cp_human_2020, setting as SILAC labels Arg10 with Lys8 and Arg6 with Lys4, trypsin specificity and up to two missed cleavages. Cysteine carbamidomethyl was used as fixed modification, methionine oxidation and protein N-terminal acetylation as variable modifications. Mass deviation for MS1 and MS2 peaks were set at 10 ppm and 20 ppm, respectively. The peptides and protein FDR were set to 0.01; the minimal length required for a peptide identification was seven amino acids; a minimum of two peptides and at least one unique peptide were required for high-confidence protein identification.

Subsequent data processing and statistical analysis was performed with Perseus (v. 1.6.2.3) [58] using SILAC ratios H/M Normalized and log2 transformed of Control/RAB5A conditions.

Differential proteins were calculated applying Significance B feature and p-value 0,05; upregulated and downregulated proteins are represented in the scatter plot. GO enrichment analysis on deregulated proteins and genes was performed with Gprofiler2 (v 0.2.0) [52]; only overrepresented categories with corrected Pvalue were kept. Downstream statistics and plotting were performed within the R (v 4.0.1) environment.

4.16 Human tissues

Human breast cancer tissue samples were collected according to the Helsinki Declaration and the study was approved by the University of Palermo Ethical Review Board (approval number

09/2018). The cases were classified according to the World Health Organization classification criteria of the tumors of the breast. All the tissue samples were from 15 adult female patients with breast ductal adenocarcinoma with an age range between 40 and 88 years old (histotypes in situ ductal adenocarcinoma, invasive ductal adenocarcinoma or both).

4.16.1 Immunohistochemistry and immunofluorescence on DCIS and IDC

$4\,\mu$m-thick human tissue sections were deparaffinized, rehydrated and unmasked using Novocastra Epitope Retrieval Solutions pH6 in thermostatic bath at $98\,^{\circ}$C for $30\,$min. Subsequently, the sections were brought to room temperature and washed in PBS. After neutralization of the endogenous peroxidase with 3% H2O2 and Fc blocking by a specific protein block (Leica Novocastra), the samples were incubated with the following primary antibodies: RAB5A (clone EPR5438, 1:100 pH6, ab109534, Abcam) and E-Cadherin (NCL-E-Cad, clone 36B5, 1:25 pH 6, Novocastra).

Immunohistochemistry (IHC) staining was developed using the Novolink Polymer Detection Systems (Leica Biosystems) and Vulcan Fast Red as substrate chromogen. Slides were counterstained using Harris hematoxylin (Novocastra, Leica Microsystems).

Immunofluorescence detection was performed using anti-mouse and anti-rabbit Alexa Fluor 488- and 568-conjugated secondary antibodies. To visualize cell nuclei, human slides were counterstained with DAPI (4',6-diamidin-2-fenilindolo).

All slides were analysed under a Zeiss Axioscope A1 microscope equipped with four fluorescence channels widefield IF. Microphotographs were collected using a Zeiss Axiocam 503 Color digital camera with the Zen 2.0 Software (Zeiss).

4.16.2 Quantification of geometric features in human DCIS and IDC samples

Nuclear segmentation Nuclear segmentation is performed with StarDist [44], using the Versatile (fluorescent nuclei) pretrained model. The result of the segmentation is a 16-bit map where a unique numerical value is assigned to each region of interest (ROI), corresponding to a single nucleus. The so-obtained map, the original image and a binary image (identifying the selected region (SR) corresponding to the lesion, manually segmented by an expert pathologist) are then loaded using a custom MATLAB script to extract nuclear features and generate the corresponding Voronoi diagram.

Determination of nuclear features For each image, only the nuclei included in the SR are considered. The number of selected nuclei per image varies between 500 and 2500. For each nucleus included in the SR, the position $\boldsymbol{x}_{cm} = (x_{cm}, y_{cm})$ of the center of mass (or centroid) is calculated as the brightness-weighted average of the coordinates included in corresponding ROI

$$\boldsymbol{x}_{cm} = \frac{\sum_{\boldsymbol{x} \in ROI} \boldsymbol{x} I(\boldsymbol{x})}{\sum_{\boldsymbol{x} \in ROI} I(\boldsymbol{x})}$$

where $I(\boldsymbol{x})$ is the intensity of the original image in the DAPI channel.

For each nucleus in the SR, the 2x2 matrix of the corresponding tensor of inertia I is considered

$$I = \begin{bmatrix} \sum_{x \in ROI} (x - x_{cm})^2 I(\boldsymbol{x}) & \sum_{x \in ROI} (x - x_{cm})(y - y_{cm}) I(\boldsymbol{x}) \\ \sum_{x \in ROI} (x - x_{cm})(y - y_{cm}) I(\boldsymbol{x}) & \sum_{x \in ROI} (y - y_{cm})^2 I(\boldsymbol{x}) \end{bmatrix}$$

The aspect ratio AR is then calculated as the square root of the ratio of the two eigenvalues I_1 and I_2 of I $AR = \sqrt{\frac{I_1}{I_2}}$

Voronoi diagram Based on the nuclear centroid positions, the Voronoi diagram (VD) is computed [59] using the *voronoin* MATLAB function. Given a set of points distributed on the plane (*generators*), the VD is a univocally defined tessellation of the plane in Voronoi cells. Each Voronoi cell is associated with a given generator and contains all the points that are closer to that generator than any other.

By construction, a faithful reconstruction is difficult to obtain for cell that are close the boundary of the SR, since in this condition a generator is not surrounded by other generators. To avoid the artifacts related to this known issue, we reject all Voronoi cells that are not fully contained within the SR.

The aspect ratio AR of each Voronoi cell is evaluated using the same procedure described above for the nuclei, where the matrix I is now calculated as

$$I = \begin{bmatrix} \int dA (x - x_{cm})^2 & \int dA (x - x_{cm})(y - y_{cm}) \\ \int dA (x - x_{cm})(y - y_{cm}) & \int dA (y - y_{cm})^2 \end{bmatrix}$$

where the integrals are calculated over the area of the Voronoi cell.

4.17 Agent-based model

We consider a minimal two-dimensional model of mutually repulsive self-propelled particles (or cells) with an active orientation mechanism that promotes the alignment of the self-propulsion velocity with their instantaneous velocity [60, 61].

The system is composed by N disk-like particles, each of them with radius a_i, arranged over a square of size L^2 with periodic boundary conditions. The surface density is captured by the packing fraction $\phi_s = \pi \sum_i a_i^2 / L^2$. We note that, since particles can overlap each other, ϕ_s can be also larger than 1. The state of each particle i is identified by its position $\boldsymbol{x}_i$ and a polar angle θ_i along which the direction of its self-propulsion velocity is aligned. The dynamics is defined by the following coupled Langevin equations:

$$\dot{\boldsymbol{x}}_i(t) = v_0 \boldsymbol{n}_i(t) + \sum_j \boldsymbol{F}_{ij}(t) \tag{5}$$

$$\dot{\theta}_i(t) = \Gamma_{0,1}[\psi_i(t) - \theta_i(t)] + \eta_i(t) \tag{6}$$

In Eq. 5, $v_{0,i}$ is a constant corresponding to the self-propulsion speed of particle i, $\boldsymbol{n}_i$ is a unit vector indicating the direction of the self-propulsion velocity, the sum $\sum_j$ is extended over all distinct particles j whose distance d_{ij} from particle i is less than the sum $A_{ij} = (a_i + a_j)$ of the respective radii, and $\boldsymbol{F}_{ij} = k(A_{ij} - d_{ij})(\boldsymbol{x}_i - \boldsymbol{x}_j)/|\boldsymbol{x}_i - \boldsymbol{x}_j|$ is an elastic repulsive force. This equation governs the motion of the center of mass of the particle, whose instantaneous velocity is thus given by the sum of a contribution due to self-propulsion and one associated with soft repulsive interactions with the neighboring particles.

In Eq. 6, $\Gamma_{0,i}$ is a constant corresponding to the self-propulsion orientation rate, ψ_i is the polar angle associated with the instantaneous orientation of the particle velocity $\dot{\boldsymbol{x}}_i$, and η_i is a delta-correlated Gaussian noise with zero mean and variance $\langle \eta_i^2 \rangle = 2D_{r,i}$. The equation describes the rotational dynamics of the self-propulsion velocity and incorporates the tendency of each particle to orient its self-propulsion velocity along the direction of the actual velocity (with an efficiency proportional to $\Gamma_{0,i}$), in presence of a random torque (whose amplitude is proportional to $D_{r,i}$) which tend to promote a random orientation of the self-propulsion velocity.

It is well-known that the model described by equations 5 and 6 experiences a flocking transition if the noise is low enough (i.e., if the orientation rate Γ_0 is large compared to the noise amplitude

D_r) or if the density is increased at fixed noise [60].

4.17.1 Mixed populations

The above-described model can be easily adapted to describe heterogeneous cell populations by introducing different families of particles, each one of them characterized by a distinct set of parameters $[v_{0,i}, \Gamma_i, D_{r,i}]$. For example, a binary mixture obtained by adding to a homogeneous population of motile cells a fraction $(1-\phi)$ of non-motile cells be simulated by letting $v_{0,i} = 0$ for $\phi N \leq i \leq N$, while $v_{0,i} = v_0$, $\Gamma_{0,i} = \Gamma_0$, and $D_{r,i} = D_r$ for $i < \phi N$.

4.17.2 Mixed populations: aligners and dissenters

A case of special interest for the present work is the one considered in [37], where, within a homogeneous population of "aligner" (motile and efficiently aligning) cells, a fraction $(1-\phi)$ of "dissenters" is introduced. In this case, dissenters have similar mobility parameters compared to "normal" aligning cells (the self-propulsion speed and the amplitude of the rotational noise are the same for both families), but they lack the ability to sense the direction of their velocity and/or to align their self-propulsion speed accordingly (for dissenters: $\Gamma_{0,i} = 0$).

4.17.3 Phenotypic switch

According to the minimal model introduced above, single-cell behavior is fully controlled by a set of three parameters $[v_{0,i}, \Gamma_i, D_{r,i}]$, encoding for self-propulsion speed, reorientation efficiency, and amplitude of the rotational noise, respectively. While in most implementations these parameters as considered as constants, it is possible to introduce different dynamical rules or mechanisms driving a change in single-cell identity, in response to external stimuli or variations in the local environment.

For example, in an aligners-dissenters scenario, it is possible to introduce an explicit dependency of the value of Γ_i of each cell on the composition of the set of particles surrounding it. In this work, we consider a simple non-symmetric "majority rule", where a dissenter switches to an aligning behavior (it assumes a non-zero value for Γ_i, identical to the one of aligners) whenever the majority of its first neighbors is represented by aligners. This transition is assumed to be reversible.

4.17.4 Numerical implementation and choice of the parameters

The results presented in this work are obtained from numerical simulations performed in MATLAB, by integrating with a Euler-Maruyama method equations 1 and 2. The integration step is set to $\Delta t = 0.05$. Unless otherwise specified, we consider systems of N=2000 cells at packing fraction $\phi_s = 1$, corresponding to full confluency. To prevent crystallization, a certain degree of dispersity is introduced in the cell radii. At the beginning of each simulation, the radius a_i of each particle is randomly extracted from a uniform distribution over the interval $[1-p, 1+p]$, where $p = 0.5$ is a polydispersity parameter. The self-propulsion speed is set to $v_0 = 0.25$, the amplitude of rotational noise to $D_r = 0.25$, and the orientation rate to $\Gamma_0 = 1$ and $\Gamma_0 = 0$ for aligners and dissenters, respectively. The force constant is fixed to $k = 10$. This is a relatively large value, corresponding to relatively stiff cells [37]. In the initial configuration, cells are randomly distributed over the simulation box, with randomly oriented self-propulsion velocities. Unless otherwise specified, the duration of a single simulation run corresponds to 10^5 time units. For each combination of parameters, at least 5 independent simulations are performed.

The results presented in this work are obtained considering mixed populations composed of aligners and dissenters at different fractions, both in the absence and in the presence of a phenotypic switch mechanism acting on the dissenters, based on previously introduced "majority rule".

4.18 Statistical analysis

Statistical analysis and plots were performed using Prism 10 (GraphPad) and *Matplotlib* library in Python. Student's unpaired t-test was used when comparing two Gaussian distributions, while Mann-Whitney test was used when comparing two non-Gaussian distributions. In the case of comparing multiple treatments, one-way ANOVA followed by the appropriate multiple comparison test was used.

Methods References

33. Cerbino, R. *et al*. Disentangling Collective Motion and Local Rearrangements in 2D and 3D Cell Assemblies. *Soft Matter* **17,** 3550–3559. ISSN: 1744-6848. (2024) (Apr. 2021).

37. Yllanes, D., Leoni, M. & Marchetti, M. C. How Many Dissenters Does It Take to Disorder a Flock? *New Journal of Physics* **19,** 103026. ISSN: 1367-2630. (2023) (Oct. 2017).

42. Stringer, C., Wang, T., Michaelos, M. & Pachitariu, M. Cellpose: A Generalist Algorithm for Cellular Segmentation. *Nature methods* **18,** 100–106. ISSN: 1548-7105 (Jan. 2021).

43. Weigert, M. & Schmidt, U. *Nuclei Instance Segmentation and Classification in Histopathology Images with Stardist* in *2022 IEEE International Symposium on Biomedical Imaging Challenges (ISBIC)* (Mar. 2022), 1–4. (2024).

44. Schmidt, U., Weigert, M., Broaddus, C. & Myers, G. *Cell Detection with Star-Convex Polygons* in *Medical Image Computing and Computer Assisted Intervention – MICCAI 2018* (eds Frangi, A. F., Schnabel, J. A., Davatzikos, C., Alberola-López, C. & Fichtinger, G.) (Springer International Publishing, Cham, 2018), 265–273. ISBN: 978-3-030-00934-2.

45. Weigert, M., Schmidt, U., Haase, R., Sugawara, K. & Myers, G. *Star-Convex Polyhedra for 3D Object Detection and Segmentation in Microscopy* in *2020 IEEE Winter Conference on Applications of Computer Vision (WACV)* (Mar. 2020), 3655–3662. (2024).

46. Ershov, D. *et al*. TrackMate 7: Integrating State-of-the-Art Segmentation Algorithms into Tracking Pipelines. *Nature Methods* **19,** 829–832. ISSN: 1548-7105. (2024) (July 2022).

47. Tinevez, J.-Y. *et al*. TrackMate: An Open and Extensible Platform for Single-Particle Tracking. *Methods. Image Processing for Biologists* **115,** 80–90. ISSN: 1046-2023. (2024) (Feb. 2017).

48. Bechinger, C. *et al*. Active Particles in Complex and Crowded Environments. *Reviews of Modern Physics* **88,** 045006. (2024) (Nov. 2016).

49. Rossi, G. *et al*. MCT1-dependent Energetic Failure and Neuroinflammation Underlie Optic Nerve Degeneration in Wolfram Syndrome Mice. *eLife* **12,** e81779. ISSN: 2050-084X (Jan. 2023).

50. Liao, Y., Smyth, G. K. & Shi, W. featureCounts: An Efficient General Purpose Program for Assigning Sequence Reads to Genomic Features. *Bioinformatics (Oxford, England)* **30,** 923–930. ISSN: 1367-4811 (Apr. 2014).

51. Ewels, P. A. *et al*. The Nf-Core Framework for Community-Curated Bioinformatics Pipelines. *Nature Biotechnology* **38,** 276–278. ISSN: 1546-1696. (2024) (Mar. 2020).

52. Love, M. I., Huber, W. & Anders, S. Moderated Estimation of Fold Change and Dispersion for RNA-seq Data with DESeq2. *Genome Biology* **15,** 550. ISSN: 1474-760X. (2024) (Dec. 2014).

53. Korotkevich, G. *et al*. *Fast Gene Set Enrichment Analysis* Feb. 2021. (2024).

54. Matafora, V. & Bachi, A. Secret3D Workflow for Secretome Analysis. *STAR Protocols* **1,** 100162. ISSN: 2666-1667 (2020).

55. Pateetin, P. *et al*. Triple SILAC Identified Progestin-Independent and Dependent PRA and PRB Interacting Partners in Breast Cancer. *Scientific Data* **8,** 100. ISSN: 2052-4463. (2024) (Apr. 2021).

56. Wiśniewski, J. R. in *Microbial Proteomics: Methods and Protocols* (ed Becher, D.) 3–10 (Springer, New York, NY, 2018). ISBN: 978-1-4939-8695-8. (2024).

57. Rappsilber, J., Mann, M. & Ishihama, Y. Protocol for Micro-Purification, Enrichment, Pre-Fractionation and Storage of Peptides for Proteomics Using StageTips. *Nature Protocols* **2,** 1896–1906. ISSN: 1750-2799. (2024) (Aug. 2007).

58. Tyanova, S. *et al*. The Perseus Computational Platform for Comprehensive Analysis of (Prote)Omics Data. *Nature Methods* **13,** 731–740. ISSN: 1548-7105. (2024) (Sept. 2016).

59. Okabe, A., Boots, B., Sugihara, K. & Chiu, S. N. *Spatial Tessellations: Concepts and Applications of Voronoi Diagrams* ISBN: 978-0-470-31785-3 (John Wiley & Sons, Sept. 2009).

60. Szabó, B. *et al*. Phase Transition in the Collective Migration of Tissue Cells: Experiment and Model. *Physical Review E* **74,** 061908. (2024) (Dec. 2006).

61. Fily, Y. & Marchetti, M. C. Athermal Phase Separation of Self-Propelled Particles with No Alignment. *Physical Review Letters* **108,** 235702. (2024) (June 2012).

Acknowledgments

We thank S. Barozzi, Z. Lavagnino and F. Casagrande of the Advanced Light Microscopy Facility at IFOM for technical assistance in advanced imaging acquisition; M. G. Totaro and S. Martone of the Flow Cytometry Facility at IFOM for technical assistance; the Cellular and Preclinical Models Facility at IFOM for technical assistance; V. Dall'Olio and L. Tizzoni at Cogentech for qRT-PCR services. The work is supported by ERC-Synergy (Grant# 801 101071470), AIRC-IG (Grant#22821), AIRC 5x1000 (#22759), the Italian Ministry of University and Research (PRIN202223GSCIT_01/G53D23002570006/20229RM8A_001;COMBINE/G53D23007040001/P2022RH4HH002;PNRR_CN3RNA_SPOKE/G43C22001320007) to G.S.; AIRC MFAG-22083 to F.G.; AIRC-MFAG 2022 (Grant# 27616) to B.G.; AIRC doctoral fellowship to L.B; AIRC IG 2023-28822 to S.P.; AIRC IG 27098 to A.B.; AIRC IG2023-28978 to C.T.; ERC-Synergy (Grant# 801 101071470) to R.V. and J.A..

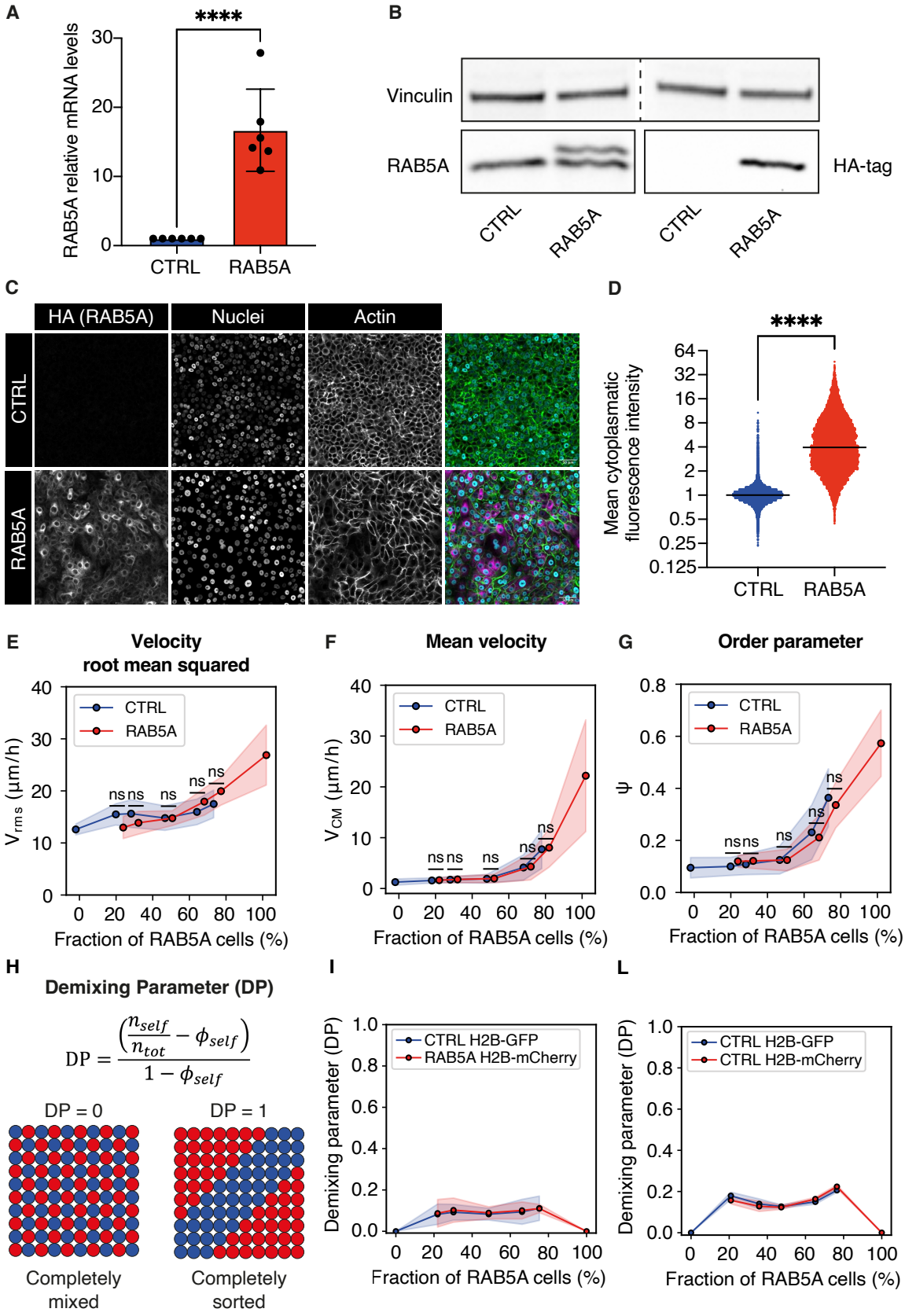
Author contributions

G.S. and F.G. conceived the study. L.B., C.M., J.A., E.F., B.G., A.P., A.C. and V.C. performed the experiments. L.B., C.G., S.V., E.B., F.G. performed the data and image analysis. L.B. compiled the figures. C.T. and V.C. collected and organized the clinical samples. A.B., C.T., S.P., R.C., R.V., G.S. and F.G. supervised the experiments and data analysis. L.B., G.S., F.G., C.G., J.A. and R.V. wrote, reviewed and edited the manuscript.

Supplementary Information

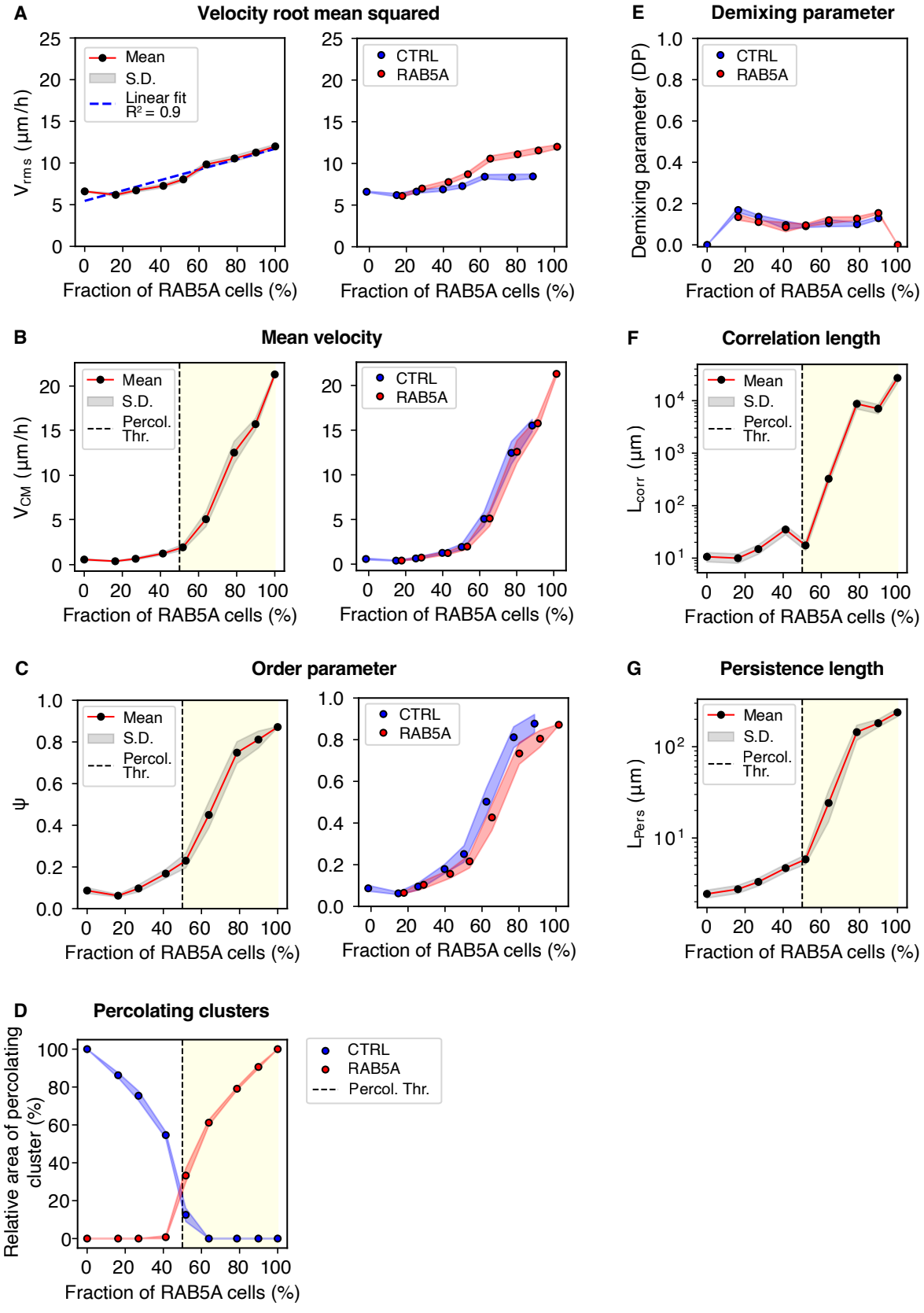
- Supplementary Figures
- Supplementary Movies Legends
- Supplementary Material – Hydrodynamic model

Supplementary Figures


A
****
RAB5A relative mRNA levels
30
20
10
0
CTRL
RAB5A
B
Vinculin
RAB5A
HA-tag
CTRL
RAB5A
CTRL
RAB5A
C
HA (RAB5A)
Nuclei
Actin
CTRL
RAB5A
D
****
Mean cytoplasmatic fluorescence intensity
64
32
16
8
4
2
1
0.5
0.25
0.125
CTRL
RAB5A
E
Velocity root mean squared
CTRL
RAB5A
V_{rms} (µm/h)
ns ns ns ns ns
Fraction of RAB5A cells (%)
F
Mean velocity
CTRL
RAB5A
V_{CM} (µm/h)
ns ns ns ns ns
Fraction of RAB5A cells (%)
G
Order parameter
CTRL
RAB5A
Ψ
ns ns ns ns ns
Fraction of RAB5A cells (%)
H
Demixing Parameter (DP)
$\mathrm{DP} = \frac{\left(\frac{n_{self}}{n_{tot}} - \phi_{self}\right)}{1 - \phi_{self}}$
DP = 0
DP = 1
Completely mixed
Completely sorted
I
CTRL H2B-GFP
RAB5A H2B-mCherry
Demixing parameter (DP)
Fraction of RAB5A cells (%)
L
CTRL H2B-GFP
CTRL H2B-mCherry
Demixing parameter (DP)
Fraction of RAB5A cells (%)

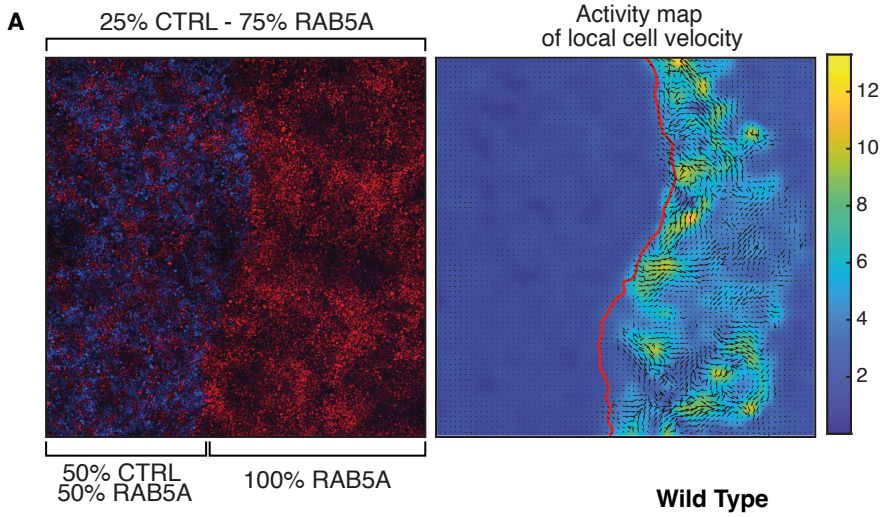
Supplementary figure 1.

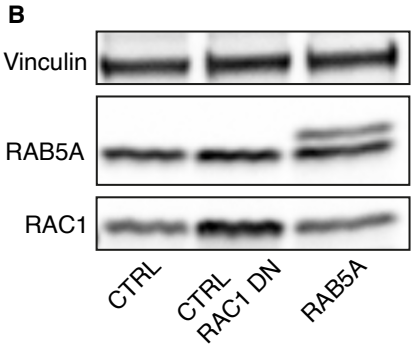
MCF10DCIS.com cells were engineered to express doxycycline-inducible RAB5A, and cells transduced with an Empty Vector (CTRL) were used as control. The expression level of RAB5A was analysed by both qRT-PCR and Western Blot after 24 hours of 2.5 µg/ml doxycycline treatment. (A) qRT-PCR, mRNA levels are the mean $\pm$ Standard Deviation (S.D.) relative to control after normalizing to GAPDH. n=6. Two-tailed unpaired t-test (****: p$<$0.0001). (B) Immunoblot with the indicated antibodies of total lysates of doxycycline-treated CTRL and RAB5A monolayers. Vinculin was used as loading control. (C) MCF10DCIS.com CTRL or RAB5A-overexpressing cells were seeded as confluent monolayers and treated with 2.5 µg/ml doxycycline for 24 hours. They were fixed in 4% paraformaldehyde and stained with anti-HA antibody, DAPI, or Phalloidin to visualize HA-RAB5A protein, nuclei, and actin cytoskeleton, respectively. The analysis was performed by confocal microscopy. Representative images are shown. Scale bar, 50 µm. Data in (D) are the mean cytoplasmic fluorescent intensities of HA-RAB5A signal in RAB5A-overexpressing cells normalized on CTRL cells. Fluorescent intensities were calculated for each cell by segmenting them with Cellpose [43–45] exploiting Phalloidin staining. n = more than 20000 cells from 3 independent experiments. Black line is the median. Mann-Whitney test (****: p<0.0001). (E-G) Motility parameters as in Fig. 1 distinguishing between control (blue) and RAB5A-overexpressing (red) cells. (E) Root mean square velocity (V_{rms}) in the center of mass reference frame, (F) mean velocity of the center of mass (V_{cm}), (G) polar order parameter ψ. Tukey's multiple comparison test (from left to right, ns: A: p=0.9387, p=0.9940, p>0.9999, p=0.9866, p=0.9466; B: p>0.9999; C: p>0.9999). Data are the mean $\pm$ S.D (n= 15 fields of view from 3 independent experiments). (H) Schematics of demixing parameter calculation. DP is evaluated over a ~ 10 hours time window centered on the peak of motility of RAB5A cells and calculated as $(\frac{n_{self}}{n_{tot}} - \phi_{self})(1-\phi_{self})^{-1}$, where n_{self} is the number of cells belonging to a population (GFP-H2B or mCherry-H2B), n_{tot} is the total number of cells and ϕ is the surface fraction covered by the percolating cluster. (I) Demixing parameter of EGFP-H2B control and mCherry-H2B RAB5A cells plotted as a function of the relative amount of mCherry-H2B MCF10DCIS.com cells in mixed monolayers monitored by time-lapse microscopy. Data are the mean $\pm$ S.D (n= 15 fields of view from 3 independent experiments). (L) Demixing parameter of EGFP-H2B and mCherry-H2B control cells plotted as a function of the relative amount of mCherry-H2B MCF10DCIS.com cells in mixed monolayers monitored by time-lapse microscopy. Data are the mean $\pm$ S.D (n= 15 fields of view from 3 independent experiments).

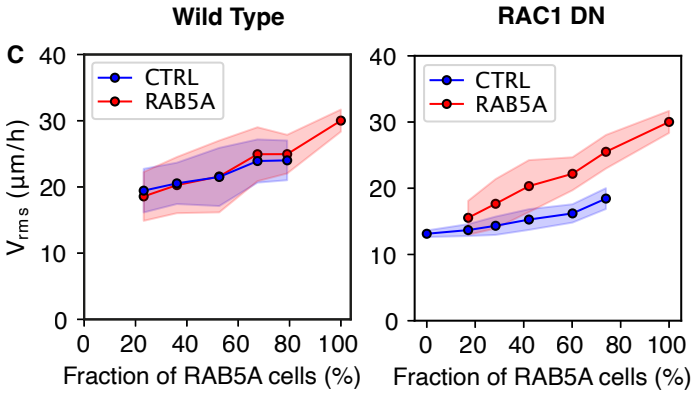

A
Velocity root mean squared
Mean
S.D.
Linear fit
R² = 0.9
CTRL
RAB5A
Fraction of RAB5A cells (%)
B
Mean velocity
Percol. Thr.
C
Order parameter
D
Percolating clusters
Relative area of percolating cluster (%)
Percol. Thr.
E
Demixing parameter
Demixing parameter (DP)
F
Correlation length
G
Persistence length

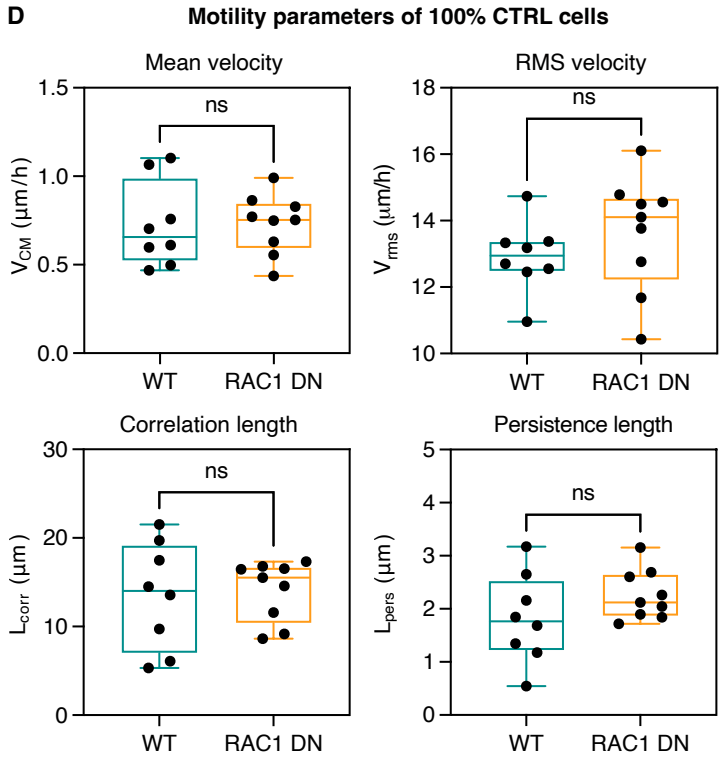
Supplementary figure 2.

Motility parameters plotted as a function of the relative amount of RAB5A-MCF10A cells obtained by nuclear tracking of mixed monolayers monitored by time-lapse microscopy. Motility parameters are evaluated over a ~ 10 hours time window centered on the peak of motility of RAB5A cells. (A-C) Plots on the left refer to mean values of the whole monolayers, while plots on the right distinguish between control (blue) and RAB5A-overexpressing (red) cells. (A) Root mean square velocity (V_{rms}) in the centre of mass reference frame. Blue line is the linear fitting of the data. (B) Mean velocity of the centre of mass (V_{cm}). (C) Polar order parameter ψ. $\psi = 1$ means a perfectly uniform velocity field, $\psi \approx 0$ indicates randomly oriented velocities. (D) Area of cell clusters that percolate the entire field of view relative to the total surface area of RAB5A-expressing MCF10DCIS.com in mixed monolayers as a function of the relative number of RAB5A-cells. (E) Demixing parameter of control and RAB5A cells plotted as a function of the relative amount of RAB5A-MCF10A cells. (F) Length of correlation (L_{corr}), obtained from stretched exponential fits on spatial velocity correlation function curves. (G) Length of persistence (L_{pers}), obtained by fitting the MSD curves with a model function describing the transition from a short-time ballistic to a long-time diffusive behavior. Dashed black lines indicate the percolation threshold of RAB5A cells. Data are the mean $\pm$ S.D (n= 15 fields of view from 3 independent experiments).


A
25% CTRL - 75% RAB5A
Activity map
of local cell velocity
12
10
8
6
4
2
50% CTRL
50% RAB5A
100% RAB5A

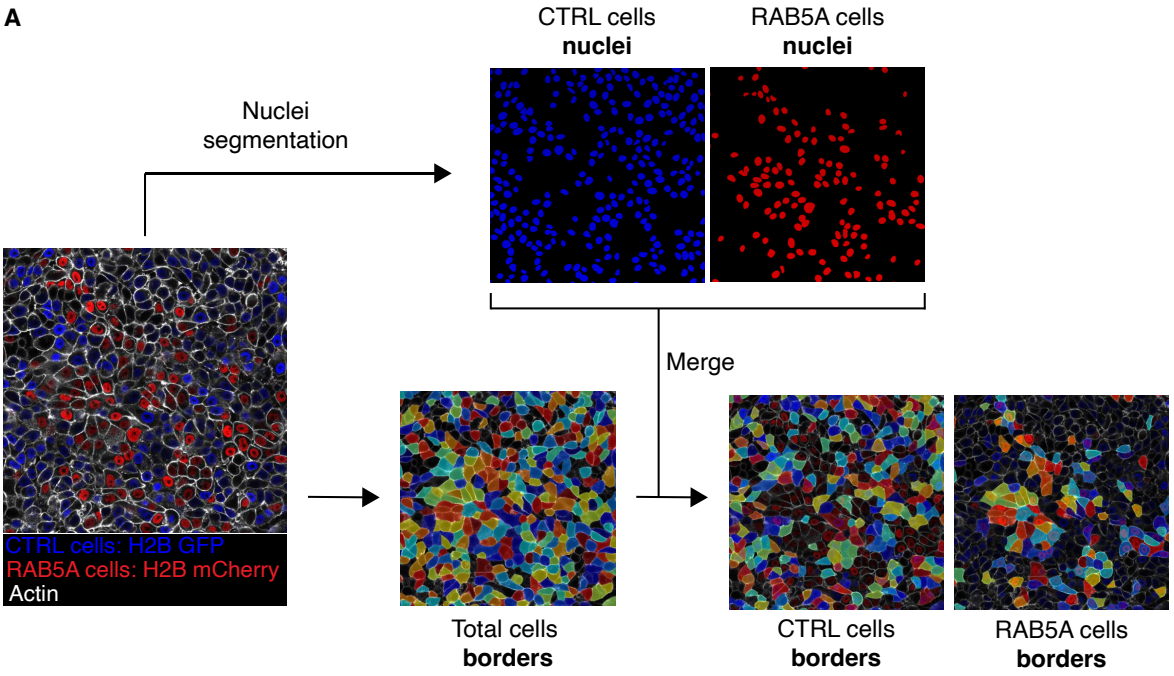

B
Vinculin
RAB5A
RAC1
CTRL
CTRL
RAC1 DN
RAB5A

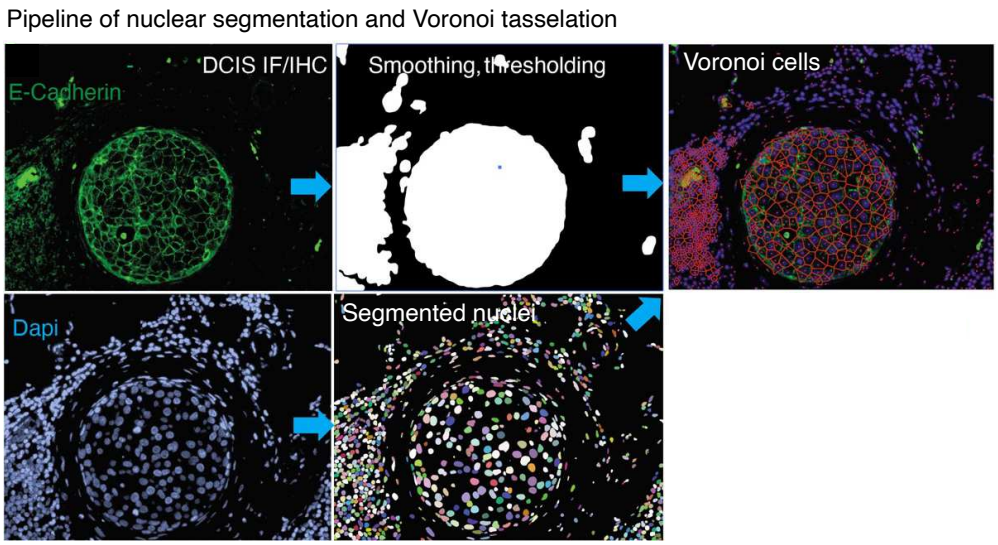

C
Wild Type
RAC1 DN
CTRL
RAB5A
V_{rms} (µm/h)
Fraction of RAB5A cells (%)
0
10
20
30
40
0
20
40
60
80
100

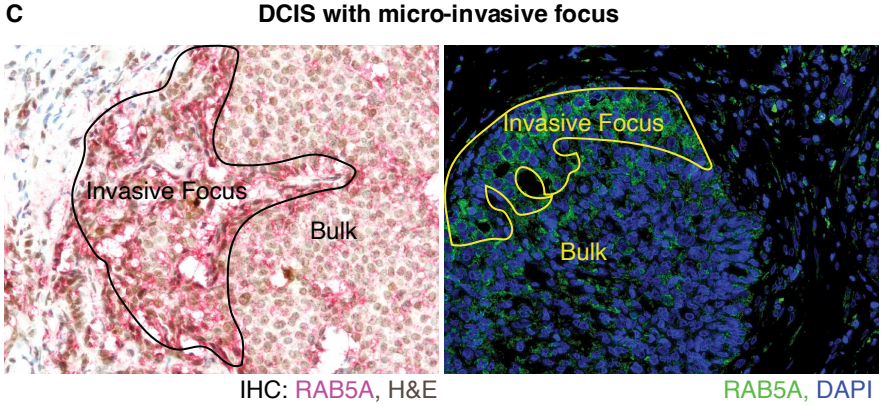

D
Motility parameters of 100% CTRL cells
Mean velocity
RMS velocity
Correlation length
Persistence length
V_{CM} (µm/h)
V_{rms} (µm/h)
L_{corr} (µm)
L_{pers} (µm)
ns
WT
RAC1 DN

Supplementary figure 3.

(A) Left: fluorescent snapshot image from time-lapse movie of control (blue nuclei) and RAB5A-expressing (red nuclei) MCF10DCIS.com cells seeded as mixed monolayers to prevent percolation, as described in the main text. Right: activity map of the local decorrelation rate Γ^* (1/hours), which measures the opposite of the time needed by a cell to move with a displacement corresponding to the cell size. Black arrows represent an instantaneous velocity field, as obtained from PIV analysis of two consecutive frames collected about 8 hours after the beginning of the acquisition. (B) Immunoblot with the indicated antibodies of total lysates of doxycycline-treated CTRL, CTRL RAC1-DN and RAB5A monolayers. Vinculin was used as loading control. (C) Root mean square velocity (V_{rms}) in the center of mass reference frame calculated in the experimental conditions as in Fig.3E, distinguishing between control (blue) and RAB5A-overexpressing (red) cells. Plot on the left refers to mixed monolayers composed of RAB5A cells and WT controls, while plot on the right refers to mixed monolayers composed of RAB5A cells and RAC1-DN controls. (D) Motility parameters of control MCF10DCIS.com monolayers Wild-Type (WT) or expressing RAC1(T17N), a mutant dominant-negative form of RAC1 (RAC1 DN). The values were obtained by nuclear tracking of monolayers monitored by time-lapse microscopy and were evaluated over a ~ 7 hours time window. Mean velocity of the centre of mass (V_{cm}), root mean square velocity (V_{rms}) in the center of mass reference frame, length of correlation (L_{corr}), obtained from stretched exponential fits on spatial velocity correlation function curves, length of persistence (L_{pers}), obtained by fitting the MSD curves with a model function describing the transition from a short-time ballistic to a long-time diffusive behavior. Unpaired t-tests (from left to right and from top to bottom, ns: p=0.9574, p=0.3271, p=0.8090, p=0.1987). Data are the mean $\pm$ S.D (WT, n= 40 fields of view from 8 independent experiments; RAC1 DN, n= 45 fields of view from 9 independent experiments).

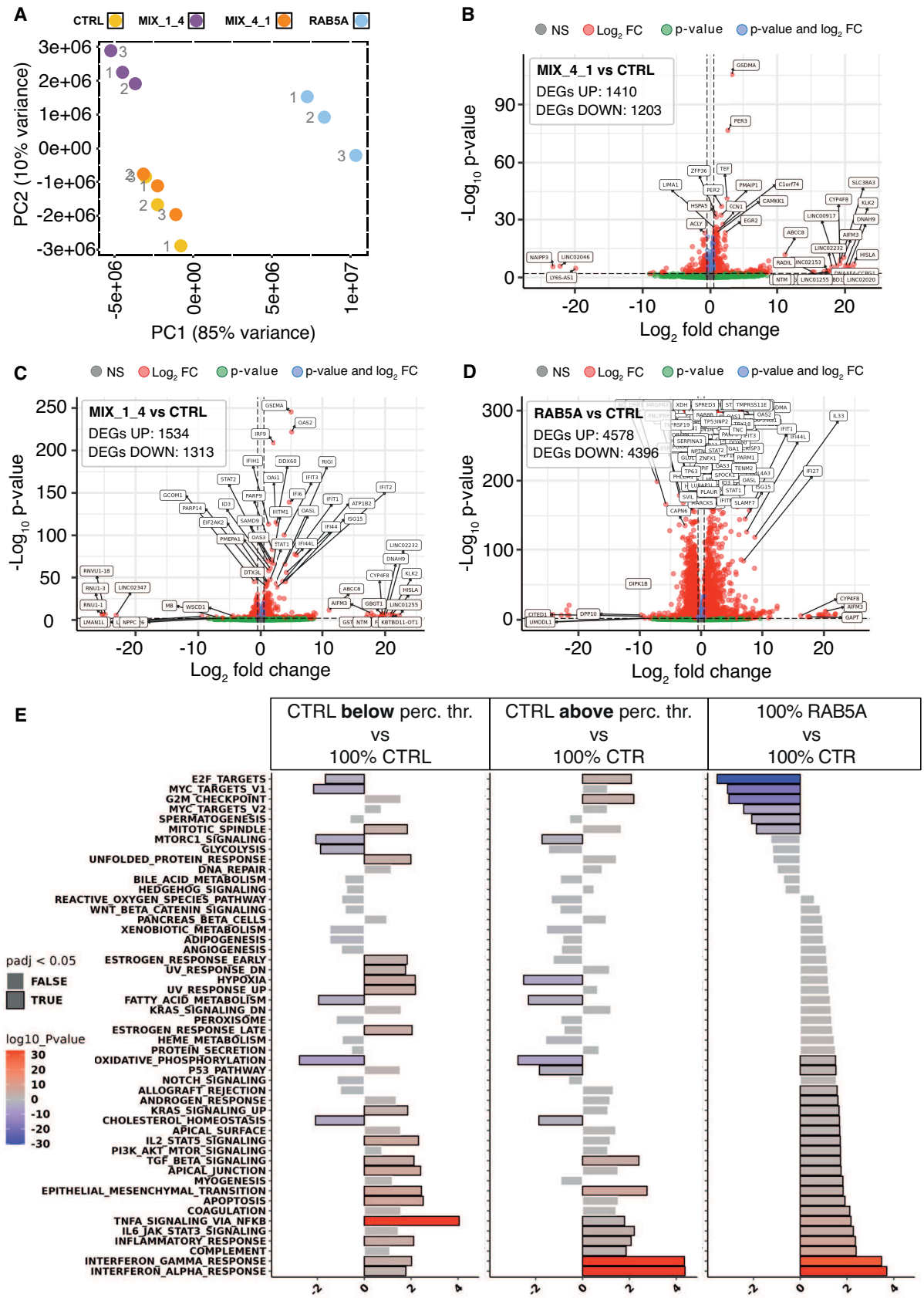

A
CTRL cells
nuclei
RAB5A cells
nuclei
Nuclei
segmentation
Merge
CTRL cells: H2B GFP
RAB5A cells: H2B mCherry
Actin
Total cells
borders
CTRL cells
borders
RAB5A cells
borders


B
Pipeline of nuclear segmentation and Voronoi tasselation
DCIS IF/IHC
E-Cadherin
Smoothing, thresholding
Voronoi cells
Dapi
Segmented nuclei


C
DCIS with micro-invasive focus
Invasive Focus
Bulk
Invasive Focus
Bulk
IHC: RAB5A, H&E
RAB5A, DAPI

Supplementary figure 4.

(A) Cell segmentation image analysis pipeline. Immunofluorescence images of control (blue) and RAB5A-expressing (red) MCF10DCIS.com cells seeded at various relative ratios to form confluent mixed monolayers. Cells were stimulated with doxycycline to induce RAB5A expression, fixed after 24 hours and stained with Phalloidin to detect F-actin. Middle-plane confocal images were acquired and processed using an automated image analysis pipeline. Total cell borders and fluorescent nuclei from control or RAB5A-cells were segmented with Cellpose. Nuclear and cellular masks were then merged to obtain control and RAB5A cellular borders masks. AR was then extracted for each individual cell. (B) Image analysis pipeline for quantifying geometric features in human DCIS and IDC samples. Cells were stained with E-cadherin and Dapi and the pipeline described in the text was applied to automatically segment nuclei, and define a cell centroid for Voronoi reconstruction of cell boundaries and shape. (C) Representative human DCIS with micro-invasive focus: (Left) Immunohistochemistry, RAB5A (red), H&E; (Right) Multiplex immunohistochemistry/immunofluorescence, RAB5A (green) and DAPI.


A
CTRL
MIX_1_4
MIX_4_1
RAB5A
PC2 (10% variance)
PC1 (85% variance)
B
NS
Log2 FC
p-value
p-value and log2 FC
MIX_4_1 vs CTRL
DEGs UP: 1410
DEGs DOWN: 1203
-Log10 p-value
Log2 fold change
C
MIX_1_4 vs CTRL
DEGs UP: 1534
DEGs DOWN: 1313
D
RAB5A vs CTRL
DEGs UP: 4578
DEGs DOWN: 4396
E
CTRL below perc. thr. vs 100% CTRL
CTRL above perc. thr. vs 100% CTR
100% RAB5A vs 100% CTR
padj < 0.05
FALSE
TRUE
log10_Pvalue
E2F_TARGETS
MYC_TARGETS_V1
G2M_CHECKPOINT
MYC_TARGETS_V2
SPERMATOGENESIS
MITOTIC_SPINDLE
MTORC1_SIGNALING
GLYCOLYSIS
UNFOLDED_PROTEIN_RESPONSE
DNA_REPAIR
BILE_ACID_METABOLISM
HEDGEHOG_SIGNALING
REACTIVE_OXYGEN_SPECIES_PATHWAY
WNT_BETA_CATENIN_SIGNALING
PANCREAS_BETA_CELLS
XENOBIOTIC_METABOLISM
ADIPOGENESIS
ANGIOGENESIS
ESTROGEN_RESPONSE_EARLY
UV_RESPONSE_DN
HYPOXIA
UV_RESPONSE_UP
FATTY_ACID_METABOLISM
KRAS_SIGNALING_DN
PEROXISOME
ESTROGEN_RESPONSE_LATE
HEME_METABOLISM
PROTEIN_SECRETION
OXIDATIVE_PHOSPHORYLATION
P53_PATHWAY
NOTCH_SIGNALING
ALLOGRAFT_REJECTION
ANDROGEN_RESPONSE
KRAS_SIGNALING_UP
CHOLESTEROL_HOMEOSTASIS
APICAL_SURFACE
IL2_STAT5_SIGNALING
PI3K_AKT_MTOR_SIGNALING
TGF_BETA_SIGNALING
APICAL_JUNCTION
MYOGENESIS
EPITHELIAL_MESENCHYMAL_TRANSITION
APOPTOSIS
COAGULATION
TNFA_SIGNALING_VIA_NFKB
IL6_JAK_STAT3_SIGNALING
INFLAMMATORY_RESPONSE
COMPLEMENT
INTERFERON_GAMMA_RESPONSE
INTERFERON_ALPHA_RESPONSE

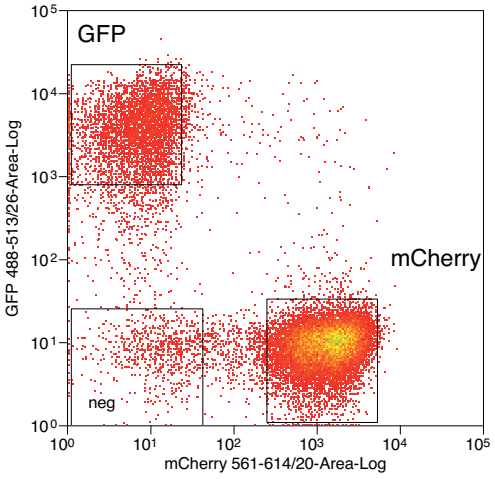
Supplementary figure 5.

(A) Whole transcriptome dimensionality reduction by PCA highlighting the similarities between RAB5A-monolayers (RAB5A) and controls isolated from pure (CTRL) or mixed monolayers below (MIX_4_1) or above (MIX_1_4) the percolation threshold. (B-D) Volcano plots depicting genes associated with significantly top 50 up and down regulated genes for the following comparisons: (B) controls isolated from mixed monolayers below the percolation threshold (MIX_4_1) vs 100% controls (CTRL); (C) controls isolated from mixed monolayers above the percolation threshold (MIX_1_4) vs 100% controls (CTRL); RAB5A vs control monolayers. The y axis indicates the $-\log_{10}$ P-value, whereas the x axis ($\log_2$ fold change) indicates gene expression. Each dot represents a gene. (E) Gene set enrichment analysis (GSEA) of deregulated genes (DEGs) in RAB5A-monolayers or controls isolated from mixed monolayers below or above the percolation threshold of RAB5A cells against 100% control cells. Moderated t-statistic was used to rank the genes. Significantly enriched pathways (one-sided P-value < 0.05) are indicated with solid black outline of the bar corresponding to the Bonferroni-Hochberg-adjusted P-value. P-value was calculated as the number of random genes with the same or more extreme NES (Normalized Enrichment Score) value divided by the total number of generated gene sets. Pathways were organized according to NES associates to RAB5A comparison list.

Pre-sorting

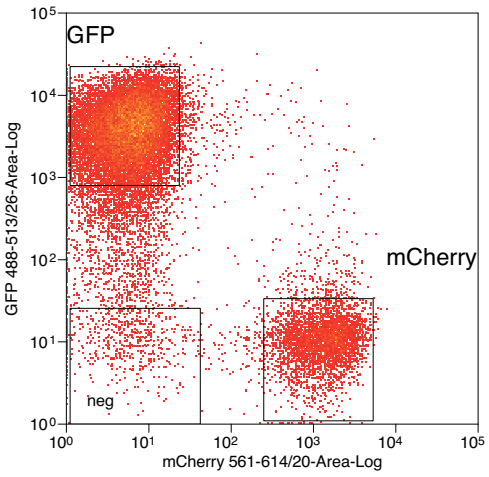
A

20% CTRL : 80% RAB5



Region	Count	% Hist	% All
Total	24165	100.00	64.54
GFP	4450	18.42	11.88
mCherry	17203	71.19	45.94
neg	713	2.95	1.90

80% CTRL : 20% RAB5

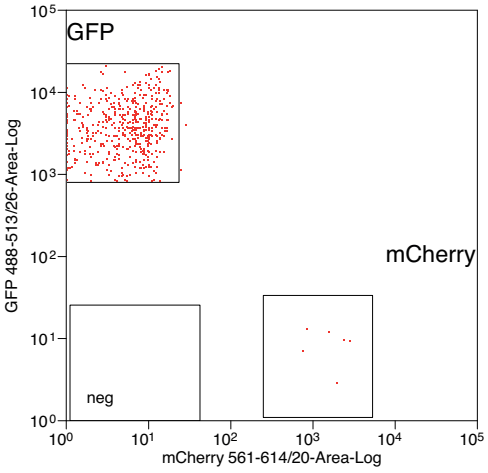


Region	Count	% Hist	% All
Total	25830	100.00	67.35
GFP	16436	63.63	42.86
mCherry	4127	15.98	10.76
neg	542	2.10	1.41

Post-sorting

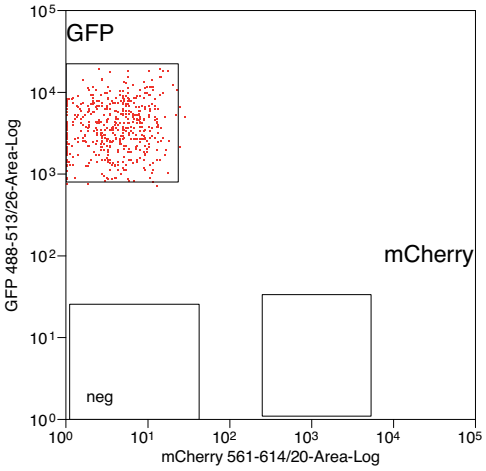
B

20% CTRL : 80% RAB5



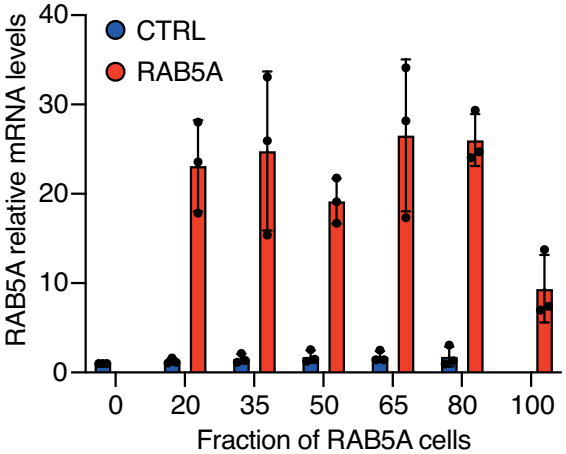
Region	Count	% Hist
Total	521	100.00
GFP	512	98.27
mCherry	6	1.15

80% CTRL : 20% RAB5



Region	Count	% Hist
Total	526	100.00
GFP	520	98.86
mCherry	0	0.00

C



Supplementary figure 6.

Mixed control and RAB5A-expressing MCF10DCIS.com monolayers were prepared and processed as described in the main text. Representative percentages of gated cells before (A) and after (B) FACS sorting. Gates were set based on GFP (control) and mCherry (RAB5A) H2B fluorescent markers. (C) mRNA expression levels of RAB5A determined by qRT-PCR in control and RAB5A MCF10DCIS.com cells isolated from mixed monolayers. Values were normalized on 100% control sorted monolayers and are the mean $\pm$ SD (n=3 independent experiments).

Supplementary Movies Legends

Supplementary Movie 1. Representative movies of GFP-H2B control (blue) and mCherry-H2B (red) RAB5A-MCF10DCIS.com cells seeded at various relative ratios to form confluent mixed monolayers. Mixed monolayers were treated with $2.5\,\mu g/ml$ doxycycline to induce RAB5A expression and monitored by time-lapse fluorescence microscopy acquiring images every 5 minutes over a 48 hours period (first 30 hours are shown).

Supplementary Movie 2. Representative movies of GFP-H2B control (blue) and mCherry-H2B (red) RAB5A-MCF10A cells seeded at various relative ratios to form confluent mixed monolayers. Mixed monolayers were treated with $2.5\,\mu g/ml$ doxycycline to induce RAB5A expression and monitored by time-lapse fluorescence microscopy acquiring images every 5 minutes over a 24 hours period.

Supplementary Movie 3. GFP-H2B control (blue) and mCherry-H2B (red) RAB5A-MCF10DCIS.com cells were seeded as mixed monolayers to prevent percolation, as described in the main text. On the left side of the monolayer, control and RAB5A-cells were mixed at 50:50 relative ratio, while on the right side only RAB5A-cells were present. Mixed monolayers were treated with $2.5\,\mu g/ml$ doxycycline to induce RAB5A expression and monitored by time-lapse fluorescence microscopy acquiring images every 5 minutes over a 48 hours period.

Supplementary Movie 4. Representative phase-contrast and fluorescent time-lapse movies of cryptic lamellipodia extension in mixed control and RAB5A-MCF10DCIS.com monolayers. GFP-LifeAct and unlabeled control or RAB5A-MCF10DCIS.com cells were mixed (1:10 ratio) to correctly visualize actin-based cryptic lamellipodia. Mixed monolayers were treated with $2.5\,\mu g/ml$ doxycycline to induce RAB5A expression and monitored by time-lapse fluorescence microscopy acquiring images every 1.5 min over a 4 hours period.

Supplementary Movie 5. Representative movies of GFP-H2B control (blue) and mCherry-H2B (red) RAB5A-MCF10DCIS.com cells seeded at various relative ratios to form confluent mixed monolayers. Top panels are mixed monolayers composed of RAB5A cells and WT controls, while bottom panels are mixed monolayers composed of RAB5A cells and control cells expressing RAC1(T17N), a mutant dominant-negative (DN) form of RAC1. Mixed monolayers were treated with $2.5\,\mu g/ml$ doxycycline to induce RAB5A expression and monitored by time-lapse fluorescence microscopy acquiring images every 5 minutes over a 48 hours period.

Supplementary Movie 6. Representative movies of control (CTRL) or RAB5A-MCF10DCIS.com cells seeded at various densities. Cells were treated with 2.5 µg/ml doxycycline to induce RAB5A expression and monitored by time-lapse fluorescence microscopy acquiring images every 15 min over a 48 hours period.

Supplementary Material: Hydrodynamic Model

In this supplementary material, we first define a minimal microscopic model that captures the main ingredients of the agent-based model analyzed in numerical simulations. Beyond our experimental system of mixtures of Rab5a and CTRL cells, it describes more generally, with minimal hypothesis, mixtures of 2 cell types, which are modeled as active particles with both soft core pairwise interactions, and aligning interactions. We then present a coarse-graining procedure of this microscopic model and derive the corresponding general hydrodynamic equations, which we show are independent of the specific choice of aligning interaction, supporting the broad applicability of our findings. The analysis of spatially uniform states yields an explicit quantitative characterization of the flocking transition as a supercritical bifurcation.

1.19 Definition of the microscopic model

Interacting motile cells – typically either RAB5A cells or CTRL cells – are described on minimal grounds as 2-dimensional Active Brownian Particles (ABPs), endowed with soft disk repulsive pairwise interactions. In this section we assume a classical pairwise aligning interaction between polarity vectors of neighboring cells, similar to flying XY models [62, 63]. The case of self-alignment [36, 64] is discussed in the next section.

1.19.1 One population dynamics

A cell (particle) i is characterized by its position r_i and the angle θ_i that defines the direction of its self-propulsion vector (polarity) $\mathbf{n}_i = (\cos\theta_i, \sin\theta_i)$; we denote by v_0 the constant norm of the self-propulsion velocity, and by μ the cell mobility. Denoting $\mathbf{r}_{ij} = \mathbf{r}_j - \mathbf{r}_i, r_{ij} = |\mathbf{r}_{ij}|$, the soft disk repulsive interaction force between cells i, j can be written : $\mathbf{F}_{ij} = k(2a - r_{ij})\mathbf{r}_{ij}/r_{ij}$ if $r_{ij} < 2a$ and $F_{ij} = 0$ otherwise, where a is the cell radius. In the rotational equation of motion, angular fluctuations are modeled by introducing a white noise η_i with zero mean and correlations $< \eta_i(t)\eta_j(t') >= 2D\delta_{ij}\delta(t - t')$. The rotational equation also includes a torque of intensity J redirecting the orientation of the particle along the orientation of the neighbors it is interacting with: $\tau_{ij} = J\sin(\theta_j - \theta_i)$ for $r_{ij} < 2a$ and $\tau_{ij} = 0$ otherwise. The dynamics of each

cell i in the population then obey:

$$\begin{cases} \dot{\mathbf{r}}_i = v_0 \mathbf{n}_i + \mu \sum_j \mathbf{F}_{ij}, \\ \dot{\theta}_i = \sum_j \tau_{ij} + \eta_i. \end{cases} \tag{7}$$

1.19.2 Mixed population dynamics

For a mixed population of N_R RAB5A particles, and N_C CTRL particles, all of radius a, the position and self-propulsion angle of each RAB5A cell are denoted $r_{R,i}, \theta_{R,i}$ and the position and self-propulsion angle of each CTRL cell are denoted $r_{C,i}, \theta_{C,i}$. The microscopic dynamics is then defined by the coupled Langevin equations:

$$\begin{cases} \dot{\mathbf{r}}_{R,i} = v_{0R} \mathbf{n}_{R,i} + \mu \sum_{j \in R,C} \mathbf{F}_{ij}, \\ \dot{\theta}_{R,i} = \sum_{j \in R} \tau_{ij}^{RR} + \sum_{j \in C} \tau_{ij}^{RC} + \eta_{R,i}, \\ \dot{\mathbf{r}}_{C,i} = v_{0C} \mathbf{n}_{C,i} + \mu \sum_{j \in R,C} \mathbf{F}_{ij}, \\ \dot{\theta}_{C,i} = \sum_{j \in C} \tau_{ij}^{CC} + \sum_{j \in R} \tau_{ij}^{CR} + \eta_{C,i}, \end{cases} \tag{8}$$

where the self-propulsion velocities for each population X is v_{0X}, the rotational torques are $\tau_{ij}^{XY} = J_{XY} \sin(\theta_{Y,j} - \theta_{X,i})$, and the rotational noises have a variance: $< \eta_{X,i}(t) \eta_{Y,j}(t') >= 2 D_X \delta_{ij} \delta(t - t') \delta_{XY}$, where X and Y can be R, C. In general, the couplings J_{XY} can take any positive value for aligning interactions, and do not need to be symmetric (interactions could be non reciprocal in such non equilibrium system). We derive below the coarse grained hydrodynamic equations of such generic binary cell mixture, and next discuss its application to our experimental example of RAB5A and CTRL cells.

1.20 Coarse-graining of the microscopic model

We follow the methodology of Ref. [37] to coarse-grain the microscopic model and derive the corresponding hydrodynamic equations.

1.20.1 BBGKY coarse-graining

The empirical one-particle densities of RAB5A c_R and of CTRL c_C are defined (up to a factor $N_R + N_C$) as the probability distribution of finding a RAB5A cell or a CTRL cell at position **r** with

a self-propulsion direction θ at time t. They are defined as follows:

$$
\begin{aligned}
c_R(\mathbf{r},\theta,t) &= \big\langle \frac{1}{2\pi V}\sum_{i\in R}\delta(\mathbf{r}_{R,i}(t)-\mathbf{r})\delta(\theta_{R,i}(t)-\theta)\big\rangle,\\
c_C(\mathbf{r},\theta,t) &= \big\langle \frac{1}{2\pi V}\sum_{i\in C}\delta(\mathbf{r}_{C,i}(t)-\mathbf{r})\delta(\theta_{C,i}(t)-\theta)\big\rangle,
\end{aligned}
\tag{9}
$$

where V is the volume of the system, and the normalization is chosen so that the angular moments of the distributions yield the densities of particle $\int_0^{2\pi} c_X d\theta = \rho_X$.

The two particle joint distributions are defined as:

$$
\begin{aligned}
c_{RR}(\mathbf{r},\theta,\mathbf{r}',\theta',t) &= \big\langle \frac{1}{(2\pi V)^2}\sum_{i,j\in R, i<j}\delta(\mathbf{r}_{R,i}(t)-\mathbf{r})\delta(\theta_{R,i}(t)-\theta)\delta(\mathbf{r}_{R,j}(t)-\mathbf{r}')\delta(\theta_{R,j}(t)-\theta')\big\rangle,\\
c_{CC}(\mathbf{r},\theta,\mathbf{r}',\theta',t) &= \big\langle \frac{1}{(2\pi V)^2}\sum_{i,j\in C, i\neq j}\delta(\mathbf{r}_{C,i}(t)-\mathbf{r})\delta(\theta_{C,i}(t)-\theta)\delta(\mathbf{r}_{C,j}(t)-\mathbf{r}')\delta(\theta_{C,j}(t)-\theta')\big\rangle,\\
c_{RC}(\mathbf{r},\theta,\mathbf{r}',\theta',t) &= \big\langle \frac{1}{(2\pi V)^2}\sum_{i\in R, j\in C}\delta(\mathbf{r}_{R,i}(t)-\mathbf{r})\delta(\theta_{R,i}(t)-\theta)\delta(\mathbf{r}_{C,j}(t)-\mathbf{r}')\delta(\theta_{C,j}(t)-\theta')\big\rangle.
\end{aligned}
\tag{10}
$$

In a first approximation, and because we aim eventually at analyzing spatially uniform states, we neglect correlations and make use of the following lowest order decoupling hypothesis:

$$
c_{XY}(\mathbf{r},\theta,\mathbf{r}',\theta',t) = c_X(\mathbf{r},\theta,t)c_Y(\mathbf{r}',\theta',t). \tag{11}
$$

This yields the noise-averaged Smoluchowski equations for each population:

$$
\begin{aligned}
&\partial_t c_R(\mathbf{r},\theta,t) = -v_{0R}\mathbf{n}_R.\nabla c_R(\mathbf{r},\theta,t) + \nabla.(D_{\mathsf{eff}}c_R(\mathbf{r},\theta,t)\nabla\rho(\mathbf{r},t))\\
&- j_{RR}\partial_\theta\int_0^{2\pi} d\theta' \sin(\theta'-\theta)c_R(\mathbf{r},\theta,t)c_R(\mathbf{r},\theta',t) - j_{RC}\partial_\theta\int_0^{2\pi} d\theta' \sin(\theta'-\theta)c_R(\mathbf{r},\theta,t)c_C(\mathbf{r},\theta',t)\\
&+ D_R\partial^2_{\theta\theta}c_R(\mathbf{r},\theta,t),\\
&\partial_t c_C(\mathbf{r},\theta,t) = -v_{0C}\mathbf{n}_C.\nabla c_C(\mathbf{r},\theta,t) + \nabla.(D_{\mathsf{eff}}c_C(\mathbf{r},\theta,t)\nabla\rho(\mathbf{r},t))\\
&- j_{CC}\partial_\theta\int_0^{2\pi} d\theta' \sin(\theta'-\theta)c_C(\mathbf{r},\theta,t)c_C(\mathbf{r},\theta',t) - j_{CR}\partial_\theta\int_0^{2\pi} d\theta' \sin(\theta'-\theta)c_C(\mathbf{r},\theta,t)c_R(\mathbf{r},\theta',t)\\
&+ D_C\partial^2_{\theta\theta}c_C(\mathbf{r},\theta,t)
\end{aligned}
\tag{12}
$$

where $D_{\text{eff}} = (8/5)\mu k\pi a^5$ and $j_{XY} = 4\pi a^2 J_{XY}$, and $\rho = \rho_R + \rho_C$. The pseudo-diffusion contribution $D_{\text{eff}}\nabla\rho$ stems from short range elastic repulsion between the particles. It is obtained by expanding $c(\mathbf{r}', \theta', t)$ around $\mathbf{r}$: $c(\mathbf{r} + \Delta\mathbf{r}, \theta', t) = c(\mathbf{r}, \theta', t) + \Delta\mathbf{r}.\nabla c(\mathbf{r}, \theta', t)$.

We next define the angular moments of the probability density:

$$f_n^X = \int_0^{2\pi} d\theta \, \mathrm{e}^{in\theta} \, c_X, \tag{13}$$

where $f_0^X = \rho_X, f_1^X = \mathsf{P}_X, f_2^X = \mathsf{Q}_X$. The $n = 1$ polar moment in real space is defined as $\mathbf{P}_X = \{P_{X,x}, P_{X,y}\}$ with $\mathsf{P}_X = P_{X,x} + iP_{X,y}$. We write the equations up to the second moment in the complex space. Following Ref. [37] the system is closed by neglecting higher order terms, and the time and spatial derivatives of the second moment:

$$\begin{cases} \partial_t \rho_R = -\frac{v_{0R}}{2}(\partial_z \mathsf{P}_R + \partial_{\bar{z}} \bar{\mathsf{P}}_R) + \nabla.(D_{\text{eff}} \rho_R \nabla\rho), \\ \partial_t \mathsf{P}_R = -\frac{v_{0R}}{2}(\partial_z \mathsf{Q}_R + \partial_{\bar{z}} \rho_R) + \frac{D_{\text{eff}}}{2}(\partial_z \mathsf{P}_R \partial_z \rho + \partial_{\bar{z}} \mathsf{P}_R \partial_{\bar{z}} \rho + 2\mathsf{P}_R \partial_z \partial_{\bar{z}} \rho) - D_R \mathsf{P}_R \\ \qquad\qquad + j_{RR}(\rho_R \mathsf{P}_R - \bar{\mathsf{P}}_R \mathsf{Q}_R) + j_{RC}(\rho_R \mathsf{P}_C - \bar{\mathsf{P}}_C \mathsf{Q}_R), \\ 0 = -\frac{v_{0R}}{2}(\partial_{\bar{z}} \mathsf{P}_R) - 4D_R \mathsf{Q}_R + 2j_{RR} \mathsf{P}_R \mathsf{P}_R + 2j_{RC} \mathsf{P}_R \mathsf{P}_C, \end{cases} \tag{14}$$

$$\begin{cases} \partial_t \rho_C = -\frac{v_{0C}}{2}(\partial_z \mathsf{P}_C + \partial_{\bar{z}} \bar{\mathsf{P}}_C) + \nabla.(D_{\text{eff}} \rho_C \nabla\rho), \\ \partial_t \mathsf{P}_C = -\frac{v_{0C}}{2}(\partial_z \mathsf{Q}_C + \partial_{\bar{z}} \rho_C) + \frac{D_{\text{eff}}}{2}(\partial_z \mathsf{P}_C \partial_z \rho + \partial_{\bar{z}} \mathsf{P}_C \partial_{\bar{z}} \rho + 2\mathsf{P}_C \partial_z \partial_{\bar{z}} \rho) - D_C \mathsf{P}_C \\ \qquad\qquad + j_{CC}(\rho_C \mathsf{P}_C - \bar{\mathsf{P}}_C \mathsf{Q}_C) + j_{CR}(\rho_C \mathsf{P}_R - \bar{\mathsf{P}}_R \mathsf{Q}_C), \\ 0 = -\frac{v_{0C}}{2}(\partial_{\bar{z}} \mathsf{P}_C) - 4D_C \mathsf{Q}_C + 2j_{CC} \mathsf{P}_C \mathsf{P}_C + 2j_{CR} \mathsf{P}_R \mathsf{P}_C, \end{cases} \tag{15}$$

where $\partial_z = \partial_x - i\partial_y, \partial_{\bar{z}} = \partial_x + i\partial_y$.

Rewriting the equations for the first and second moment in real space leads to:

$$\begin{cases} \partial_t \rho_R = -v_{0R} \nabla . \mathbf{P}_R + \nabla . (D_{\text{eff}} \rho_R \nabla \rho) \\ \partial_t \rho_C = -v_{0C} \nabla . \mathbf{P}_C + \nabla . (D_{\text{eff}} \rho_C \nabla \rho) \\ \partial_t \mathbf{P}_R = -\frac{v_{0R}}{2} \nabla \rho_R + D_{\text{eff}} \nabla . (\mathbf{P}_R \nabla \rho) + \frac{v_{0R}^2}{16 D_R} \nabla^2 \mathbf{P}_R - \frac{v_{0R} j_{RR}}{2 D_R} \nabla . \mathbf{Q}_R - \frac{v_{0R} j_{RC}}{2 D_R} \nabla . \mathbf{Q}_{RC} - D_R \mathbf{P}_R \\ \qquad -j_{RR}(-\rho_R \mathbf{P}_R + \frac{j_{RR}}{2 D_R} |\mathbf{P}_R|^2 \mathbf{P}_R + \frac{j_{RC}}{2 D_R} |\mathbf{P}_R|^2 \mathbf{P}_C - \frac{v_{0R}}{4 D_R} (\nabla (|\mathbf{P}_R|^2) - 2 \mathbf{P}_R \nabla . \mathbf{P}_R)) \\ \qquad -j_{RC}(-\rho_R \mathbf{P}_C + \frac{j_{RR}}{4 D_R} \mathbf{P}_C . \mathbf{Q}_R + \frac{j_{RC}}{4 D_R} |\mathbf{P}_C|^2 \mathbf{P}_R - \frac{v_{0R}}{2 D_R} (\mathbf{P}_C \nabla \mathbf{P}_R - \mathbf{P}_C \nabla . \mathbf{P}_R)) \\ \partial_t \mathbf{P}_C = -\frac{v_{0C}}{2} \nabla \rho_C + D_{\text{eff}} \nabla . (\mathbf{P}_C \nabla \rho) + \frac{v_{0C}^2}{16 D_C} \nabla^2 \mathbf{P}_C - \frac{v_{0C} j_{CC}}{2 D_C} \nabla . \mathbf{Q}_C - \frac{v_{0C} j_{CR}}{2 D_C} \nabla . \mathbf{Q}_{RC} - D_C \mathbf{P}_C \\ \qquad -j_{CC}(-\rho_C \mathbf{P}_C + \frac{j_{CC}}{2 D_C} |\mathbf{P}_C|^2 \mathbf{P}_C + \frac{j_{CR}}{2 D_C} |\mathbf{P}_C|^2 \mathbf{P}_R - \frac{v_{0C}}{4 D_C} (\nabla (|\mathbf{P}_C|^2) - 2 \mathbf{P}_C \nabla . \mathbf{P}_C)) \\ \qquad -j_{CR}(-\rho_C \mathbf{P}_R + \frac{j_{CC}}{2 D_C} \mathbf{P}_R . \mathbf{Q}_C + \frac{j_{CR}}{2 D_C} |\mathbf{P}_R|^2 \mathbf{P}_C - \frac{v_{0C}}{2 D_C} (\mathbf{P}_R \nabla \mathbf{P}_C - \mathbf{P}_R \nabla . \mathbf{P}_C)) \end{cases} \tag{16}$$

where we defined the nematic tensors $Q_{X,ij} = (P_{X,i} P_{X,j} - \delta_{ij} P_{X,k} P_{X,k}/2)$, and $Q_{XY,ij} = (P_{X,i} P_{Y,j} - \delta_{ij} P_{X,k} P_{Y,k}/2)$

1.20.2 Uniform steady state

Writing the equations in the uniform and steady state leads to:

$$\begin{cases} \rho_R \mathbf{v}_R = v_{0R} \mathbf{P}_R, \quad \rho_C \mathbf{v}_C = v_{0C} \mathbf{P}_C, \\ 0 = -D_R \mathbf{P}_R - j_{RR}(-\rho_R \mathbf{P}_R + \frac{j_{RR}}{2 D_R} |\mathbf{P}_R|^2 \mathbf{P}_R + \frac{j_{RC}}{2 D_R} |\mathbf{P}_R|^2 \mathbf{P}_C) - j_{RC}(-\rho_R \mathbf{P}_C + \frac{j_{RR}}{D_R} \mathbf{P}_C . \mathbf{Q}_R + \frac{j_{RC}}{2 D_R} |\mathbf{P}_C|^2 \mathbf{P}_R), \\ 0 = -D_C \mathbf{P}_C - j_{CC}(-\rho_C \mathbf{P}_C + \frac{j_{CC}}{2 D_C} |\mathbf{P}_C|^2 \mathbf{P}_C + \frac{j_{CR}}{2 D_C} |\mathbf{P}_C|^2 \mathbf{P}_R) - j_{CR}(-\rho_C \mathbf{P}_R + \frac{j_{CC}}{D_C} \mathbf{P}_R . \mathbf{Q}_C + \frac{j_{CR}}{2 D_C} |\mathbf{P}_R|^2 \mathbf{P}_C). \end{cases} \tag{17}$$

Note that these equations are symmetric upon switching $R \leftrightarrow C$ as expected. We discuss the specific case of RAB5A and CTRL cell mixtures below.

1.20.3 RAB5A and CTRL cell mixtures

In the model presented in the main text, we assume that: (i) RAB5A cells align with each other so that $j_{RR} > 0$, (ii) CTRL cells do not align with each other so that $j_{CC} = 0$, (iii) RAB5A cells align with CTRL cells so that $j_{RC} > 0$, and (iv) CTRL cells may align with RAB5A cells ($j_{CR} > 0$) except if they are dissenters (RAC1(T17N) control cells, where $j_{CR} = 0$).

Taking $j_{CC} = 0$ yields the following equations:

$$\begin{cases} \rho_R \mathbf{v}_R = v_{0R} \mathbf{P}_R, \quad \rho_C \mathbf{v}_C = v_{0C} \mathbf{P}_C, \\ 0 = -D_R \mathbf{P}_R - j_{RR}(-\rho_R \mathbf{P}_R + \frac{j_{RR}}{2D_R} |\mathbf{P}_R|^2 \mathbf{P}_R + \frac{j_{RC}}{2D_R} |\mathbf{P}_R|^2 \mathbf{P}_C) - j_{RC}(-\rho_R \mathbf{P}_C + \frac{j_{RR}}{D_R} \mathbf{P}_C . \mathbf{Q}_R + \frac{j_{RC}}{2D_R} |\mathbf{P}_C|^2 \mathbf{P}_R), \\ 0 = -D_C \mathbf{P}_C - j_{CR}(-\rho_C \mathbf{P}_R + \frac{j_{CR}}{2D_C} |\mathbf{P}_R|^2 \mathbf{P}_C). \end{cases} \tag{18}$$

At steady state one has $\mathbf{P}_C \propto \mathbf{P}_R$); we thus define a unit vector e_x so that $\mathbf{P} = P\,\mathsf{e}_x$, and we drop the vector notation to obtain :

$$\begin{cases} \rho_R v_R = v_{0R} P_R, \quad \rho_C v_C = v_{0C} P_C, \\ 0 = (-D_R + j_{RR}\rho_R) P_R + j_{RC} \rho_R P_C - \frac{j_{RR}^2}{2D_R} P_R^2 P_R - \frac{j_{RC} j_{RR}}{D_R} P_R^2 P_C - \frac{j_{RC}^2}{2D_R} P_C^2 P_R, \\ 0 = -D_C P_C + j_{CR} \rho_C P_R - \frac{j_{CR}^2}{2D_C} P_R^2 P_C. \end{cases} \tag{19}$$

The above equations are written for the angular moments. The average polarity, defined by $p_X = P_X/\rho_X$, thus finally satisfies:

$$\boxed{\begin{cases} 0 = (-D_R + j_{RR}\rho_R) p_R + j_{RC} \rho_C p_C - \frac{j_{RR}^2}{2D_R} \rho_R^2 p_R^2 p_R - \frac{j_{RC} j_{RR}}{D_R} \rho_R \rho_C p_R^2 p_C - \frac{j_{RC}^2}{2D_R} \rho_C^2 p_C^2 p_R, \\ 0 = -D_C p_C + j_{CR} \rho_R p_R - \frac{j_{CR}^2}{2D_C} \rho_R^2 p_R^2 p_C. \end{cases}} \tag{20}$$

These equations, given in the main text, constitute the main result of the coarse-graining method, and yield explicit expressions of the average polarity for each cell type ; examples are shown in (Fig. 2G) of the main text.

1.20.4 Flocking transition

The flocking transition is defined by the emergence of a non vanishing solution of the above equations for the cell polarities p_C, p_R. The threshold density for such isotropic-polar transition is straightforwardly obtained and reads :

$$-D_R + j_{RR}\rho_R + j_{RC}\rho_C \frac{j_{CR}\rho_R}{D_C} = 0. \tag{21}$$

Assuming a constant total density $\rho = \rho_R + \rho_C$ and defining the volume fraction of the RAB5A cells $\phi = \rho_R/\rho$, we finally obtain the critical volume fraction ϕ^* (see Fig. 2G, inset in the main text):

$$\boxed{\phi^* = \frac{1}{2} + \frac{1 - \sqrt{\left(\frac{\mathsf{j}_{CR}\mathsf{j}_{RC}}{\mathsf{j}_{RR}} + 1\right)^2 - \frac{4\mathsf{j}_{CR}\mathsf{j}_{RC}}{\mathsf{j}_{RR}^2}}}{\frac{2\mathsf{j}_{CR}\mathsf{j}_{RC}}{\mathsf{j}_{RR}}},} \tag{22}$$

where we introduced the dimensionless couplings $j_{XY}\rho/D_X \to \mathsf{j}_{XY}$. The threshold is controlled by two parameters: $\mathsf{j}_{CR}\mathsf{j}_{RC}\mathsf{j}_{RR}^{-1}$ that describes the activation through the interactions between species and j_{RR}^{-1} that describes the behavior of RAB5A cells alone ($\phi = 1$). Of note, in the case of RAC1(T17N) control cells, which act as dissenters, so that $j_{CR} = 0$, the critical fraction is simply given by $\phi^* = D_R/j_{RR}\rho$.

Remark: We simplified the equations by writing $j_{CC} = 0$, in order to minimize the number of parameters. However, the absence of flocking phase for CTRL cells alone only requires that $j_{CC} < D_C/\rho_{max}$, and could thus be realized with non vanishing j_{CC}. With $j_{CC} \neq 0$, the volume fraction threshold is modified as follows:

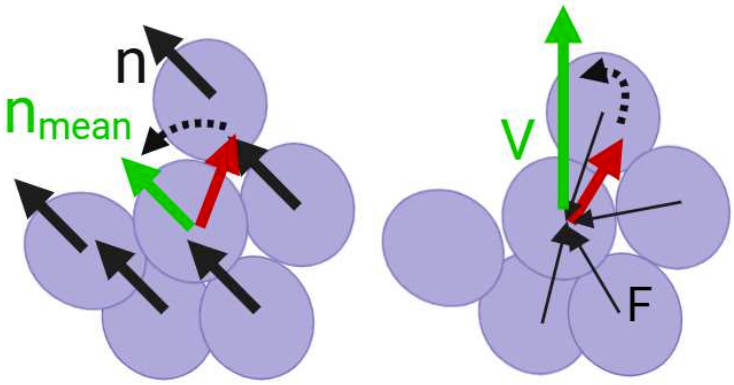
$$\phi^* = \frac{\mathsf{j}_{CC} + \mathsf{j}_{CR}\mathsf{j}_{RC} + \mathsf{j}_{RR} \pm \sqrt{(\mathsf{j}_{CC} + \mathsf{j}_{CR}\mathsf{j}_{RC} + \mathsf{j}_{RR})^2 - 4(\mathsf{j}_{CC}\mathsf{j}_{RR} + \mathsf{j}_{RC}\mathsf{j}_{CR})}}{2(\mathsf{j}_{CC}\mathsf{j}_{RR} + \mathsf{j}_{CR}j_{RC})}. \tag{23}$$

1.21 Robustness of the hydrodynamic model

We now aim at demonstrating that the structure of equations (20) holds independently of the specific choice of microscopic model. While we previously considered an explicit (mutual) alignment rule where cells align with the self-propulsion orientation of their neighbors [65], we extend the analysis to the case of self-alignment [66], where cells align their polarity with their own velocity, which itself depends on elastic interactions between particles.

1.21.1 Implicit alignment rule

The aim of this section is not to derive the exact space and time dependent hydrodynamic equations for the implicit alignment rule in their full generality ; this in principle could be obtained with different dedicated methods, see eg [67–72], but is beyond the scope of this article and is left for further works. Instead, we aim at describing the onset of the flocking transition for a spatially uniform system, which can be discussed as follows.



(a) Explicit alignment (b) Implicit alignment

Figure 1: *Difference between explicit (mutual) and implicit (self) alignment. In the explicit alignment, the orientation* **n** *of a particle (in red) aligns with the mean orientation of its neighbors (in green). In the implicit alignment case, cells align with their own velocity* **V***, that is the combination of both the self propulsion and of the elastic forces* **F** *acting on this particle.*

We consider here an implicit (self) alignment rule, where cells align their self-propulsion direction $\mathbf{n}_i$ with the orientation of their velocity $\mathbf{v}_i$. In this example, we assume for convenience that the amplitude of the aligning torque is proportional to the absolute value of the velocity $v_i = |\mathbf{v}_i|$ where $\mathbf{v}_i = v(\cos\psi_i, \sin\psi_i)$. Last, we set $v_{0R} = v_{0C} = v_0$. The microscopic dynamics is then given by the coupled Langevin equations:

$$\begin{cases} \dot{\mathbf{r}}_{R,i} = v_0 \mathbf{n}_{R,i} + \mu \sum_{j\in R,C} \mathbf{F}_{ij}, \\ \dot{\theta}_{R,i} = J_R v_{R,i} \sin(\psi_{R,i} - \theta_{R,i}) + \eta_{R,i}, \\ \dot{\mathbf{r}}_{C,i} = v_0 \mathbf{n}_{C,i} + \mu \sum_{j\in R,C} \mathbf{F}_{ij} \\ \dot{\theta}_{C,i} = J_C v_{C,i} \sin(\psi_{C,i} - \theta_{C,i}) + \eta_{C,i}. \end{cases} \tag{24}$$

To perform the coarse-graining, we use a mean-field argument to simplify the previous system of equations. This argument consists in writing an effective elastic force independent of the specific positions of the neighbors of each cell. It is based on the assumption of a local elastic behavior for the system at least at short time scales (where a particle is caged by its neighborhood), which is indeed relevant to our experimental system. The equations are first written with only one cell type in large space dimension d, and will next be given for two cell types and $d = 2$. We start by writing:

$$\dot{\mathbf{r}}_i - z_i^{-1} \sum_j \dot{\mathbf{r}}_j = v_0(\mathbf{n}_i - z_i^{-1} \sum_j \mathbf{n}_j) + \mu(\sum_j \mathbf{F}_{ij} - z_i^{-1} \sum_j \sum_k \mathbf{F}_{jk}), \tag{25}$$

where the sums are over the neighboring cells, and z_i is the number of neighbors for the cell i, which is large for d large. Making use of the approximation of a local elastic behavior, we may write $\dot{\mathbf{r}}_i - z_i^{-1}\sum_j \dot{\mathbf{r}}_j \approx 0$, which expresses that the local strain should remain finite in a solid regime. Note that this implicitly assumes a time average over time scales shorter than the elastic time scale. We also neglect the correlations involving next to nearest neighbors, so that: $z_i^{-1}\sum_j\sum_k \mathbf{F}_{jk} \approx 0$. With this assumptions, equation (25) becomes:

$$0 = v_0(\mathbf{n}_i - z_i^{-1}\sum_j \mathbf{n}_j) + \mu\sum_j \mathbf{F}_{ij}. \tag{26}$$

This relation may also be considered as a linear response relation, since at long time scales, the existence of elastic forces at low densities is due only to the self-propulsion forces of nearest neighbors.

Finally, these assumptions lead to the new set of Langevin equations (24):

$$\begin{cases} \dot{\mathbf{r}}_{R,i} = v_0 z_{R,i}^{-1}\left(\sum_{j\in R}\mathbf{n}_{R,j} + \sum_{j\in C}\mathbf{n}_{C,j}\right), \\ \dot{\theta}_{R,i} = J_R v_0 z_{R,i}^{-1}\mathbf{n}_{R,i} \wedge \left(\sum_{j\in R}\mathbf{n}_{R,j} + \sum_{j\in C}\mathbf{n}_{C,j}\right) + \eta_{R,i}, \\ \dot{\mathbf{r}}_{C,i} = v_0 z_{C,i}^{-1}\left(\sum_{j\in R}\mathbf{n}_{R,j} + \sum_{j\in C}\mathbf{n}_{C,j}\right), \\ \dot{\theta}_{C,i} = J_C v_0 z_{C,i}^{-1}\mathbf{n}_{C,i} \wedge \left(\sum_{j\in R}\mathbf{n}_{R,j} + \sum_{j\in C}\mathbf{n}_{C,j}\right) + \eta_{C,i}, \end{cases} \tag{27}$$

where the sums run on the neighbors of the cell.

We next assume small density fluctuations so that $z_{X,i}$ can be approximated by $z_{X,i} \approx V\rho$, where V is the effective volume of one cell and ρ is the local total cell density ; this holds in the large d limit. Following the same steps as above, we obtain the corresponding Smoluchowski equations:

$$\begin{aligned} \partial_t c_R(\mathbf{r},\theta,t) &= -v_0\nabla.\left(\frac{c_R(\mathbf{r},\theta,t)(\mathbf{P}_R+\mathbf{P}_C)}{\rho}\right) - \frac{J_R v_0}{\rho}\partial_\theta\int d\theta' \sin(\theta'-\theta)c_R(\mathbf{r},\theta,t)(c_R(\mathbf{r},\theta',t) \\ &\quad + c_C(\mathbf{r},\theta',t)) + D\partial^2_{\theta\theta}c_R(\mathbf{r},\theta,t), \\ \partial_t c_C(\mathbf{r},\theta,t) &= -v_0\nabla.\left(\frac{c_C(\mathbf{r},\theta,t)(\mathbf{P}_R+\mathbf{P}_C)}{\rho}\right) - \frac{J_C v_0}{\rho}\partial_\theta\int d\theta' \sin(\theta'-\theta)c_C(\mathbf{r},\theta,t)(c_R(\mathbf{r},\theta',t) \\ &\quad + c_C(\mathbf{r},\theta',t)) + D\partial^2_{\theta\theta}c_C(\mathbf{r},\theta,t). \end{aligned} \tag{28}$$

These Smoluchowski equations lead to similar polynomial contributions for the moments equations (17), where the parameters are modified according to: $j_{RR}, j_{RC} \to J_R v_0 \rho^{-1}$ and $j_{CC}, j_{CR} \to J_C v_0 \rho^{-1}$. In this case, the first polar moment equation has an identical form for both CTRL and RAB5A cells with identical parameters $j_R = j_{RR} = j_{RC}$ and $j_C = j_{CC} = j_{CR}$. We assume that $\mathbf{P}_R$ and $\mathbf{P}_C$ are still colinear and Eq. (20) becomes:

$$\begin{cases} v_R = v_C = v_0(\phi p_R + (1-\phi)p_C) \\ 0 = (-D_R + j_R\rho_R)p_R + j_R\rho_C p_C - \frac{j_R^2}{2D_R}\rho_R^2 p_R^3 - \frac{j_R^2}{D_R}\rho_R\rho_C p_R^2 p_C - \frac{j_R^2}{2D_R}\rho_C^2 p_C^2 p_R \\ 0 = (-D_C + j_C\rho_C)p_C + j_C\rho_R p_R - \frac{j_C^2}{2D_R}\rho_C^2 p_C^3 - \frac{j_C^2}{D_C}\rho_C\rho_R p_C^2 p_R - \frac{j_C^2}{2D_C}\rho_R^2 p_R^2 p_C \end{cases} \tag{29}$$

The critical volume fraction corresponding to equation (22) can then be written:

$$\phi^* = \frac{\mathrm{j}_C + \mathrm{j}_C\mathrm{j}_R + \mathrm{j}_R - \sqrt{(\mathrm{j}_C + \mathrm{j}_C\mathrm{j}_R + \mathrm{j}_R)^2 - 4(\mathrm{j}_C\mathrm{j}_R + \mathrm{j}_R\mathrm{j}_C)}}{4\mathrm{j}_C\mathrm{j}_R} \tag{30}$$

where we defined: $\mathrm{j} = j\rho/D$. In this context, the experimental result $\phi^* = 1/2$ implies $j_C\rho/D_C = 2 - j_R\rho/D_R$ (where $j_C\rho/D_C < 1$ since CTRL cells do not present any flocking transition alone). Finally, this shows that the implicit alignment rule yields hydrodynamic equations that are formally equivalent to the case of mutual alignment upon redefinition of coupling parameters, provided that the self alignment parameter of CTRL cells j_C is non vanishing. This shows the robustness of our approach and its broad applicability.

1.21.2 Implicit alignment rule and majority rule

Last, we show that for $j_C = 0$ (CTRL cells with no self-alignment) the majority rule as introduced in the agent based model, which assumes that self alignment depends on the number of neighboring RAB5A cells, can be taken into account and yields upon coarse graining the same class of hydrodynamic equations as Eq. (20). Taking into account a dependence of j_C on the number of neighboring RAB5A cells, Eq. (27) becomes:

$$\begin{cases} \dot{\mathbf{r}}_{R,i} = v_0 z_{R,i}^{-1}\left(\sum_{j\in R}\mathbf{n}_{R,j} + \sum_{j\in C}\mathbf{n}_{C,j}\right) \\ \dot{\theta}_{R,i} = J_R v_0 z_{R,i}^{-1}\,\mathbf{n}_{R,i} \wedge \left(\sum_{j\in R}\mathbf{n}_{R,j} + \sum_{j\in C}\mathbf{n}_{C,j}\right) + \eta_{R,i} \\ \dot{\mathbf{r}}_{C,i} = v_0 z_{C,i}^{-1}\left(\sum_{j\in R}\mathbf{n}_{R,j} + \sum_{j\in C}\mathbf{n}_{C,j}\right) \\ \dot{\theta}_{C,i} = J_C v_0 z_{C,i}^{-1} F(z_{C,i}^R)\,\mathbf{n}_{C,i} \wedge \left(\sum_{j\in R}\mathbf{n}_{R,j} + \sum_{j\in C}\mathbf{n}_{C,j}\right) + \eta_{C,i} \end{cases} \tag{31}$$

where $F(z^R_{C,i})$ is a threshold function that depends on the number of RAB5A neighbors of the CTRL cell i. It may for instance be written in the form: $F(z^R_{C,i}) = \min(1, \max(z^R_{C,i} - z_{threshold}, 0))$, which is null if the number of neighbors falls below a threshold value and 1 above. In the simple case where $z_{threshold} = 1$, the Smoluchowski equation writes:

$$\begin{aligned}
\partial_t c_R(\mathbf{r},\theta,t) &= -v_0\nabla.\left(\frac{c_R(\mathbf{r},\theta,t)(\mathbf{P}_R+\mathbf{P}_C)}{\rho}\right) - \frac{J_R v_0}{\rho}\partial_\theta \int d\theta' \sin(\theta'-\theta) c_R(\mathbf{r},\theta,t)(c_R(\mathbf{r},\theta',t) \\
&\quad + c_C(\mathbf{r},\theta',t)) + D\partial^2_{\theta\theta} c_R(\mathbf{r},\theta,t) \\
\partial_t c_C(\mathbf{r},\theta,t) &= -v_0\nabla.\left(\frac{c_C(\mathbf{r},\theta,t)(\mathbf{P}_R+\mathbf{P}_C)}{\rho}\right) - \frac{J_C v_0}{\rho}\partial_\theta \int d\theta' \sin(\theta'-\theta) c_C(\mathbf{r},\theta,t) c_R(\mathbf{r},\theta',t) \\
&\quad + D\partial^2_{\theta\theta} c_C(\mathbf{r},\theta,t) - \frac{J_C v_0 \rho_R V}{\rho}\partial_\theta \int d\theta' \sin(\theta'-\theta) c_C(\mathbf{r},\theta,t) c_C(\mathbf{r},\theta',t) + D\partial^2_{\theta\theta} c_C(\mathbf{r},\theta,t)
\end{aligned} \tag{32}$$

This leads to the modified equation (20), where $j_{RC}, j_{RR} \to j_R = J_R v_0 \rho^{-1}, j_{CR} \to j_{CR} = J_C v_0 \rho^{-1}, j_{CC} \to j_{CC}\rho_R = (J_C v_0 V \rho^{-1})\rho_R$:

$$\begin{cases}
v_R = v_C = v_0\rho^{-1}(\rho_R p_R + \rho_C p_C) \\
0 = (-D_R + j_R\rho_R)p_R + j_R\rho_C p_C - \frac{j_R^2}{2D_R}\rho_R^2 p_R^3 - \frac{j_R^2}{D_R}\rho_R\rho_C p_R^2 p_C - \frac{j_R^2}{2D_R}\rho_C^2 p_C^2 p_R \\
0 = (-D_C + j_{CC}\rho_C\rho_R)p_C + j_{CR}\rho_R p_R - \frac{j_{CC}^2}{2D_R}\rho_C^2 p_C^3 - \frac{j_{CR}j_{CC}}{D_C}\rho_C\rho_R p_C^2 p_R - \frac{j_{CR}^2}{2D_C}\rho_R^2 p_R^2 p_C
\end{cases} \tag{33}$$

In the general case of a different value for $z_{threshold}$, the equation for p_C writes: $0 = (-D_C + j_{CC}\rho_C\rho_R^{z_{threshold}})p_C + j_{CR}\rho_R p_R - \frac{j_{CC}^2}{2D_R}\rho_C^2 p_C^3 - \frac{j_{CR}j_{CC}}{D_C}\rho_C\rho_R p_C^2 p_R - \frac{j_{CR}^2}{2D_C}\rho_R^2 p_R^2 p_C$. The incidence of j_{CC} on the critical volume fraction ϕ^* increases with the density and decays with the value of the threshold, as $\phi < 1$.

In conclusion, our coarse-graining procedure applies to various microscopic dynamics describing mixtures of interacting cells, and yields robust hydrodynamic equations (Eq. (20)) for uniform phases. This allows for a simple description of the flocking transition as a supercritical pitchfork bifurcation, independently of the specifics of the alignment mechanism.

1.22 Introduction of friction

Cell-cell friction forces may be introduced phenomenologically in the force balance equation, as is standard for multi component fluids where each phase can have non vanishing relative

velocities ; the derivation of the friction coefficient from the explicit coarse graining of the microscopic dynamics is left for further work. Of note, in the uniform case, contributions of friction forces do not appear in the polarity equations, because they would only appear in gradient terms. Taking into account friction forces in the force balance equation thus does not modify our results for the polarity of uniform phases. Note that cell/cell friction forces are relevant in the case of explicit alignment rules only; our analysis of the implicit alignment rule assumes an elastic behavior at short times, and thus a vanishing relative velocity of the two cell types, so that $v_R = v_C$. In the case of explicit alignment, Equation (20) then becomes:

$$\begin{cases} v_R = v_{0R} p_R + \xi \rho_C (v_C - v_R), \quad v_C = v_{0C} p_C + \xi \rho_R (v_R - v_C) \\ 0 = (-D_R + j_{RR}\rho_R) p_R + j_{RC}\rho_C p_C - \frac{j_{RR}^2}{2D_R}\rho_R^2 p_R^2 p_R - \frac{j_{RC} j_{RR}}{D_R}\rho_R \rho_C p_R^2 p_C - \frac{j_{RC}^2}{2D_R}\rho_C^2 p_C^2 p_R \\ 0 = -D_C p_C + j_{CR}\rho_R p_R - \frac{j_{CR}^2}{2D_C}\rho_R^2 p_R^2 p_C \end{cases} \tag{34}$$

where ξ is the friction parameter. Friction leads to the new expressions for the velocities, that recovers the elastic limit of section 1.21 for high values of ξ:

$$\begin{cases} v_R = \frac{v_{0R} p_R + \xi(\rho_R v_{0R} p_R + \rho_C v_{0C} p_C)}{1 + \xi(\rho_R + \rho_C)} \\ v_C = \frac{v_{0C} p_R + \xi(\rho_R v_{0R} p_R + \rho_C v_{0C} p_C)}{1 + \xi(\rho_R + \rho_C)}. \end{cases} \tag{35}$$

Our observation in experiments that $v_R = v_C$ can thus be recovered by assuming a large value of ξ (or equivalently an elastic behavior), as we do in the main text.

Supplementary Model References

36. Giavazzi, F. *et al.* Flocking Transitions in Confluent Tissues. *Soft Matter* **14,** 3471–3477. ISSN: 1744-6848 (Electronic) 1744-683X (Linking) (May 2018).

37. Yllanes, D., Leoni, M. & Marchetti, M. C. How Many Dissenters Does It Take to Disorder a Flock? *New Journal of Physics* **19,** 103026. ISSN: 1367-2630. (2023) (Oct. 2017).

62. Vicsek, T., Czirók, A., Ben-Jacob, E., Cohen, I. & Shochet, O. Novel type of phase transition in a system of self-driven particles. *Physical review letters* **75,** 1226 (1995).

63. Ginelli, F., Peruani, F., Bär, M. & Chaté, H. Large-scale collective properties of self-propelled rods. *Physical review letters* **104,** 184502 (2010).

64. Baconnier, P. *et al*. Self-Aligning Polar Active Matter. *arXiv preprint arXiv:2403.10151* (2024).

65. Zhao, Y., Ihle, T., Han, Z., Huepe, C. & Romanczuk, P. Phases and homogeneous ordered states in alignment-based self-propelled particle models. *Physical Review E* **104,** 044605 (2021).

66. Shimoyama, N., Sugawara, K., Mizuguchi, T., Hayakawa, Y. & Sano, M. Collective motion in a system of motile elements. *Physical Review Letters* **76,** 3870 (1996).

67. Rein, M. & Speck, T. Applicability of effective pair potentials for active Brownian particles. *The European Physical Journal E* **39,** 1–9 (2016).

68. Arnoulx de Pirey, T., Lozano, G. & Van Wijland, F. Active hard spheres in infinitely many dimensions. *Physical review letters* **123,** 260602 (2019).

69. Bickmann, J. & Wittkowski, R. Predictive local field theory for interacting active Brownian spheres in two spatial dimensions. *Journal of Physics: Condensed Matter* **32,** 214001 (2020).

70. Arnoulx de Pirey, T., Manacorda, A., van Wijland, F. & Zamponi, F. Active matter in infinite dimensions: Fokker–Planck equation and dynamical mean-field theory at low density. *The Journal of Chemical Physics* **155** (2021).

71. Te Vrugt, M., Bickmann, J. & Wittkowski, R. How to derive a predictive field theory for active Brownian particles: a step-by-step tutorial. *Journal of Physics: Condensed Matter* **35,** 313001 (2023).

72. Li, Y. I., Garcia-Millan, R., Cates, M. E. & Fodor, É. Towards a liquid-state theory for active matter (a). *Europhysics Letters* **142,** 57004 (2023).

Supplementary Files

This is a list of supplementary files associated with this preprint. Click to download.

- SupplementaryMovie1.mp4
- SupplementaryMovie2.mp4
- SupplementaryMovie3.mp4
- SupplementaryMovie4.mp4
- SupplementaryMovie5.mp4
- SupplementaryMovie6.mp4